

GLOBAL DISTRIBUTION OF MICROBURSTS IN THE EARTH'S  
MAGNETOSPHERE

BY

Alexander Bennett Crew

A.B Dartmouth College, 2008

M.A. Boston University, 2011

DISSERTATION

Submitted to the University of New Hampshire

in Partial Fulfillment of

the Requirements for the Degree of

Doctor of Philosophy

in

Physics

December, 2013

This dissertation has been examined and approved.

---

Dissertation Director, Harlan Spence  
Director, Institute for the Study of Earth, Oceans, and Space  
Professor of Physics

---

Lynn Kistler  
Professor of Earth, Oceans, and Space and Physics

---

Marc Lessard  
Associate Professor of Earth, Oceans, and Space and Physics

---

Dawn Meredith  
Associate Professor of Physics

---

Robyn Millan  
Associate Professor of Physics  
Dartmouth College

---

Date

## **DEDICATION**

*To my parents*

## **ACKNOWLEDGEMENTS**

There are a great many people that I should thank for their efforts to help me achieve this milestone, but I will start with my advisor, Harlan Spence. I consider myself fortunate to have had such a supportive advisor throughout my time in graduate school. From the moment I walked through the door at BU, Harlan was setting up opportunities for me to be involved in a multitude of interesting and enriching hardware projects. I sincerely appreciate all the time, advice, and encouragement that you have given me, as well as the opportunity to follow you to UNH and continue these efforts.

I have been fortunate to spend 4 summers (as well as a few other choice intervals) working at The Aerospace Corporation. In addition to conducting some of the research described in this thesis I had the opportunity to gain invaluable hardware experience working on a plethora of flight projects there. Everyone that I worked with there was helpful in providing the experience I've benefited from in navigating my graduate career. In particular I'd like to thank Bern Blake and Joe Fennell for sharing with me so much accumulated wisdom of the how and why detectors and instruments work the way they do. In addition to being my manager when I started at Aerospace, Jim Clemons continually pushed me to get more and more out of the Freja data set. I'm appreciative of many insightful conversations with Paul O'Brien on the subject of microbursts. Finally, I'd like to thank Mark Looper for providing me with SAMPEX data files, in particular the post-2004 events.

The FIREBIRD project is in many ways a culmination of all the work that I've been doing, and I certainly could not have done it alone. I'd like to thank Brian Larsen for guiding me through the details of instrument design and innumerable assists along the way. Ehson Mosleh and the whole team at MSU made my job substantially easier when it came to interfacing between the two halves of the mission. I'd like to thank Mark Widholm and Steve Longworth for their patience in explaining electronics to me, and their assistance in troubleshooting the issues that did come up. Everyone downstairs in the electronics shop has been gracious in both fitting in work for me as well as explaining how and what was being done. Finally, Jason Legere helped with both keeping track of everything as well as the nuts and bolts (literally) of assembly.

Here at UNH (and before that at BU), I've been glad to work in such a supportive research group. I'd like to thank Sonya Smith for being a wonderful project manager—taking care of innumerable logistical details that I dislike dealing with as well as gently prodding me to the finish line. Andrew Jordan, Chia-Lin Huang, and Alex Boyd have put up with me (no small feat) for the last few years and provided all sorts of help and encouragement from the large to the mundane.

Finally, I would like to thank my family. Words do not suffice to describe your help and support along the way. My parents have encouraged my intellectual curiosity at every step of the way, and my sister Hilary has been a pillar of support in the whole process. This thesis would not have been possible without everything you did and do for me.

# TABLE OF CONTENTS

SIGNATURE PAGE .....	II
DEDICATION .....	III
ACKNOWLEDGEMENTS.....	IV
TABLE OF CONTENTS.....	VI
LIST OF FIGURES.....	IX
LIST OF TABLES .....	XVII
ABSTRACT.....	XVIII
LIST OF ABBREVIATIONS .....	XX
CHAPTER 1 .....	1
INTRODUCTION AND MOTIVATION .....	1
RADIATION BELT OVERVIEW .....	1
SOURCES AND LOSSES.....	6
MICROBURSTS .....	11
VLF WAVE ACTIVITY .....	15
THESIS OBJECTIVE.....	19
CHAPTER 2.....	21
MICROBURST EVENT DISTRIBUTIONS AND INTENSITIES .....	21
MOTIVATION.....	21
SAMPEX DATA .....	21
CHARACTERISTICS OF INDIVIDUAL BURSTS.....	23

<i>Event Location</i> .....	26
<i>Event Intensity</i> .....	32
<i>Event Duration</i> .....	40
DISCUSSION.....	41
<i>Correlations with Chorus</i> .....	42
<i>Intensity Distributions</i> .....	44
<i>Storm Phase Analysis</i> .....	45
CONCLUSIONS .....	47
<b>CHAPTER 3.....</b>	<b>49</b>
<b>MAPPING THE SOURCE REGIONS .....</b>	<b>49</b>
MOTIVATION.....	49
THEORY OF MICROBURST GENERATION .....	49
FREJA DATA.....	55
MAPPING MICROBURST SOURCE REGION.....	59
DISCUSSION.....	67
CONCLUSIONS .....	72
<b>CHAPTER 4.....</b>	<b>74</b>
<b>HARDWARE DEVELOPMENT.....</b>	<b>74</b>
MOTIVATION.....	74
FIREBIRD OVERVIEW.....	74
FIREBIRD SCIENCE OBJECTIVES.....	77
<i>Spatial Decorrelation Scale Length of Microbursts.....</i>	<i>77</i>
<i>Energy Range and Features of Individual Events .....</i>	<i>82</i>
<i>Global Loss due to Microbursts .....</i>	<i>84</i>
FIRE INSTRUMENT DESIGN AND CONCEPT OF OPERATIONS .....	85

<i>FIREBIRD Science Operations Plan .....</i>	85
<i>Analog Electronics and Detectors .....</i>	90
<i>Digital Board and Instrument Timing .....</i>	96
<i>Power Board and Unit Assembly.....</i>	99
INSTRUMENT CALIBRATION .....	101
<i>Radionuclide Source Testing at UNH.....</i>	102
<i>Beta Spectrometer Testing at The Aerospace Corporation.....</i>	109
<i>Geant4 Model validation.....</i>	115
CONCLUSIONS .....	118
<b>CHAPTER 5.....</b>	<b>120</b>
<b>ASSESSING GLOBAL LOSS .....</b>	<b>120</b>
MOTIVATION.....	120
COORDINATING MULTIPOINT AND SINGLE POINT MEASUREMENTS .....	121
ESTIMATES FROM SAMPEX .....	122
EXPANDING TO MULTIPOINT .....	132
CONCLUSIONS .....	133
<b>CHAPTER 6.....</b>	<b>136</b>
<b>CONCLUSIONS AND FUTURE WORK .....</b>	<b>136</b>
SUMMARY .....	136
FOCUS QUESTIONS .....	137
VAN ALLEN PROBES AND BARREL.....	143
PARTING WORDS .....	145
<b>WORKS CITED.....</b>	<b>146</b>

## LIST OF FIGURES

Figure 1. Overview of radiation belt processes from (Mauk et al., 2012). This list is not presumed to be exhaustive but rather indicates the zoo of active processes, and situates microburst science within the greater whole. ....	5
Figure 2. Balloon observations of microbursts from x-ray counts (Anderson et al., 1966). Over a short time period a large number of microbursts are seen with significant variability among them.....	12
Figure 3. Chorus emissions measured with power spectrograms of electric field fluctuations measured by the WBD instruments on the 4 Cluster spacecraft on 18 April 2002. 2 Discrete chorus elements are seen rising in tone to 1/2 $f_{ce}$ (Santolik et al., 2003).....	16
Figure 4. Intensity distributions of lower-band chorus waves as a function of MLT, L for both equatorial and off-equatorial chorus (Bortnik and Thorne, 2007). 18	
Figure 5. An example of microburst events from SAMPEX. In this case, a long series of microburst events of various different sizes are shown. T= 0 corresponds to one particular microburst. ....	24
Figure 6. Event frequency as a function of MLT, L measured by SAMPEX. L ranges from 0 to 10, noon is at the top of the figure and midnight is at the bottom. This represents the average event frequency over the period 1996-	

2010. Event frequencies are measured as number of events observed per minute of observation within each bin. ....	28
Figure 7. Event Frequency as a function of AE, measured in events per minute of observation time with the corresponding AE levels. Overall event levels are dramatically lower during times of low AE, and are pushed towards noon and midnight.....	29
Figure 8. Event frequency across storm phase, measured in events per minute of observation time. Quiet times encompasses all times with Dst > -20 (even if it is the beginning or end of a main or recovery phase). Microburst precipitation is strongest during the main phase of storms, as well as shifted closer to midnight during these times. ....	31
Figure 9. Event characterization for a single SAMPEX microburst event. First, the event has the background flux profile subtracted off to isolate the microburst. The black trace is that data, while the red is the Gaussian profile fit to the microburst event, from which the relevant characteristics (absolute intensity, duration) are extracted. ....	33
Figure 10. Relative Intensity Histogram from SAMPEX for all observed events follows a power law spectrum over the entire observed range. ....	34
Figure 11. Relative Intensity by AE bin. Blue is AE < 100nT, green is 100nT<AE<300nT and white is AE > 300nT. At lower AE relative intensity falls off more quickly. ....	35
Figure 12. Relative mapping as function of MLT, L by AE bin. During the quietest times there are not enough events to draw meaningful conclusions from, but	

otherwise the peak in relative intensity still occurs closest to dawn and does not shift with increasing AE.	37
Figure 13. Relative Intensity by Storm Phase. No matter what storm phase the peak relative intensity occurs closest to dawn, with seemingly similar values.	38
Figure 14. Absolute intensity histogram. Similar to the relative intensity histogram in showing a power-law like intensity distribution, albeit over a smaller range in values.	40
Figure 15. Event Duration Histogram. Average microburst length is ~70 ms, with most falling between 50 and 150 ms.	41
Figure 16. Prediction of resonance zone for electrons for a variety of conditions. Top panel holds wave normal angles constant and looks for a first-order resonance at a variety of magnetic latitudes with MeV energy particles seen on SAMPEX. Bottom panel looks for resonance at the equator using higher order resonances (Lorentzen et al., 2001)	52
Figure 17. Resonance zones in L, magnetic latitude for interactions with chorus at different equatorial pitch angles and energies. The red indicates the resonant regions at different L values (Ni and Summers, 2010)	54
Figure 18. Microbursts observed by Freja. Three microbursts are observed starting at the maximum energy of 25keV and terminating around 5keV. The curved shape of the bursts is indicative of the time of flight effects whereby the most energetic particles reach the detector first.	57

Figure 19. Distance determination of a microburst event using the dispersion within a single event and a time of flight analysis to determine the source region. For each channel the delay between the arrival of particles of that energy and that of the highest energy particles is plotted against the reciprocal of its velocity in order to determine the distance traveled. ....	57
Figure 20. Distribution of microburst events measured by Freja normalized by observation time within each MLT, L bin, extending out to a maximum L value of 10. This comprises all events which matched the necessary conditions to be identified as a microburst and mapped.....	60
Figure 21. Average distance off the equator for Freja events measured in degrees latitude, binned by MLT and L. Only bins with at least 5 events are shown.....	62
Figure 22. Histograms of microburst source latitude and characteristic energy. Top panel shows source latitude (positive is Northern hemisphere, which is the same hemisphere as the spacecraft) for all events, only downside and only midnight events. Bottom panel shows the calculated characteristic energy for the spectra of events in the different categories.....	63
Figure 23. Fraction of events that correspond to mapped location within 15 degrees of the equator binned by L and MLT. Events that mapped to within 15 degrees of the equator are those which can be considered to have a possibly equatorial source.....	65
Figure 24. Energy spectrum of a single microburst event. The energy spectra was fitted to an exponential distribution with a characteristic energy $E_0$ .....	66

Figure 25. Average characteristic energy for events in different regions by MLT, L. Only those regions with at least 5 events are shown.....	67
Figure 26. FIRE/BIRD interface testing at MSU. MSU's BIRD bus is seen in the bottom left, while FIRE is held on the right by the clamp. A single interface cable connects FIRE to BIRD. BIRD occupies the bottom 10x10x10cm of the CubeSat structure, while FIRE uses the remaining 5x10x10cm space. The detectors are within the (covered) doghouses which protrude from the top (analog) electronics board. A model of the spacecraft exterior (with extended antenna) is visible in the top left. ....	76
Figure 27. Process for calculating the spatial decorrelation of chorus and microbursts. Chorus calculations are done using data from Cluster spacecraft, while microburst observations are from SAMPEX. Figure from FIREBIRD proposal (Spence, Private Communication). .....	80
Figure 28. Comparison of FIRE timing with microburst duration observations from SAMPEX. The green identification timescale is that of the MBP calculation (100 ms), while the normal hi-res data rate, and the practical limit are 18.75 and 12.5 ms respectively.....	88
Figure 29. MicroBurst Parameter Identification. The top line is the 20 ms count rate from SAMPEX for a period with a number of microburst events, while at the bottom is the calculated MBP for the time interval. Spikes in the MBP correspond with microburst events seen by SAMPEX. ....	89
Figure 30. A single FIRE detector inside a collimated doghouse. The doghouses were coated to prevent oxidation, hence the different color. The short	

collimator is visible as part of the top piece. The light-tight foil (not shown) goes between the delrin ring and the top half of the doghouse.....	95
Figure 31. FIRE Flight analog board. Tape covers the opening to the collimated detector, while a removable dust cover (green) is attached to the surface detector to protect the foil. The sensitive electronics on the analog board (DAPPER) are underneath the copper shield.....	96
Figure 32. Top side view of FIRE digital board. The blank space in the top right corner is for the collimated doghouse which is pressed between the analog and digital boards. The connection to the analog board (above) and digital board (below) is through the black connector at bottom right.....	99
Figure 33. Fully built FIRE unit. FIRE->BIRD interface cable extends from bottom left. Mechanical dust covers are placed over each detector aperture currently. Mid-plane standoffs for attaching FIRE to the spacecraft structure are visible above (on left) analog board, and below (on both sides) the power board.....	100
Figure 34. Testing setup at UNH. The gamma source was held approximately 3" above the detector. The GSE board is visible to the left of the instrument, along with the laptop to command FIRE.....	103
Figure 35. UNH source testing of FIRE A. Collimated detector is shown in solid lines, surface detector in dashed lines. Different colors represent different sources.....	105
Figure 36. Testing DAPPER linearity with a lab pulser. Data was taken using an oscilloscope to measure input voltage from laboratory precision pulser as	

well as the DAPPER shaper pulse width (in ns). This pulse width was then converted to the nominal channel using the 14.7456 MHz digital board clock.	107
Figure 37. Pulser test on FIRE B. The small step feature seen near channel 100 is the result of artifact of the GSE software, which did not appear in the flight software.....	109
Figure 38. Histogram results from Flight Unit 1 Collimated Detector. The top panel is traces in the highest energy resolution mode of the beam at different set energies. The bottom panel is a plot of the center channel of each peak showing the linear energy response and calibration coefficients.....	112
Figure 39. Normal Incidence on surface detector. Here the instrument is in flight configuration with very wide energy bins. As expected the energy peaks fall in the correct bins within the nominal (200-1000 keV) energy range. At higher energies, the peak moves to the lower energies predicted due to the electrons punching through the detector. Background counts are a small fraction of the total.....	115
Figure 40. Geant4 Model of instrument response in each of the 6 nominal flight channels for the uncollimated (surface) detector. Figure courtesy of Brian Larsen .....	117
Figure 41. Comparison of microburst characteristics across storm phase. From left to right are main phase, recovery phase, and all events (total). From top to bottom, the plots are ordered as event frequency, event absolute intensity (total loss), event relative frequency.....	123

Figure 42. Producing a storm event frequency map. Top left is the baseline main phase event frequency map (events/min). Top right is a map of where SAMPEX's observations come from. Bottom left is applying that map of observations to the baseline. Bottom right is then the actual event frequencies as measured by SAMPEX for that storm. The storm in question is the October 1998 storm that was part of the GEM challenge. All plots are in MLT, L..... 126

Figure 43. Total loss across events. Typical losses during the main phase of storms fell between  $10^{22}$  and  $10^{24}$  electrons. Additionally, there was a lower-loss tail, of a handful events below  $10^{22}$  total electrons for which microbursts were likely not very significant. During the recovery phase the total losses were generally higher, but this was due to the longer duration of recovery phases relative to the main phase—the loss rate was higher during the main phase..... 128

## **LIST OF TABLES**

Table 1. Sources used in radionuclide testing at UNH with relevant characteristics .....	104
Table 2. Calibration coefficients for FIREBIRD Flight units. ....	113

# **ABSTRACT**

## GLOBAL DISTRIBUTION OF MICROBURSTS IN THE EARTH'S MAGNETOSPHERE

by

Alexander Bennett Crew

University of New Hampshire, December, 2013

The dynamics of the Earth's radiation belts are governed by the interplay between the various source and loss terms. Electron microbursts represent a particular form of electron loss through precipitation to the atmosphere. Moreover, assessing the total significance of microburst loss to radiation belt dynamics is an important and still unresolved question. This thesis seeks to qualify and quantify the scale and properties of microburst precipitation. Accordingly, the thesis has 4 main guiding goals: (1) to understand the similarities and differences in characteristics among the microburst event population; (2) to create constraints for models and theories of microburst generation; (3) to detail how past observations inform and direct the development of the next set of microburst observations; and (4) to assess the global scale of microburst loss. To accomplish these goals I draw on existing observations of microburst from the SAMPEX and Freja missions, as well as operational planning and design for the upcoming FIREBIRD CubeSat. In particular, the nearly 15

years and ~685,000 individual microburst events from SAMPEX provide a comprehensive description of the microburst population, showing that microbursts are generally seen on the downside from L of approximately 4 to 8, with event frequencies that typically follow power-law like distributions and typical event durations ~100 ms. Utilizing measurements of keV level microbursts from Freja I show how we can map the source locations of individual microbursts. Using a time-of-flight analysis I show that microbursts observed by Freja, typically originate from equatorial source locations along the downside in a similar set of locations to the MeV energy events observed by SAMPEX and correlate well with measurements of chorus waves. The upcoming FIREBIRD CubeSat mission utilizes these observations to drive instrument requirements as well as a science operations plan to address the goals of understanding the spatial scale size and energy dependence of individual microburst events. Finally, I build tools for quantifying the total loss due to microbursts and comparing that to the total content of the radiation belts.

## **LIST OF ABREVIATIONS**

- AE: Auroral Electrojet activity index
- BIRD: Bus In support of Radiation Detection
- CRRES: Combined Release and Radiation Effects Satellite
- FIREBIRD: Focused Investigations of Relativistic Electron Burst Intensity,  
Range, and Dynamics
- FIRE: FIREBIRD Instrument for Relativistic Electrons
- HILT: Heavy Ion Large Telescope
- LEO: Low Earth Orbit
- SAMPEX: Solar, Anomalous, Magnetospheric Particle Explorer
- TLE: Two Line Element
- VLF: Very Low Frequency
- ULF: Ultra Low Frequency

# CHAPTER 1

## INTRODUCTION AND MOTIVATION

### Radiation Belt Overview

A natural consequence of the configuration and strength of the Earth's geomagnetic field is the existence of the radiation belts—a location where energetic particles are stably trapped by the Earth's magnetic field. Also known as the Van Allen Belts, the radiation belts are home to some of the most energetic particles present within the Earth's magnetosphere, with protons ranging in energy from 10 MeV up to more than a GeV, and electrons from several hundred keV to several MeV in energy. At these energies, particles are capable of penetrating the typical shielding of spacecraft and exacting radiation damage to critical components, which can under extreme conditions lead to spacecraft failure (Lanzerotti, 2001). Radiation damage takes many different forms, and while the detailed mechanisms are interesting and may vary, the broader note is that the radiation belts are a particularly inhospitable environment. While these types of damage represent extreme circumstances, they motivate why the dynamics and variability of the radiation belts are of broad and significant importance.

Structurally, the Van Allen Belts are typically described as divided into two distinct belts, denoted by location as an inner belt and an outer belt. The inner belt, which typically extends in L from 1 to 2.5, is home to both energetic

electrons and protons, and is typically considered to be relatively stable ( $L$  being a measure of the radial distance mapped in a dipole magnetic field; it represents the radial distance of a magnetic field line at the equator expressed in Earth radii). By contrast, the outer belt, which typically extends from 3 to 8 in  $L$ , exhibits much more dynamic variability. As shown in *Baker et al. [2004]*, long-term measurements of MeV electrons from SAMPEX over the course of an entire solar cycle revealed outer belt fluxes varying dramatically by 4 orders of magnitude. Moreover, these changes occurred over a variety of time scales (often, but not necessarily in response to geomagnetic storms) and with accompanying variability in the precise  $L$  shell location of the outer belt ( $L$  shell refers to the surface on which a particle would drift around the Earth when its motion is governed by the third adiabatic invariant (Roederer, 1970)). I will note also, that recent results from the Van Allen Probes Mission (née Radiation Belt Storm Probes) have shown the existence of a transient 3<sup>rd</sup> belt or so-called storage ring (Baker et al., 2013) situated between the inner and outer belts. For the purposes of this thesis, the presence of a third belt is more an example of the dynamic nature of the radiation belts, particularly of the outer belt, than a key structural feature. However, understanding the dynamic variability of the radiation belts is a central need for contending with their radiation hazards and is thus a prime objective of this thesis.

Historically, the dynamics of the radiation belts were originally considered to be governed by various diffusive processes, typically described in phase space (Schultz and Lanzerotti, 1974). Ordering particles by the adiabatic

invariants ( $\mu$ ,  $\kappa$ ,  $L^*$ ) in phase space is more useful for modeling the behavior of the belts, since by their definition the adiabatic invariants are conserved as long as the magnetic field changes slowly. However, I generally will not work in these coordinates throughout the thesis. Instead I will generally work in terms of particle energy, pitch angle, and  $L$  as they are sufficient for the questions that I am interested in, and obtainable through direct measurement at the instrument as opposed to requiring a detailed magnetic field model. These processes were those that tended to diffusively redistribute phase space density, for instance through energy or pitch angle diffusion. Such a treatment explained the broad morphology of the radiation belts, i.e. the existence of two belts and thus the presence of a slot region. However, pure diffusive treatments suffered in explaining rapid increases or decreases in particle flux for which the intrinsic physical timescales are too slow. Observations from two missions (CRRES and SAMPEX) particularly underscored the fact that while diffusion may explain some portion of the belts structure and slow time variation (Blake et al., 1992) (Baker et al., 2004) (Li. et al., 2011), other processes must be at work to produce the observed rapid dynamism.

To explain these clearly non-diffusive changes a whole host of various processes have been proposed and developed in the past few decades. They generally consist of physical processes that can rapidly accelerate particles or equally rapidly cause them to be lost from the stably trapped regions, either into the atmosphere or out of the magnetosphere; *Friedel et al.* [2002] provides an excellent review of the range of possible mechanisms for both the sources and

sinks of radiation belt particles. Wave particle interactions (Thorne, 2010) (Summers, Ni and Meredith, 2007) (Ni and Summers, 2010) provide one potent method for rapidly modifying particle populations; such interactions have the capacity to both accelerate particles and also cause them to be lost. I should emphasize that there exists a substantial variety of mechanisms within the broad category of wave particle interactions. Understanding how these mechanisms shape the dynamic evolution of the belts is a question that extends well beyond the scope of any single thesis and motivates a tremendous depth of current and ongoing research including major strategic spaceflight missions both in the United States and internationally.

The scientific rationale for NASA's Radiation Belt Storm Probes mission is laid out in *Mauk et al.* [2012]. A large number of processes that affect radiation belt dynamics, each of which requires further investigation and understanding, motivate the mission objectives (Millan and Baker, 2012). A cartoon from *Mauk et al.* [2012] of the wealth of processes operating within and upon the radiation belts is visible in Figure 1. The take-away message from this figure for this thesis is less about any one single process, and more that there are a great many processes that act simultaneously and collectively within and around the belts to govern its state. The challenge, of course, is to separate out the impact of any single process. Microbursts, the subject of this thesis, fall under two categories identified in Figure 1, both wave-particle interactions and precipitation.

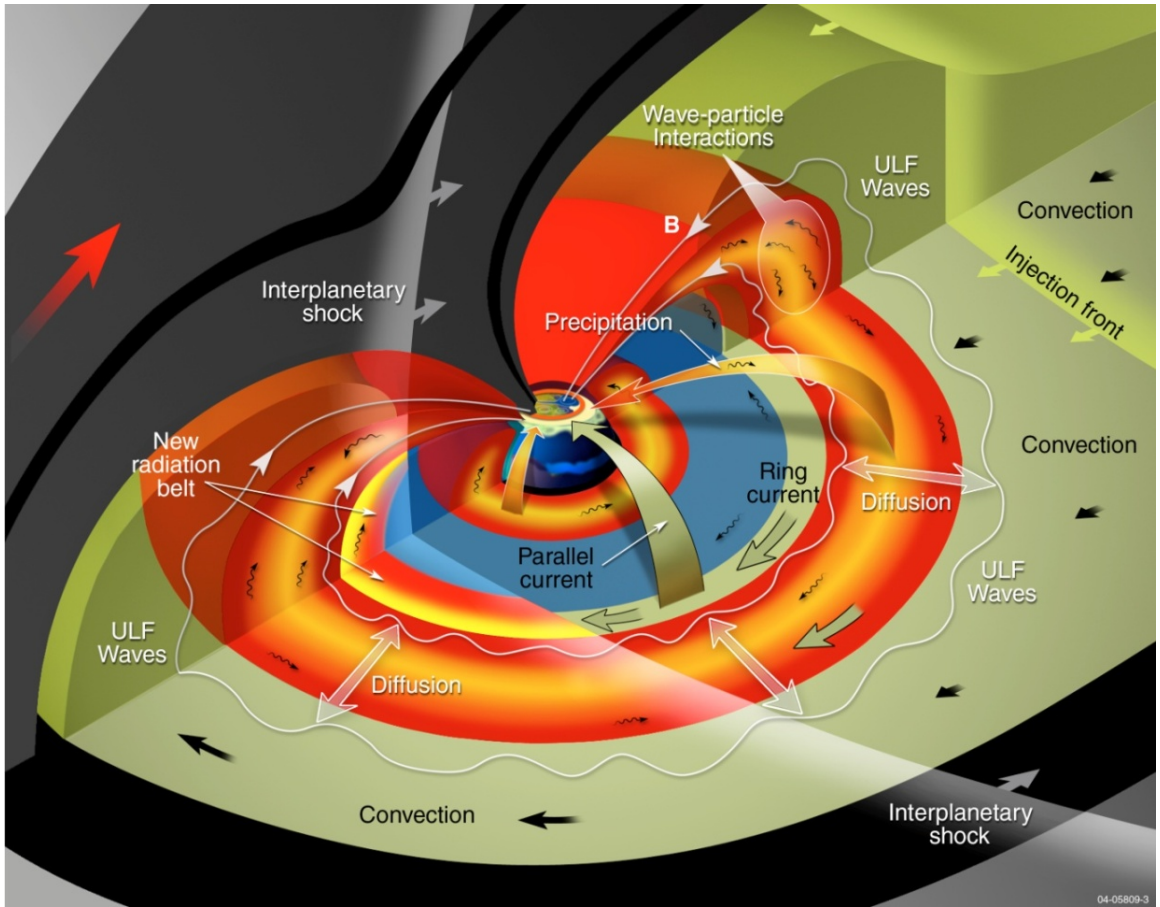


**Figure 1.** Overview of radiation belt processes from (Mauk et al., 2012). This list is not presumed to be exhaustive but rather indicates the zoo of active processes, and situates microburst science within the greater whole.

Underneath the broad umbrella of wave-particle interactions are a host of different wave modes (Thorne, 2010) that can have a variety of different impacts upon the particle population. While very low frequency (VLF) so-called chorus waves (typically with frequencies of a few kHz) are the ones most often associated with microburst precipitation (as will be discussed in greater detail in Chapter 3 in particular), there are many other electromagnetic wave modes present within the radiation belt environment. These different wave modes, and their interactions with the particles, are often proposed as an explanation for not

only the energization of lower energy or “seed” particles to higher energies (Horne, Glauert and Thorne, 2003), but also for the loss of the higher energy particles through pitch angle scattering (Hikishima et al., 2009). However, wave-particle interactions are not the only type of process that acts within the belts. As should become clear from Figure 1, the wealth and diversity of listed processes and the fact that they are acting potentially both globally and simultaneously mean that untangling which ones are responsible for which effects becomes a complicated task. At a fundamental level, this thesis is therefore about focusing narrowly upon a single process within the radiation belts and trying to understand both its phenomenological and physical properties as well as ultimately the scale of its impact on global radiation belt dynamics. Until we can isolate and quantify each source and loss mechanism identified in Figure 1, we will not be able to robustly predict radiation belt dynamics.

### **Sources and Losses**

As stated previously, one of the primary challenges in radiation belt science is to explain the changes in radiation belt fluxes in the aftermath of geomagnetic storms (although it should be noted that not all changes require storms). In 2003, Reeves *et al.* studied 276 different storms. Among similarly sized storms (as determined by Dst) they found that, at geostationary orbit, 53% exhibited a strong increase in the flux of relativistic (greater than several hundred keV) electrons afterwards, 19% exhibited a sharp decrease in fluxes, and 28% exhibited little change altogether (less than a factor of 2 in either direction). Reeves *et al.* [2003] concluded that the interplay between various competing

source and loss terms governed the overall dynamics of the outer zone's electrons. In storms where the source terms dominate, an overall enhancement resulted; when losses dominate, an overall weakening of the belts occurred, and when the source and loss terms are of comparable magnitude then little change in belt dynamics resulted overall.

The results of the *Reeves et al.* study become especially important when considering the deeper consequences. Though the total energy density of the relativistic electron population is minuscule compared to the lower-energy, pressure-bearing populations of ions that comprise the plasmashell and ring current, the energy per particle of the radiation belt electrons is enormous. For instance, estimates of the >1 MeV population of the radiation belts can be  $\sim 10^{25}$  electrons (Baker, Kanekal and Blake, 2004). Though comparatively small in total number to the other magnetospheric populations, their capacity to impart radiation damage even in low numbers amplifies their significance. Consequently, as *Reeves et al.*'s study illuminates, even small differences in the relative efficacy of the given source and loss processes can lead to dramatic differences in radiation belt content which in turn can lead to significantly different outcomes in terms of radiation belt dynamics and effects to technological systems. We know that different storms impacting different processes in different ways can therefore produce the wide range of observed changes. We still lack the detailed understanding of how, when, and where these different processes combine to produce a net effect for any given set of external drivers and internal responses.

The next step in sorting out the relevant governing physical processes is to assess the magnitude of the individual processes. Many, if not most, studies have focused on the ways by which radiation belt particles are accelerated and transported. These processes range from gradient drift and bounce resonance to direct cyclotron resonance over a range of waves that span ultra low frequency (ULF) magnetohydrodynamic waves to VLF waves. Particle acceleration is not the focus of this thesis, though we do appeal to these related wave-particle interactions in terms of their ability to scatter particles in pitch angle.

In this work, we focus instead on how radiation belt particles might be lost from the system, the other competing element in the tug-of-war battle with source mechanisms. Loss mechanisms come in various forms. One form is loss out of the magnetosphere when outer zone relativistic electron drift paths become untrapped and intersect the magnetopause (Turner et al., 2012), typically at storm times when either the internal field of the changing ring current becomes inflated or when the external compression of the magnetosphere from interplanetary shocks radically and abruptly change the magnetic configuration of the radiation belts on a time scale short compared to a particle's gradient drift time. This loss mechanism is a somewhat global process and is typically assessed by looking at electron dropouts in geostationary data.

The second major form of loss is loss through the other boundary of the radiation belt system, namely the upper atmosphere. If electrons are scattered into the atmospheric loss cone, they too can be removed from the system. The atmospheric loss cone is a cone defined in velocity space. A particle's pitch angle

is defined by the ratio of the components parallel and perpendicular to the local magnetic field by the below equation: (Roederer, 1970)

$$\alpha = \arccos \frac{v_{\parallel}}{v}$$

As the magnetic field strength changes slowly the first adiabatic invariant stays constant which changes the fraction of the total velocity that is in the parallel component (since the ratio of the perpendicular velocity to the magnetic field strength must be constant and the total energy does not change some parallel velocity becomes perpendicular). As the magnetic field strength increases (closer to the poles) the particle has more of its velocity turned into the perpendicular component until it reaches a point at which it has no parallel velocity, whereby it turns around and heads back towards the equator. This location is known as the mirror point. If a particle has sufficiently high parallel velocity (relative to its perpendicular component) then by the time it reaches its mirror point it will have reached the Earth's atmosphere and instead of bouncing back along the field line it instead is lost to the atmosphere through collisions. The critical pitch angle at which a particle mirrors too low to return defines the loss cone angle, as particles with that amount of parallel velocity or higher are lost to the atmosphere (the 'cone' designation comes from how that critical angle defines a cone in velocity space).

Particles in the radiation belt can experience pitch angle scattering that directs them into the atmospheric loss cone, whereby the mirror point for low pitch angle particles causes them to collide deep into the upper atmosphere and effectively be lost from the radiation belts. Pitch angle scattering typically occurs

through the presence of additional small perturbations to the local magnetic field, say from small amplitude waves. Through sequential interactions between the particles and the waves, they can random walk to new pitch angles in a diffusive process. If this interaction between the electrons and the waves brings an electron into the loss cone, then it will be lost to the atmosphere within a single bounce. This is a process known as “precipitation” and is one of the processes noted before and identified in Figure 1. Pitch angle scattering can occur slowly through a weak diffusion process that drains the radiation belts through what we might term drizzle rather than precipitation. Or it can occur impulsively, whereby a large number of particles are suddenly and dramatically scattered into the atmospheric loss cone and are lost. Such a process has been termed “microburst” precipitation and has been implicated as a major loss mechanism. It is the primary focus of this thesis.

A number of works, such as *Lorentzen et al.*, [2001] and *O'Brien et al.* [2004], have attempted to estimate the total loss of the radiation belts due to relativistic electron microbursts from single point measurements made by low Earth orbit (LEO) satellites (other works have sought to quantify the importance of microbursts in other manners (Comess et al., 2013)). However, owing to the necessary uncertainties and limitations involved in the estimates of microburst losses from LEO, the general conclusion was that the total loss due to microbursts could be enough to empty the outer radiation belt in a single day, but with the unsatisfying caveat of order of magnitude error bars. Unfortunately, this scale of uncertainty calls into question the significance of the geo-effectiveness

of this loss process. Losses on the timescale of a day or less are large enough to dominate dynamics, while those an order of magnitude lower (on the timescale of a week) would be unable to drive dynamics and thus would be at best a secondary process. In sum, while the microburst precipitation process has been identified as a possible major loss mechanism, single-point LEO measurements of the loss process limit our ability to quantitatively assess the impacts of the loss mechanism without additional assumptions (that are typically not well constrained by observations).

### **Microbursts**

As noted above, microburst precipitation is the focus of this thesis; hence we next discuss their history and qualities. Microbursts are short ( $\sim$ 100 ms) impulsive bursts of electron precipitation that represent a loss mechanism for high-energy magnetospheric electrons to the Earth's upper atmosphere. Measurements of microbursts date from the 1960's with balloon-borne measurements of bremsstrahlung x-rays produced when fast electrons strike the Earth's atmosphere (Anderson et al., 1966). At that early time, microbursts were identified by the short, temporal nature of the increases in x-ray counts and in a limited spatial domain, hence the term "microburst." An example of early microburst measurements from *Anderson et al.* [1966] is shown in Figure 2. Later balloon work (Rosenberg et al., 1977) reported significant variability in the characteristics of individual x-ray microburst events in terms of both size and time scale, as well as further solidifying the observations as being tied to auroral and sub-auroral latitudes.

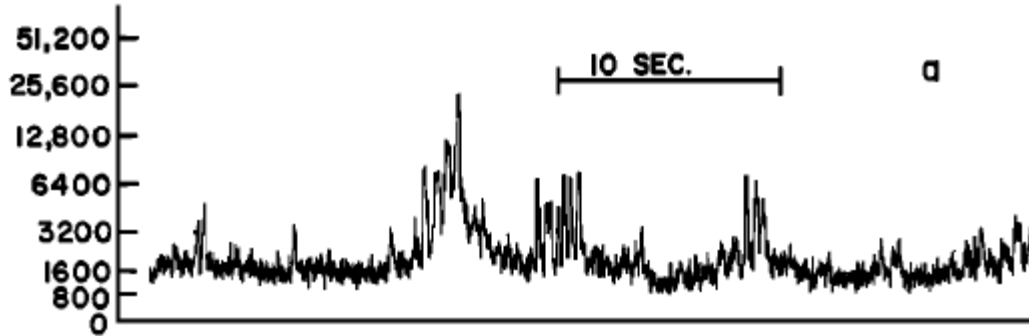


**Figure 2.** Balloon observations of microbursts from x-ray counts (Anderson et al., 1966). Over a short time period a large number of microbursts are seen with significant variability among them.

Since these earliest discovery measurements were of the secondary x-rays, not the primary electrons incident on the atmosphere, they provided only an indirect glimpse of the precipitating relativistic electrons. In order to directly measure the precipitating electrons, it is necessary to move the measurement platform above the earth's atmosphere and view the electrons as they are moving downwards to Earth in the atmospheric loss cone. This was accomplished with rocket and satellite-borne instruments.

During the 1990s, there were several rocket missions that directly measured the characteristics of electrons precipitating in a few individual microburst events. These observations of microbursts were typically associated with auroral measurements, and so were biased to lower energies (tens to hundreds of keV) than are typically considered as radiation belt particles. However, studies have shown that microbursts in these somewhat lower energy populations (up to a few hundred keV) are clearly related to the immediately higher energy populations (one half to many MeV) (Clemmons et al., 1994).

The ability of sounding rockets to directly measure precipitating electrons permitted for the first time direct measurements of the spectral shape of the electrons themselves present in microburst precipitation, rather than relying on inverting the x-ray spectrum (Reinard et al., 1997). From this, the energy spectra were matched to an exponential distribution across the range in energies measured, with given characteristic e-folding energies (typically 10-20keV). Additional work (Datta et al., 1996), measured the characteristic energy profiles of microburst precipitation from a sounding rocket in the energy range of 20-120 keV as well as a simple pitch angle structure, and then linked it to a pitch-angle diffusion model (Datta et al., 1997) to try and explain the events. The early measurements of pitch angle suggested that during microbursts, the pitch angle distribution becomes nearly isotropic (Datta et al., 1996), consistent with a wave-particle interaction with VLF waves; however no one-to-one correlation between individual particle events and distinct VLF wave activity was measured. Efforts were made to connect the microburst precipitation with cyclotron resonance of VLF wave activity (Skoug et al., 1996); however these were unable to fully explain the particle events. This connection had also been posited from bremsstrahlung measured after electron precipitation in conjunction with microbursts (Imhof et al., 1989). Nonetheless, these sounding rocket studies begin to connect microburst precipitation with VLF waves, a connection that will be further explored in greater detail later in the thesis.

The first direct measurements of fully relativistic ( $>1$  MeV) electron microbursts were made using the SEEP (Stimulated Emission of Energetic

Particles) instrument on board the S81-1 spacecraft (Imhof et al., 1992) in LEO. In their study, microburst precipitation was generally observed to occur closer to midnight than had been observed by studies investigating precipitation of lower energy particles. More recently and quite comprehensively, microbursts have been studied extensively using the SAMPEX satellite. SAMPEX, the Solar, Anomalous, Magnetospheric Particle Explorer, recorded measurements of microbursts from 1996 to 2012 also in LEO. In 2004, the mission reached the formal “end” of its science mission, but fortunately data from surviving instruments continued to be downlinked as long as the instrument survived. In the case of microburst measurements from SAMPEX, these primarily relied on the HILT instrument (Klecker et al., 1993), which continued working all the way until reentry in late 2012 (which provided some brief overlap with complementary high-altitude Van Allen Probes measurements).

A number of studies of microburst dynamics and effects have been performed using SAMPEX data. SAMPEX’s presence in low-earth orbit (520 x 670 km, 82° inclination) made it ideally suited to measure precipitating electrons in the atmospheric loss cone. Although the HILT instrument was intended for heavy ion measurements, the detectors were also sensitive to MeV electrons, and so those electrons dominated the counts in the outer radiation belts, leading to some of the first measurements of >1 MeV electron microbursts with SAMPEX (Nakamura et al., 1995). Further studies, such as *Lorentzen et al.* [2001], attempted to correlate the observations of microbursts from SAMPEX with VLF wave activity, in addition to later efforts to quantify the magnitude of microburst

precipitation such as in (O'Brien, Looper and Blake, 2004) and (Lorentzen, Looper and Blake, 2001). SAMPEX measurements are central to this thesis and will be described in much more detail within the body of the thesis.

### **VLF Wave Activity**

VLF wave activity has long been associated with measurements of microbursts. More specifically, the principal VLF wave type of interest for microburst science is called chorus. Chorus waves are plasma waves which propagate through the magnetosphere in the whistler mode with typical frequencies of hundreds of hertz to a few kHz. Chorus is observed in discrete elements which last for a few tenths of a second, and within each element the wave frequency changes (typically, but not always increasing in tone) (Santolik et al., 2003). Figure 3 shows an example of chorus emissions measured using the four Cluster spacecraft.

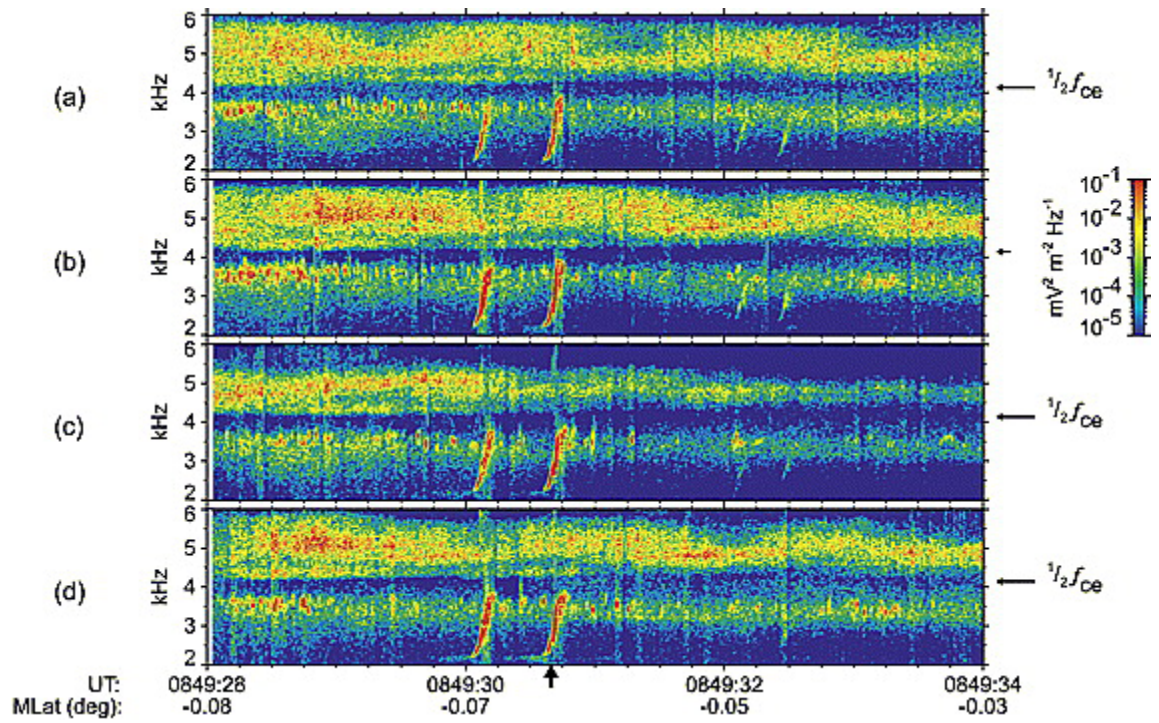


**Figure 3. Chorus emissions measured with power spectrograms of electric field fluctuations measured by the WBD instruments on the 4 Cluster spacecraft on 18 April 2002. 2 Discrete chorus elements are seen rising in tone to  $1/2 f_{ce}$  (Santolik et al., 2003).**

The structure of chorus emissions is intimately tied to the equatorial electron gyrofrequency ( $f_{ce}$ ). Early measurements of chorus frequencies typically varied from one quarter to three quarters of the electron gyrofrequency (Tsurutani and Smith, 1974) but recording a minimum in power near  $0.5 f_{ce}$ . This breakpoint in the spectrum serves to divide chorus emissions into two bands: lower band chorus (below  $0.5 f_{ce}$ ) and upper band chorus ( $0.5\text{--}0.9 f_{ce}$ ). This distinction is not solely in nomenclature; although there are many similarities between upper and lower band chorus, there are differences in precisely where in the magnetosphere they exhibit strength as well as where they will be in resonant conditions with energetic electrons. Similar maps of microburst precipitation and source regions appear later in the thesis.

One of the reasons that chorus has so often been associated with microburst precipitation is that the regions of microburst activity are very similar to regions of chorus activity. Observations from CRRES (Meredith et al., 2003) identified chorus emission occurrence across the entire dawnside of the magnetosphere. Figure 4, an adaptation of these CRRES results (Bortnik and Thorne, 2007), shows the distribution of wave power at different latitudes for a variety of parameters of geomagnetic activity. Lower band chorus is most prevalent near the equator along the dawnside while closer to noon the wave power moves to further off the equator. Additionally, it is perhaps unsurprising that wave intensity picks up dramatically with increasing AE. A stronger AE index corresponds to more significant auroral currents being driven, which reflects additional free energy for waves on a local level. The AE index is a substorm index, as opposed to a strictly storm index. Much ink has been spilled about substorms and their differences from storms. I do not seek to get into a long and involved discussion of substorms and their qualities in this thesis. For the purposes of this thesis it is sufficient to note that chorus activity tracks quite well with AE. This trend in wave activity foreshadows the microburst observations, as is discussed in Chapter 2.

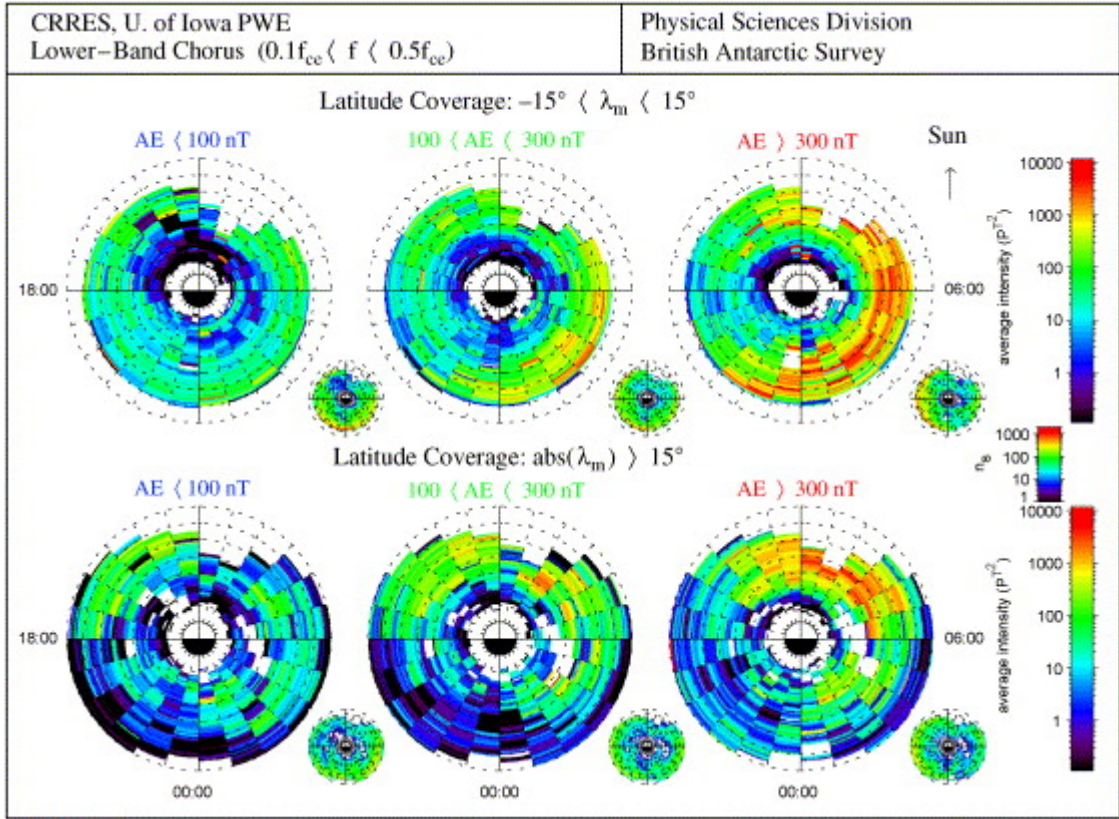


**Figure 4. Intensity distributions of lower-band chorus waves as a function of MLT, L for both equatorial and off-equatorial chorus (Bortnik and Thorne, 2007).**

Fundamentally, interest in wave activity is due to an expectation of a resonance between the waves and the particles. The conditions for resonant wave-particle scattering require that the Doppler-shifted wave frequency match a multiple of the relativistic electron gyrofrequency by the following equation (Thorne et al., 2005):

$$\omega - k_{\parallel}v_{\parallel} = \frac{n\Omega_e}{\gamma}$$

These parameters are of course functions of both particle properties (energy, pitch angle), and wave properties (normal angle, frequency), as well as local conditions (gyrofrequency, determined by magnetic field). Finding regions (in both physical and phase space) which match resonant conditions provides key

information about the processes and what governs their efficacy. Summaries of more recent work (Thorne, 2010) have suggested that these processes may be more complicated and involve non-linear interactions.

### **Thesis Objective**

The objective of the thesis is to understand the properties of and ultimately significance of microburst precipitation—ideally on a global level. While individual microburst events are localized probably in space and time, the fact that they can occur in large numbers and across broad regions, and repeatedly over time, leaves the total geo-effectiveness of microburst loss unresolved. This thesis will address issues of the size, distribution and impacts of microburst precipitation through a series of focus questions in order to make progress toward answering the ultimate question. They are:

- 1) How do microbursts vary/how are they similar?
- 2) What are the physical mechanisms involved in the generation of microbursts?
- 3) What is required to create the next set of microburst observations to make substantial progress in understanding?
- 4) What is the global scale of microburst loss?

Over the course of the next 4 chapters, each of these questions will be addressed in turn. The first two focus questions deal with understanding the relevant characteristics and qualities of the phenomena; the third deals with expanding the depth and quality of microburst measurements to advance the science. Finally, the results of these questions and analysis required to address

them are pulled together to address the final focus question, which serves as a capstone for the thesis. Truly and finally answering this last question requires measurements from newer data sets which are beyond the scope of this work; in this case the thesis sets out to address microburst characteristics and develop a guide for answering this question only upon the arrival of new data by the mission described in Chapter 4.

# **CHAPTER 2**

## **MICROBURST EVENT DISTRIBUTIONS AND INTENSITIES**

### **Motivation**

The aim of this chapter is to understand microburst events as phenomena and, by building up a significant database of events, to look for the similarities and differences that define microbursts as a population. In order to assess the significance of microbursts as a loss mechanism, it is first necessary to understand what exactly comprise the population of microbursts. Therefore, the objective is to assemble a large, comprehensive database of microburst events under a wide range of conditions. This section is based towards answering the first focus question: “*How do microbursts vary/how are they similar?*”

### **SAMPEX Data**

The data in this study comes from the HILT (Heavy Ion Large Telescope) on board the SAMPEX spacecraft. The HILT instrument (Klecker et al., 1993) was originally intended to study heavy ions, however, a few years into the mission, it was converted into an operational mode that was uniquely suited for microburst studies. HILT’s large geometric factor ( $60 \text{ cm}^2\text{sr}$ ) meant that it could generate sufficient counts in order to avoid challenges of small numbers looking artificially bursty. Starting in 1996, HILT was switched into a higher time resolution mode, which provided measurements at a 20ms cadence. This is ideal

for microburst science, since the instrument resolution is shorter than the characteristic timescale of a burst. Additionally, SAMPEX's orbit was well suited for microburst observations as its high-inclination ( $82^\circ$ ) and low-altitude (520x670 km) orbit means that the bounce loss cone becomes very large. The combination of these factors makes it easier to observe and identify microburst events and the long mission duration (over 15 years) ensures events under a range of conditions.

SAMPEX has been utilized before for microburst measurements [e.g. (O'Brien et al., 2003), (Lorentzen,Looper and Blake, 2001), (Blake et al., 1996), (Nakamura et al., 2000) (Comess et al., 2013)]. For the purposes of this study microburst identification was based on the identification algorithm utilized in O'Brien et al., [2003], which created a burst parameter and used that for event identification. The burst parameter is defined as:

$$MBP = \frac{n_{100} - a_{500}}{\sqrt{1 + a_{500}}}$$

where  $N_{100}$  is the number of counts in 100 ms, and  $a_{500}$  is the 500 ms rolling average of  $N_{100}$ . When the burst parameter (MBP) is greater than 10, it is considered a microburst. Additionally, a floor of 10 counts (in n) was utilized in order to avoid false positives due to Poisson noise. The principal definition of a microburst comes from the short time structure which is reflected in the time constants used for the microburst parameter. The particular implementation of the algorithm with the combination of linear and logarithmic elements was designed to be responsive to bursts at a range of different flux levels (O'Brien et al., 2003). The critical value of 10 in assessing a burst comes from that same

work, with a continuous range in values. Obviously, changing that value higher or lower would change things but it seemed to be the sweet spot in terms of event identification. In addition to using the automated algorithm, I spot-checked the algorithm under a variety of conditions and places within the data set to see that the events identified as bursts looked reasonable. Since this appeared to work, I extended the algorithm to the entirety of the SAMPEX dataset. SAMPEX did not reenter until November 2012; however after 2004, funding to maintain the public data archive disappeared. Fortunately, the instruments were not turned off, and The Aerospace Corporation continued to process some of the data files. Accordingly, although there were more data gaps in the post-2004 interval, I was able to work with a data set from 1996-2010.

### **Characteristics of Individual Bursts**

Combing through the data set with the use of the automated microburst identification algorithm resulted in a database of ~686,000 individual microburst events. An example of microbursts is shown in Figure 5. Here, a long series of microbursts is shown, centered at t=0 around a particular event. A number of characteristics jump out from this image, which will be explored in greater detail systematically. First, it is clear that microbursts can occur in substantial numbers in close proximity to one another. Secondly, not all microbursts are the same amplitude, as they have different size peaks. When thinking about the amplitude, this can be done either as a ratio of the peak to the nominal baseline flux, or as an integration of the total number of electrons contained within the event. Thirdly,

the duration of the bursts does vary; some have a naturally broader structure than others.

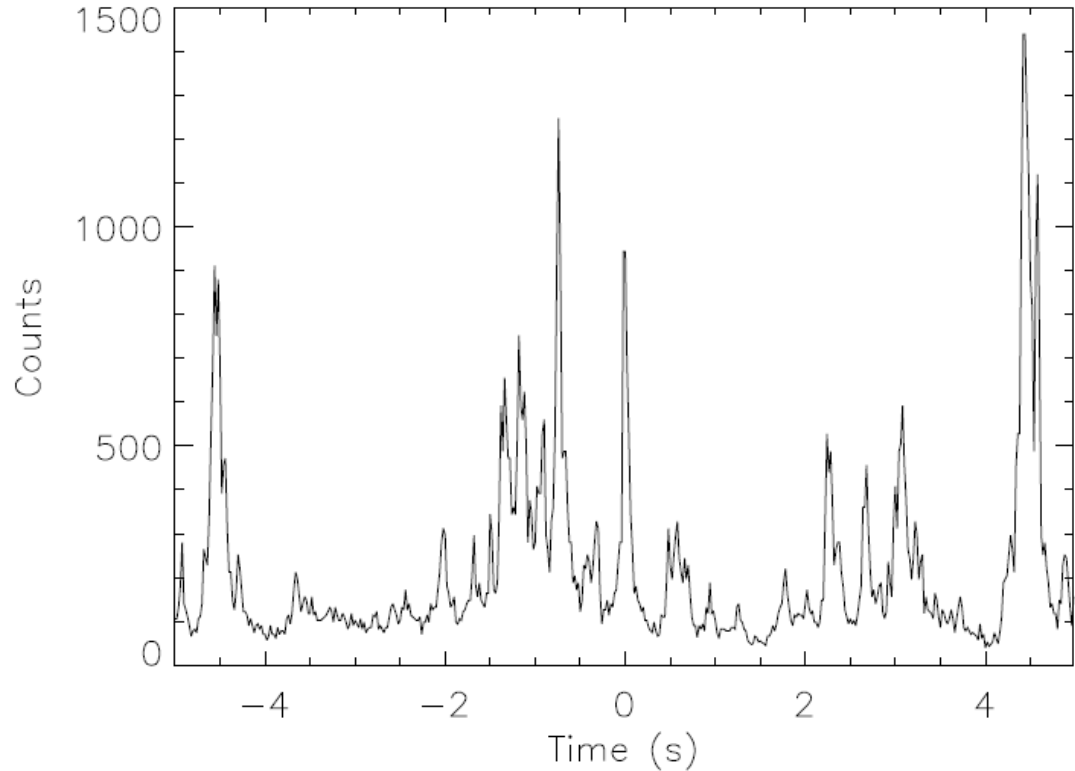


**Figure 5. An example of microburst events from SAMPEX. In this case, a long series of microburst events of various different sizes are shown. T= 0 corresponds to one particular microburst.**

In addition to studying the microbursts as a single population, the large data set suggested dividing it into subsets for further analysis. Since our underlying motivation is to understand how the radiation belts respond to storms, it seemed natural to look for differences associated with storms. For the purposes of a storm phase of the events, we identified 231 storm events that had a minimum Dst less than -50nT. Dst is an hourly measurement from equatorial magnetometer stations of the perturbation in the Earth's magnetic field (Sugiura,

1964). During a storm (and in fact at other times), particles are injected inwards from the tail. Electrons and ions experience opposite drifts in the Earth's magnetic field, and since they drift in opposite directions that gives rise to the ring current. This current in turn creates its own magnetic field which is oriented anti-parallel to the Earth's dipole field, and consequently the stronger the ring current is, the more negative the perturbation and thus a more negative (stronger) Dst value. The Dst index is thus often used as a proxy for the strength of a storm, and so a criterion of minimum Dst less than -50nT was chosen to select for storms of a certain strength. Each storm was then divided into a main and recovery phase based on a visual inspection of the Dst profile using hourly values. The end of the recovery phase was determined visually upon a return to 80% of the minimum Dst value. Storms were not required to be completely isolated (frequently a second storm occurs while the recovery from the first storm is ongoing). In that case, the two storms were treated as distinct with the new main phase starting on the drop in Dst. As these determinations were done by eye, there were naturally times when it was a judgment call. The relevant characteristics of microbursts during the main phase and the recovery phases were calculated using the total population of all main phase and all recovery phase events rather than on a per storm basis. This results in a description of an average main phase and an average recovery phase characteristics. At present, no distinctions have been drawn between CIR and CME driven storms, although this remains a topic for future inquiry.

A second geomagnetic index that is of interest is the Auroral Electrojet activity index, also known as AE (Davis and Sugiura, 1966). The AE index is calculated by measuring the perturbation in the H component (North-South) of the Earth's magnetic field at a number of stations in the auroral zone. AE is calculated as the difference between the maximum positive and maximum negative values; this range in magnetic field values is a measurement of the strength of the horizontal Auroral Electrojet since stations on one side will see an increase in field strength and those on the other will see a decrease. The AE index is of particular interest because it is a good measure of the strength of substorm activity at any given time.

### **Event Location**

For each event, the location was determined using the spacecraft ephemeris data, which utilized a dipole magnetic field to determine the location as a function of MLT, and dipole L. To create the frequency map of microburst locations we normalized the total number of measured events in each MLT-L bin by the total amount of time that SAMPEX spent within the given bin. This represents a long-term average of SAMPEX observations—owing to its orbit SAMPEX is only monitoring a small sector of local times during any given event. This map represents a composite image of where bursts are most likely to occur. Maps of microburst location by themselves are not a new result; past efforts with SAMPEX data have produced similar sorts of distributions (O'Brien et al., 2003) (Lorentzen et al., 2001). However, the key advance in this thesis is the sizable increase in statistics and the breadth of observations. Past work typically covered

only a few years of data from SAMPEX, whereas this work represents the most comprehensive data set, and therefore more detailed slices can be made.

Figure 6 shows the measured occurrence frequency of microburst events in each region over all conditions. From this we see that microbursts are distributed over the dawnside—from just before midnight to noon in local time, and 4 to 7 in L. We note that the peak frequency (most common occurrence of microbursts) is an approximately 2 hour section centered on 1000MLT. This distribution of microburst occurrence frequency is remarkably similar to distributions of chorus intensity such as reported by both CRRES (Meredith et al., 2003) and THEMIS (Li et al., 2009); regions of high microburst activity match those of strong chorus activity. Furthermore, breaking down the frequency by AE (as shown in Figure 7) heightens the comparison. For  $AE < 100nT$ , microburst activity is at very low levels (<4% of the total) and is primarily confined to near midnight in local time. As AE increases, the overall frequency of events starts to increase, with the overwhelming majority of events (>77%) occurring for  $AE > 300nT$ . Furthermore, at times of strong AE, the overall structure of microburst occurrence better matches the frequency of chorus, with the focus shifting to the post-dawn and pre-noon hours. Such a trend mirrors the trend in lower band chorus properties seen for the equatorial population (Bortnik and Thorne, 2007). The AE dependence on the overall level of microburst activity mirrors the trend of the overall amplitude of chorus wave measurements.

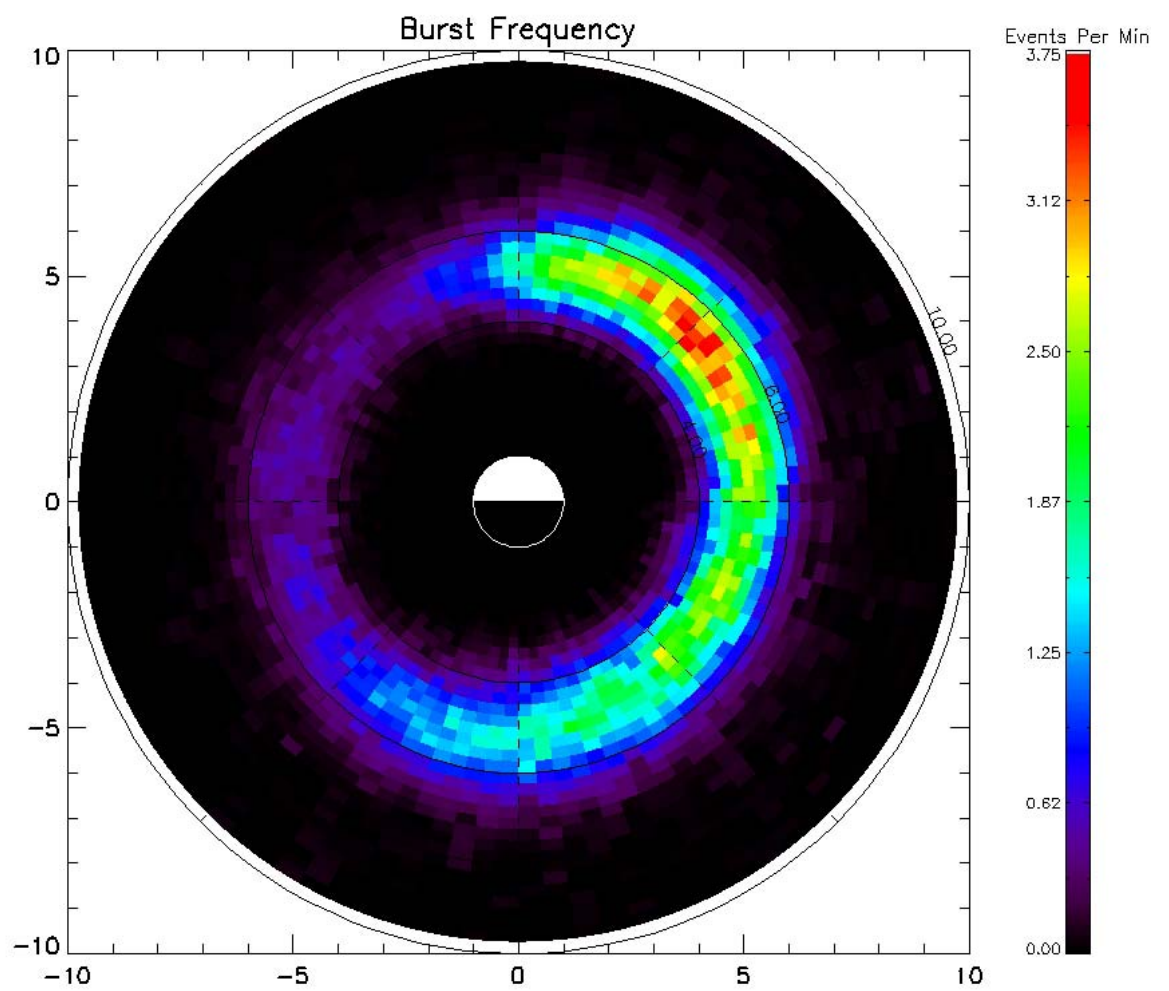


**Figure 6.** Event frequency as a function of MLT,  $L$  measured by SAMPEX.  $L$  ranges from 0 to 10, noon is at the top of the figure and midnight is at the bottom. This represents the average event frequency over the period 1996-2010. Event frequencies are measured as number of events observed per minute of observation within each bin.

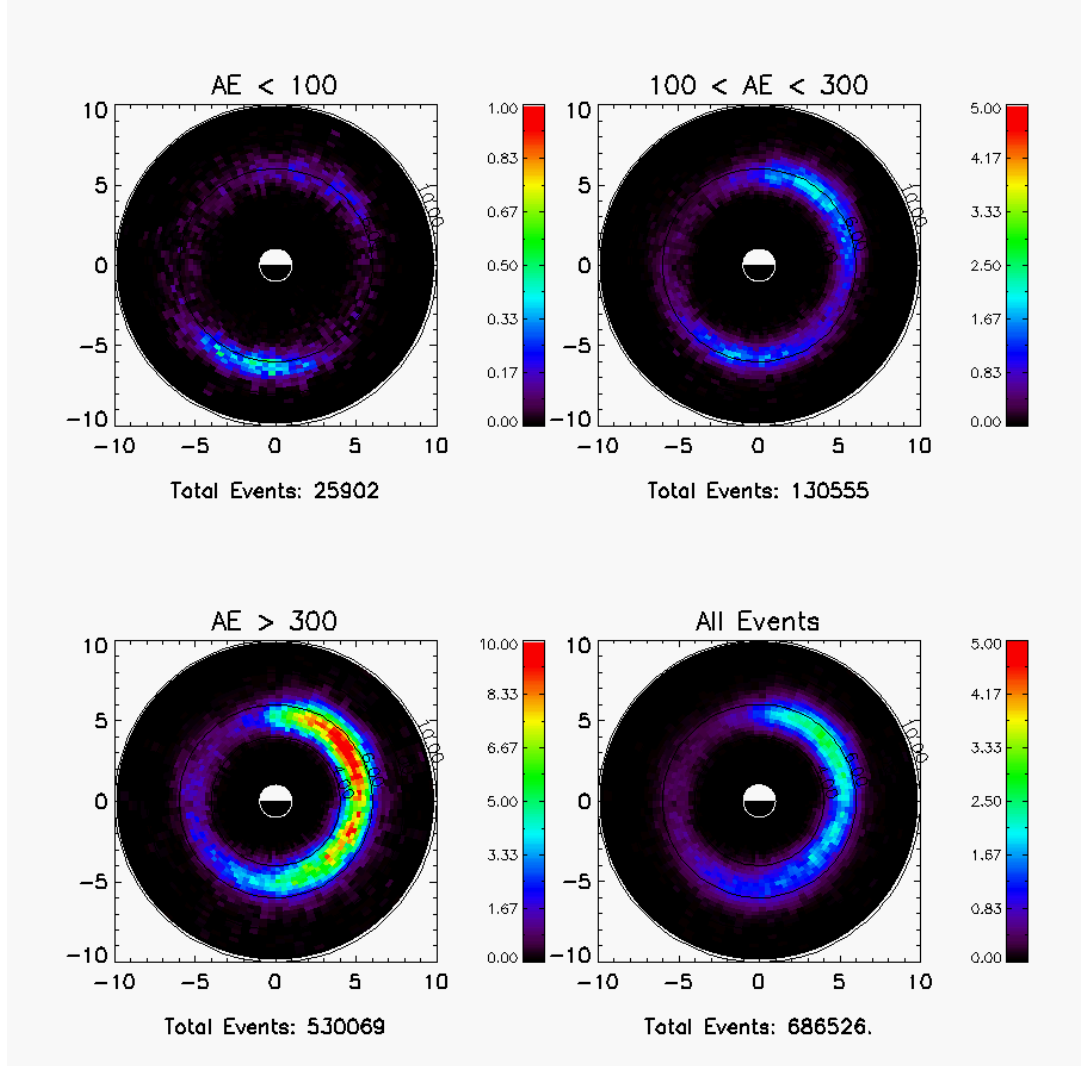


**Figure 7. Event Frequency as a function of AE, measured in events per minute of observation time with the corresponding AE levels. Overall event levels are dramatically lower during times of low AE, and are pushed towards noon and midnight.**

Using our database of 231 moderate storms selected by a minimum Dst criterion we examined the variation in microburst event frequency across the different storm phases. Figure 8 shows this variation in how event frequency varies across storm phase. Compared to the overall event frequency distribution, we see significantly elevated event rates during the main phase of the storm, while the recovery phase is slightly elevated. (Astute readers may wonder how this compares with results from O'Brien *et al.* [2003] which argued for higher

rates during the recovery phase. This difference comes from two factors: the first is that their frequency statistics were based on a binary variable—whether or not a burst occurred within a given pass, whereas ours counted the number of individual bursts. Secondly, this conclusion was based primarily on a comparison in the morning sector (post-dawn) where recovery events are most frequent while the main phase events are most frequent in the pre-dawn sector.) This trend is further emphasized if we restrict the storm database to only events with minimum Dst less than -100 nT in which case the event frequency during the main phase is even higher. In addition to the significant variation in overall frequency across storm phase, there are also structural differences in event frequency. During the main phase, not only is the overall rate of microbursts significantly higher, but the peak region for microburst activity is moved towards the pre-dawn sector, between 0300 and 0600 MLT. This is in contrast to both the recovery phase, and the overall composite picture which see the peak frequency as closer to 1000 MLT. The total number of events observed during the main phase of storms is still a relatively small fraction of the total (~10%), owing to the shorter duration of the main phase, which is perhaps why the overall distribution better matches the recovery phase picture. While microburst occurrence rates climb during storms, storm-time events (main + recovery phase) only represent 50% of the total database. Utilizing a definition of  $Dst > -20$  nT as a “quiet” population (although it can include the beginning or end of storms), we see that there is a very low level persistent microburst population (it also shows up in the  $AE < 100$  nT bin in

Figure 7). This occurs at much lower frequencies overall and appears to be better represented among the midnight and pre-midnight events.

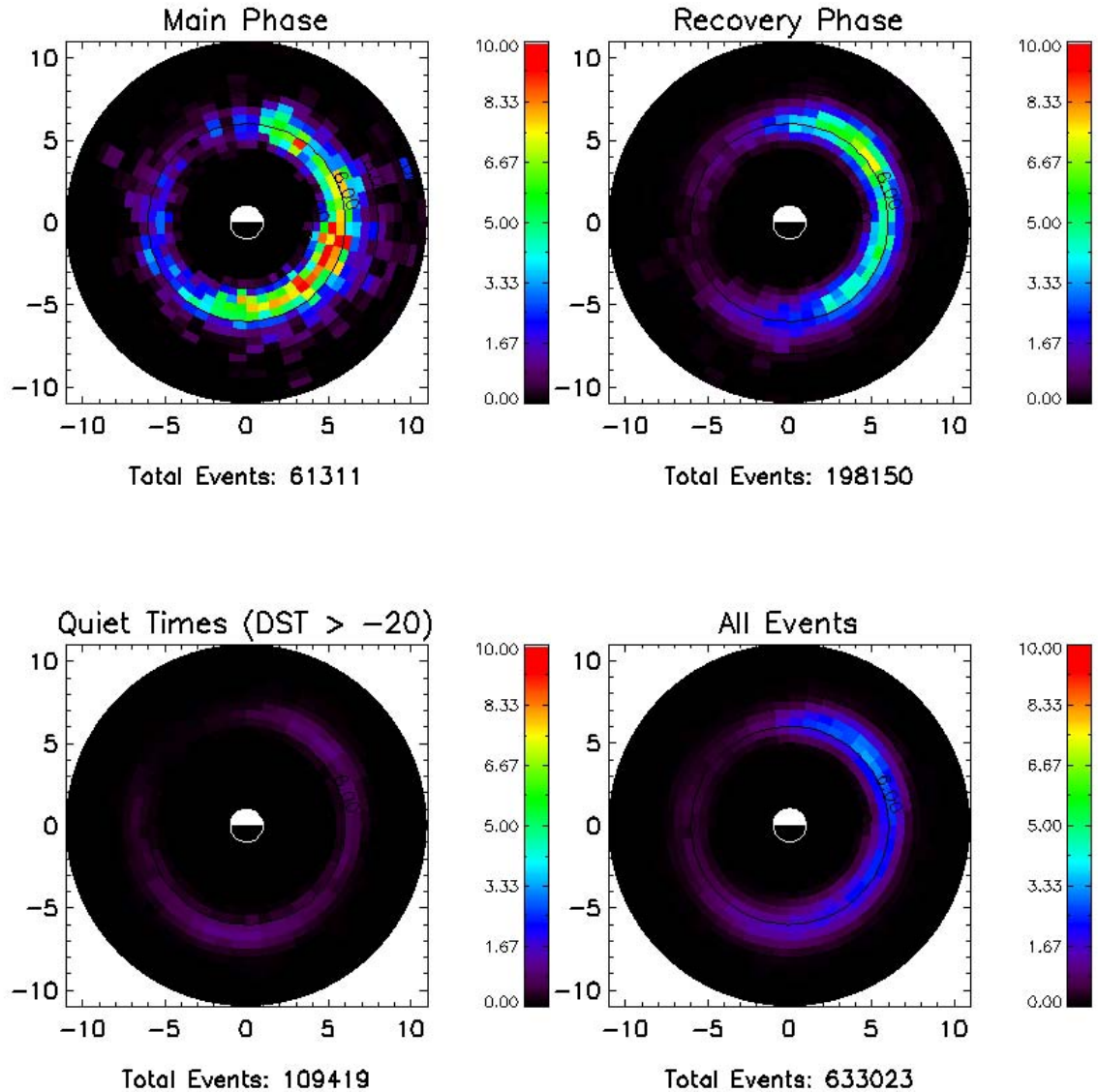


**Figure 8. Event frequency across storm phase, measured in events per minute of observation time. Quiet times encompasses all times with  $Dst > -20$  (even if it is the beginning or end of a main or recovery phase). Microburst precipitation is strongest during the main phase of storms, as well as shifted closer to midnight during these times.**

## **Event Intensity**

To measure the intensity of a given microburst we defined two different measurements. The first, termed “relative intensity,” was a measurement of the peak of the microburst relative to the normal background count rate (defined as the 10s median count rate), expressed as a ratio of the two. Large relative intensities map to times when there was a very large enhancement in flux, and plays an important role in determining the types of events that are observable—an important instrumental consideration. Additionally, the relative intensity likely serves as a proxy for the strength of the wave particle-interaction in terms of suddenly filling the loss cone. The second measure of event intensity was termed “absolute intensity.” Absolute intensity was a measurement of the total number of electrons that precipitated. Absolute intensity was measured by fitting the event profile to a Gaussian fit, and then subtracting off the background flux profile. The process for characterizing an individual event (absolute intensity and later duration) is shown in Figure 9. Absolute intensity serves as a tracer for the geo-effectiveness of electron precipitation due to microbursts, as summing the absolute intensity of all events would provide a method for estimating the total number of electrons due to microbursts globally.

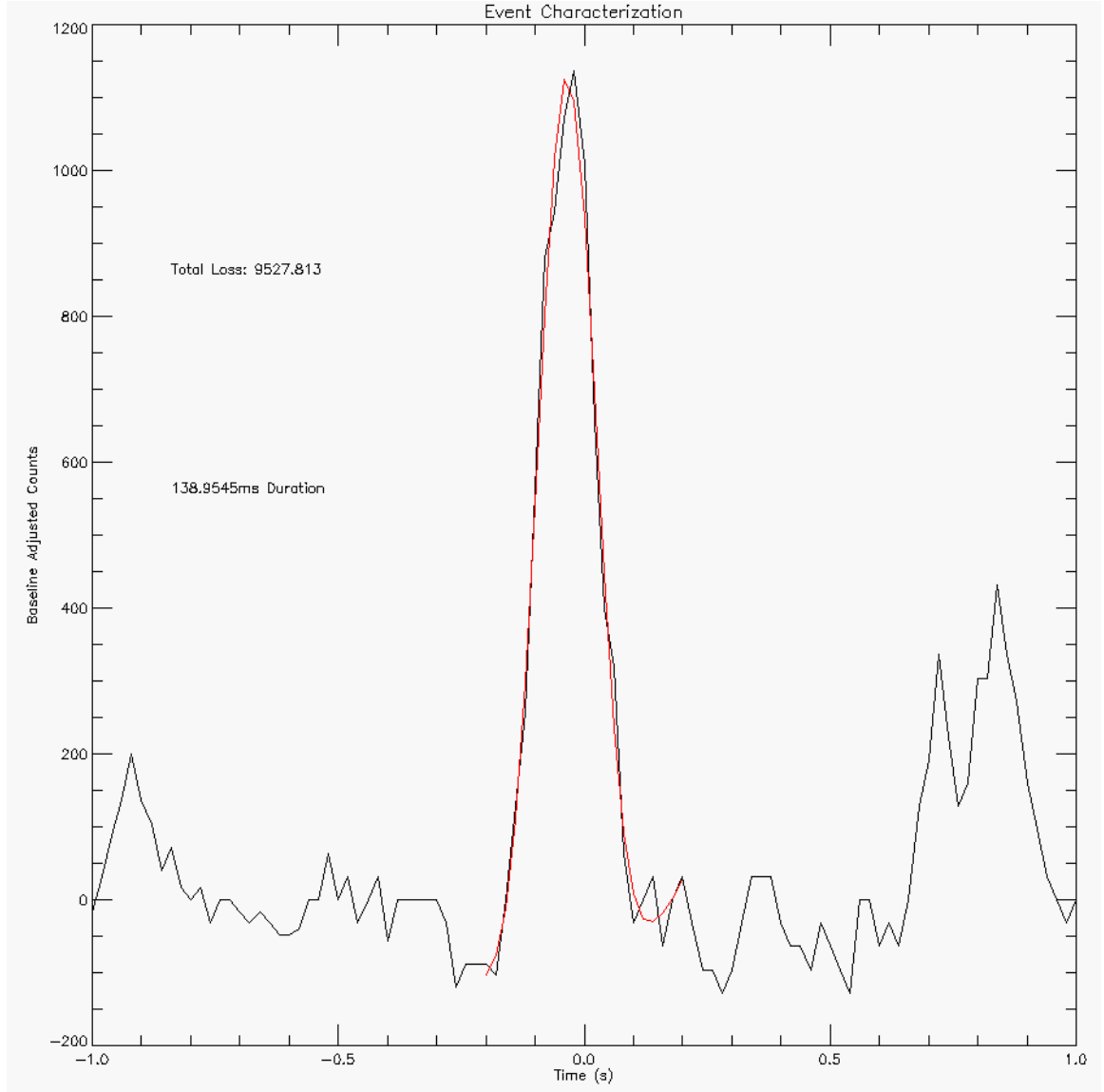


**Figure 9.** Event characterization for a single SAMPEX microburst event. First, the event has the background flux profile subtracted off to isolate the microburst. The black trace is that data, while the red is the Gaussian profile fit to the microburst event, from which the relevant characteristics (absolute intensity, duration) are extracted.

The relative intensity of microbursts observed by SAMPEX appears to be highly variable. As Figure 10 shows, the relative intensity for all events appears to follow a power-law distribution over several orders of magnitude in relative intensity. Furthermore, Figure 11 splits out the relative intensity profiles by AE bin. Across the different AE bins all appear as power laws, however falling off

with varying degrees of steepness. For the quietest AE intervals we see significantly fewer events with large relative intensities; conversely it appears that in order to generate the strongest events we require times of heightened AE.

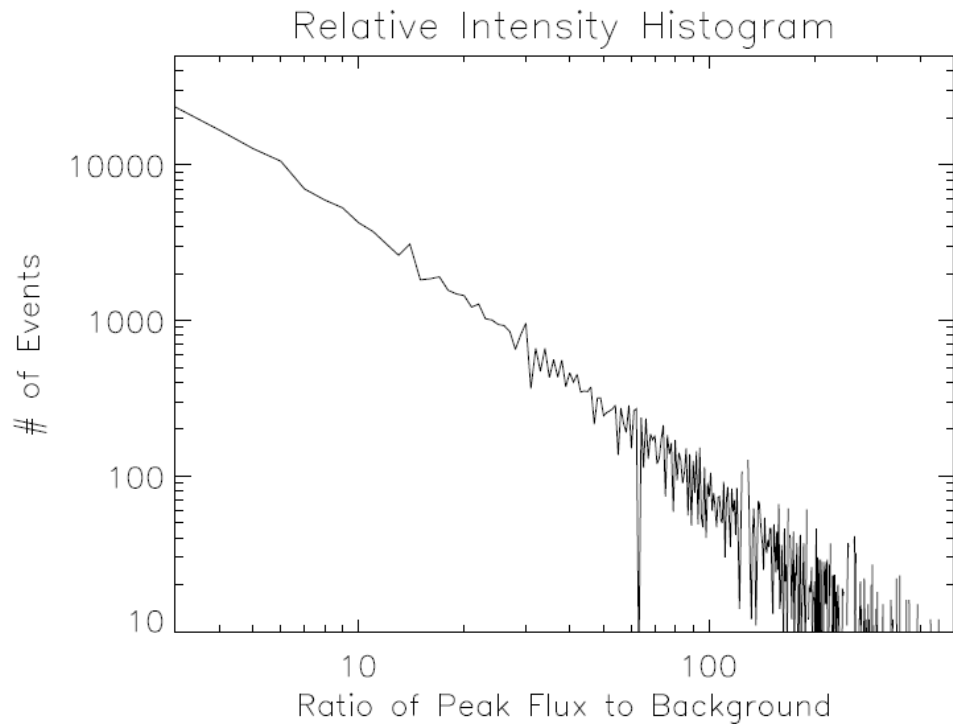


**Figure 10. Relative Intensity Histogram from SAMPEX for all observed events follows a power law spectrum over the entire observed range.**

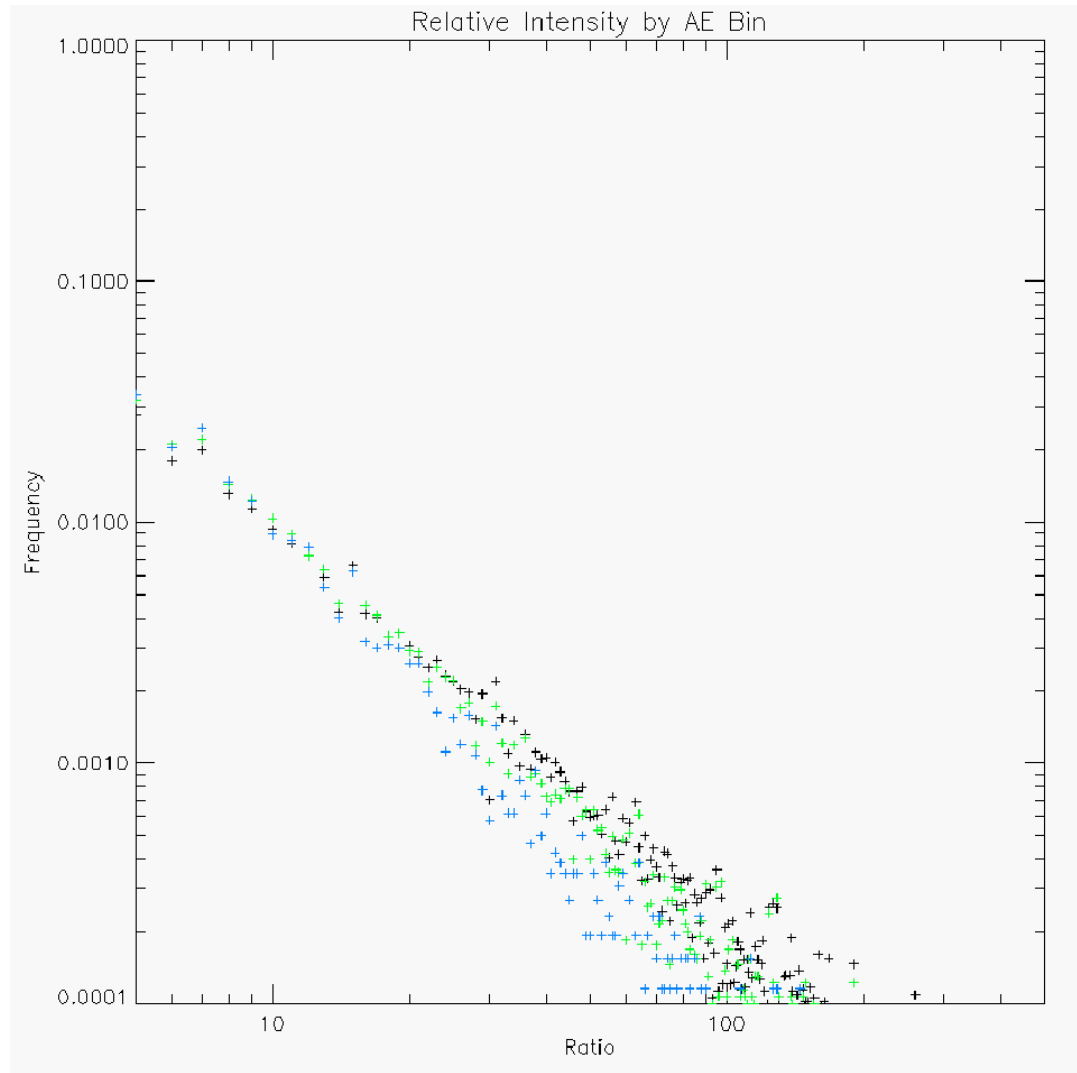


**Figure 11. Relative Intensity by AE bin. Blue is  $AE < 100nT$ , green is  $100nT < AE < 300nT$  and white is  $AE > 300nT$ . At lower AE relative intensity falls off more quickly.**

To map the locations of strongest peak intensity we binned events by MLT, L and then measured the average (mean) relative intensity for all events within a given bin. Figure 12 displays the resulting map of relative intensity across the different AE regimes. In the overall composite picture we see that the peak relative intensity typically occurs close to dawn ( $\sim 0600$  MLT) and that the average relative intensity weakens at both higher and lower MLT. As in the intensity histograms we do see that the strength of the events falls off at weaker

AE; while the effect is subtle for the bin of  $100 \text{ nT} < \text{AE} < 300 \text{ nT}$ , it is very pronounced in the “quiet” bin of  $\text{AE} < 100 \text{ nT}$  which shows both very few events and only very weak ones at that. We note that the distribution of events (as seen in the frequency plots) shows that the quiet time events primarily occurred near midnight (which has weaker events), so the structure of peak intensity for that regime makes sense. However, we note that across the more elevated AE bins, the shape of the relative intensity histogram remains constant, with a peak at dawn. It is also interesting to note that the region of peak microburst intensity (dawn) and the region of peak microburst frequency (post-dawn/pre-noon) appear to be separated by a few hours in local time.

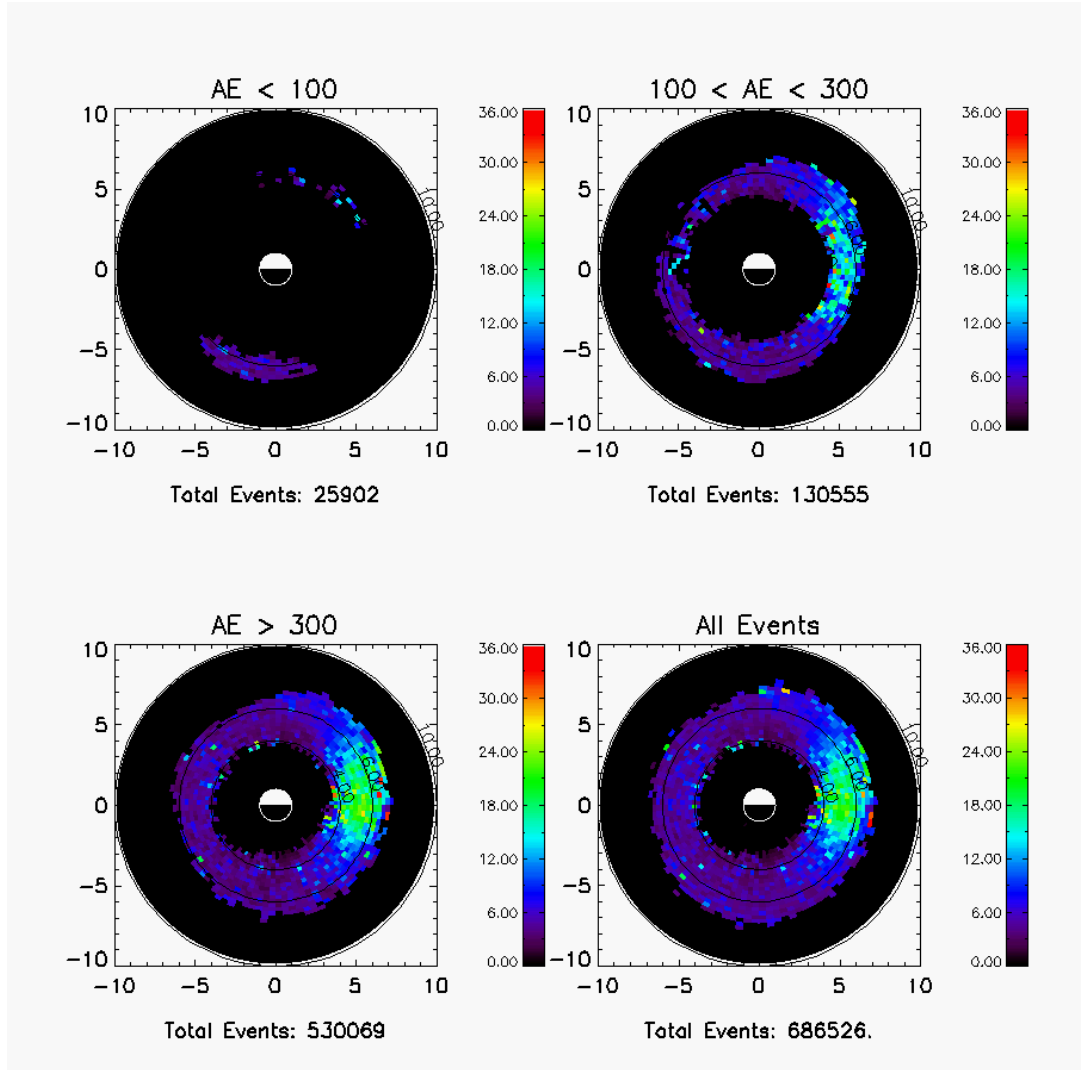


**Figure 12.** Relative mapping as function of MLT, L by AE bin. During the quietest times there are not enough events to draw meaningful conclusions from, but otherwise the peak in relative intensity still occurs closest to dawn and does not shift with increasing AE.

The variation in relative intensity across storm phase, however, is much less pronounced. Figure 13 shows the average relative intensity in different MLT, L bins for using the same categorization of storm phase as earlier. Once again, the peak relative intensity occurs at dawn with lower intensities seen at noon and midnight. There appears to be relatively little difference in the distribution of relative intensities across the main phase of a storm, or across the recovery

phase as compared to the overall distribution of relative intensities. This suggests that the chief difference in the microburst precipitation over the course of a storm results from the frequency and location of the bursts, as opposed to the magnitude and scale of the individual events. Such a conclusion has profound implications for total loss and will be revisited at length in Chapter 5.

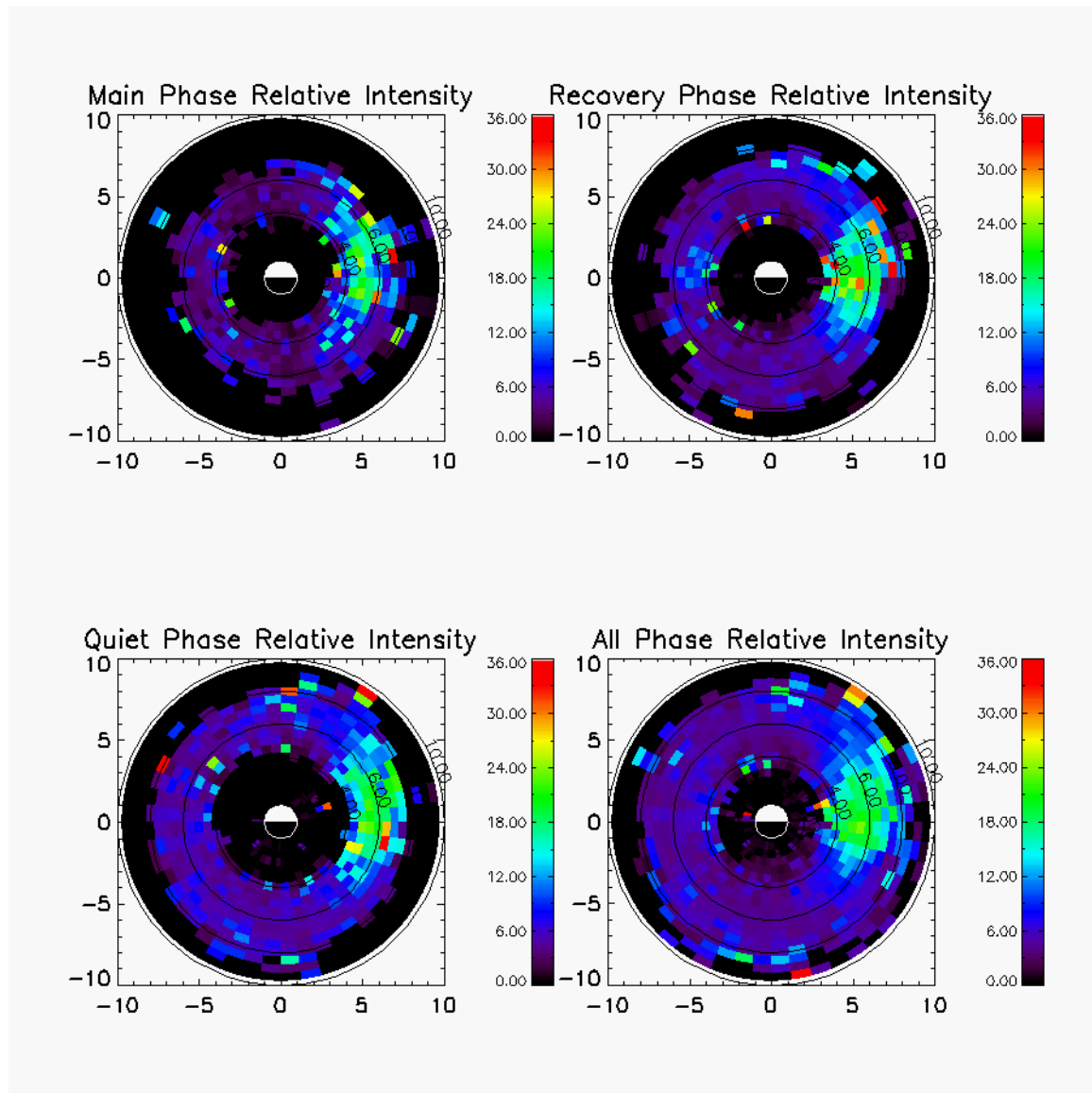


*Figure 13. Relative Intensity by Storm Phase. No matter what storm phase the peak relative intensity occurs closest to dawn, with seemingly similar values.*

Measurements of the total number of electrons lost, the absolute intensity, bear a striking resemblance to relative intensity profiles. While it represents a different physical quantity, absolute intensity shares a power-law like distribution in scale. As shown in Figure 14, however, the one main difference is that there is a smaller range in values for absolute intensity, roughly a single order of magnitude. Moreover, like relative intensity, when mapped in terms of MLT and L there is a similar pattern in strength. Peak absolute intensities are measured near dawn with weaker ones being measured near noon and midnight (as seen for the distribution in Figure 12) but the peaks are less tightly focused in local time than those of relative intensity.

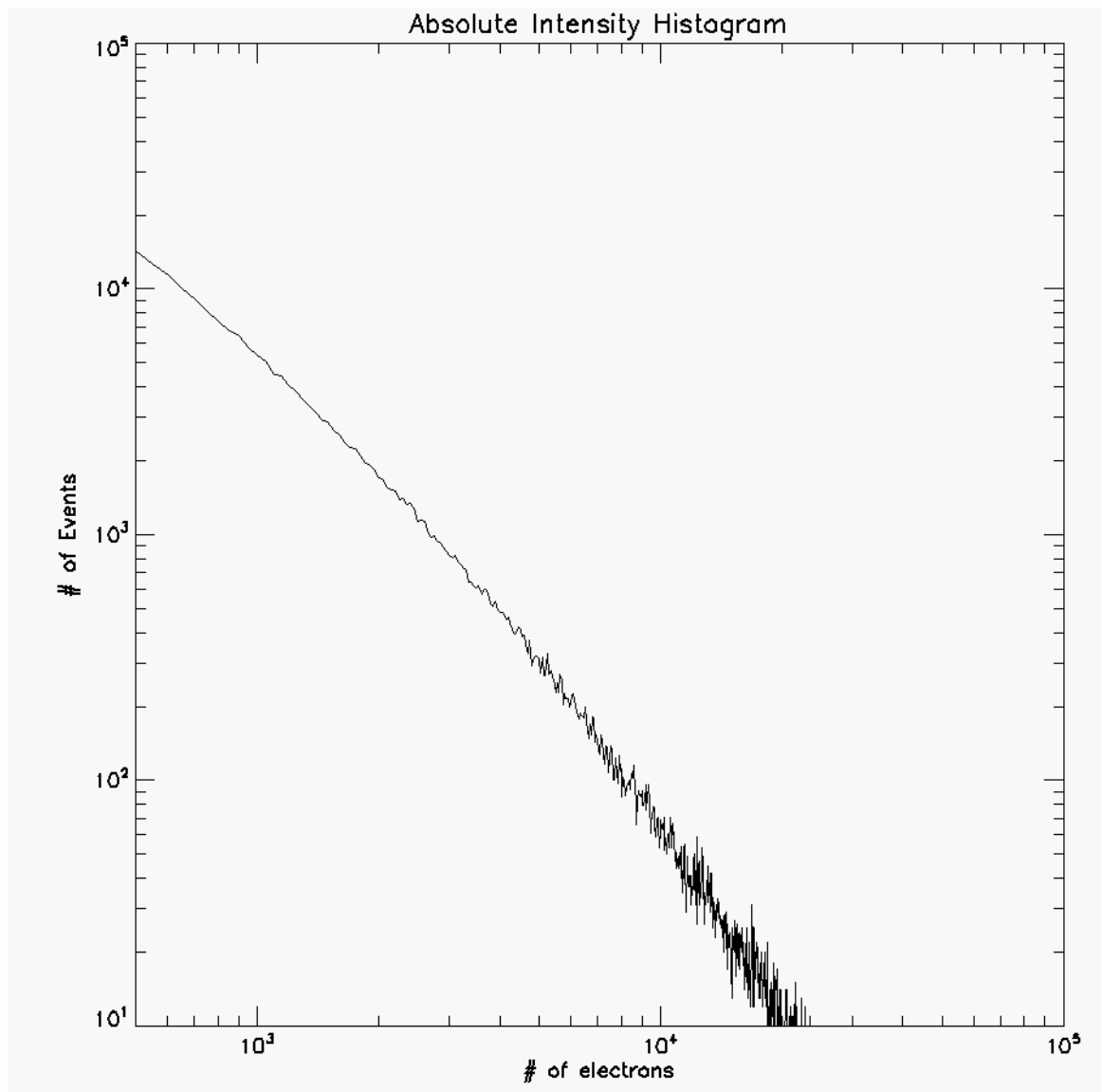


**Figure 14. Absolute intensity histogram.** Similar to the relative intensity histogram in showing a power-law like intensity distribution, albeit over a smaller range in values.

### Event Duration

Each microburst was fit to a Gaussian profile for analysis. Event duration was determined through extracting the characteristic FWHM of each event. The results are displayed in histogram form in Figure 15. The mean event duration was  $\sim 100$  ms with 60% of the events having duration between 50 and 150 ms. A check of the Gaussian profiles revealed that events typically matched the

Gaussian profile, however for some of the apparent longest duration events (~250 ms) the duration was artificial. Consequently, I assert that a typical timescale for microburst identification is 100 ms, and that the higher time resolution of SAMPEX (20 ms) permits exploration of event structure.

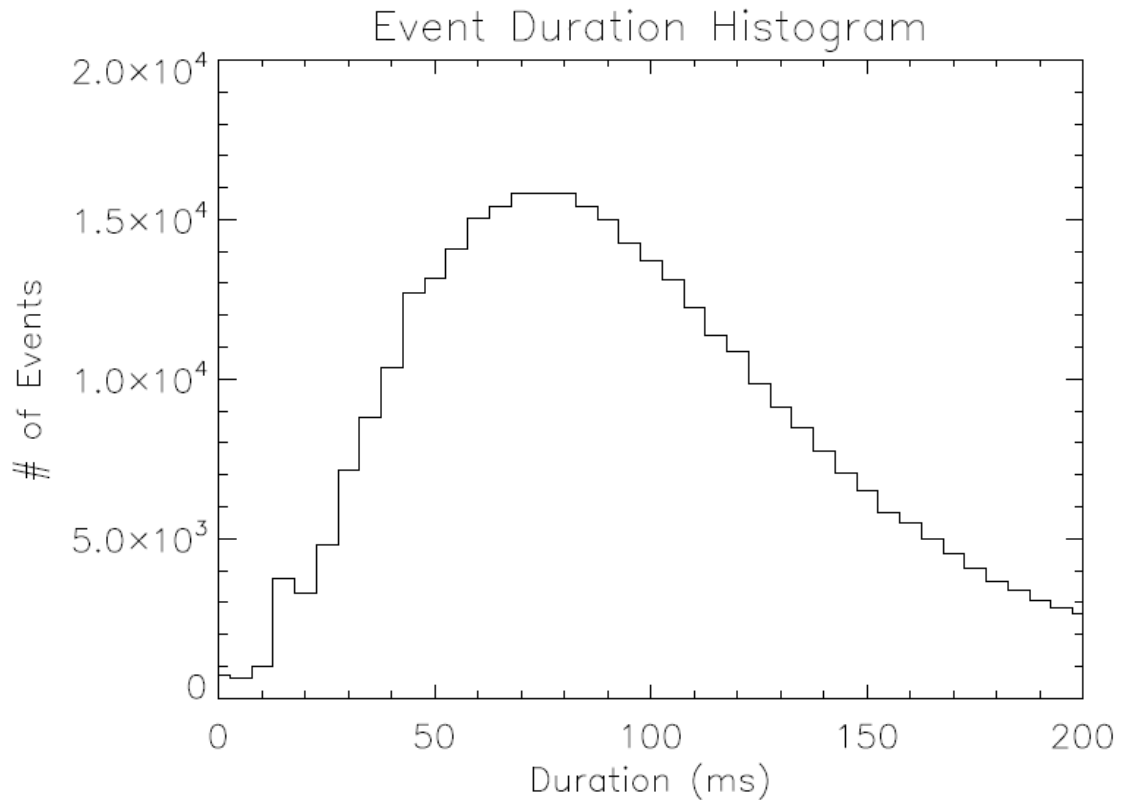


**Figure 15. Event Duration Histogram. Average microburst length is ~70 ms, with most falling between 50 and 150 ms.**

### Discussion

The depth and breadth of the SAMPEX observations of microbursts provide a window into the essential similarities and differences among microbursts. There are three major areas of interest worthy of further discussion raised by the characteristics of the bursts. The location distributions are important due to their strong links to VLF chorus activity and thus hint at causal mechanisms as well as addressing the question of when and where microbursts

occur. The intensity distributions address the question of how large is a given burst. Finally, the storm phase analysis is useful for addressing questions of how these results evolve over the course of a storm, which is important for understanding the geo-effectiveness of microbursts as a loss process among radiation belt dynamics.

### **Correlations with Chorus**

Observations of microbursts share many obvious similarities to those of chorus. Both phenomena exhibit strong similarities in local time distribution (morning side) as well as similar distributions in L. Moreover, past work (Lorentzen et al., 2001) has noted a correlation between times of enhanced chorus activity with times of enhanced microburst precipitation. Such a trend is also seen in binning microbursts by AE, as the sizeable enhancements in chorus activity (both power, and presence of larger amplitude waves) (Li et al., 2009) is replicated in measurements of microbursts. Statistically, microburst activity occurs over a very large range in local times, and possesses internal structure in event frequency. Of course, one important unresolved question is the difference between the instantaneous width (at any one moment, where are the bursts?) and statistical width (on the whole, where do we see them?) of microburst activity, something which can only be resolved by simultaneous multipoint measurements. The range in event frequency is another intriguing characteristic; during excited times the overall event frequency can jump almost an order of magnitude as compared to the average event rate. Likewise, there is a similar

drop in event frequency for the quietest intervals; however there appears to be a persistent low-level event occurrence rate.

The substantial increase in number of microbursts at times of high AE (and associated with large amplitude whistler-mode chorus) suggests that microbursts are an outgrowth of substantially disturbed local conditions. Chorus waves can be excited by lower energy ( $\sim$ 10s of keV) particles in unstable distributions (Hikishima et al., 2009). During times when substantial numbers of lower energy particles are being injected to the inner magnetosphere we would expect the pitch-angle distributions of these lower energy particles to become more anisotropic and thus provide the critical free energy to generate the chorus waves which in turn pitch-angle scatter the MeV electrons into the loss cone as microbursts.

Our understanding is that the generation mechanism of microbursts is an intensely non-linear interaction between the chorus waves and the resonant electrons (Hikishima, Omura and Summers, 2010). The implication is that there is a critical amplitude that is necessary to achieve the non-linear effects—which could explain the strong similarities between the distribution of highest intensity chorus and that of microbursts. Microbursts represent a pitch angle scattering of particles into the loss cone—however, large amplitude chorus waves should have other resonant effects. There is the potential to view microburst activity as a tracer for the presence of large amplitude chorus, which is capable of both scattering energetic electrons into the loss cone and energizing lower energy particles up to relativistic energies (Horne, Glauert and Thorne, 2003).

The underlying principle is that interactions require some sort of resonant interaction. Microbursts tell us that the resonant conditions are met somewhere (more on this in Chapter 3). So if a burst occurs, that means that the resonant conditions were met, and therefore information about the conditions under which events occur (i.e. location, AE dependence) provides information about the conditions under which these resonant conditions can be met. Under resonant conditions, a particle's motion matches that of the wave properties so that instead of seeing an oscillating field (as the wave appears to an observer on Earth) the particle instead sees a constant field. Chorus waves have typical frequencies of a few kHz, which is approximately the same as the gyrofrequency of a radiation belt electron (in fact chorus frequencies are linked to the electron gyrofrequency). Consequently, if the motion of the particle is such that it can match frequencies, it allows the particle to see a constant field giving rise to the interesting interactions.

### **Intensity Distributions**

There are two interesting facets of the intensity (both relative and absolute) distributions observed in the microburst data. The first is the local fact that microburst intensities fall off like a power-law spectrum. There are substantially more events at relatively low intensities, as compared with larger spikes. From an instrumental standpoint, the relative intensity distribution provides a way to estimate the efficiency of observation, as events with larger relative intensities will naturally be easier to observe. However, for estimates of the total loss due to microburst precipitation, it is the absolute intensity that is the

important characteristic, which means that in order to determine an average number of particles precipitated it is necessary to weight the distribution.

The local time distribution of the relative intensity also raises some interesting questions. As shown in Figure 12, the peak relative intensity occurs directly at dawn, and the average relative intensity then falls off as we move towards both noon and midnight. By contrast, the peak event occurrence frequency (number of events), occurs several hours later and closer to noon in local time. This discrepancy raises questions about the underlying physical process. For instance, are the criteria responsible for determining if a burst can occur (perhaps a function of resonance conditions) different from the criteria that determine the size of burst (perhaps a function of the local electron population and wave amplitude)? We know that there are differences in the observed properties of upper band and lower band chorus waves (Li et al., 2009) in frequency range, location, and mean amplitudes, and so it is conceivable that these microburst characteristics are a reflection of the differences in wave properties.

### **Storm Phase Analysis**

As shown in Figure 13, the event frequency varies dramatically across storm phase; the main phase sees an enhancement in event frequency as well as a shift in the location of most frequent events to earlier on the dawnside. From a location standpoint the interpretation here is that during the main phase of the storm, particles are being injected from the tail to create the unstable particle distributions in order to create the waves necessary to pitch angle scatter the

MeV electrons through microbursts. This causes the location of peak frequency to move closer towards the tail as we see more microbursts occurring closer to midnight. Additionally, the overall event frequency is much higher during the main phase of the storm than during the recovery phase, which itself is much higher than the overall event frequency.

However, although the event frequency changes dramatically across storm phase, the event intensity distributions (relative and absolute) show little change between events that take place during the main phase or the recovery phase as compared to the overall population. While we see some differences in largest strength events with respect to AE, the storm phase appears to have relatively little effect in terms of the strength of the individual events. If we return to the motivating question of the geo-effectiveness of microburst induced precipitation loss of radiation belt electrons, we would therefore conclude that the driver for total loss across storm phase appears to be the number of events and the frequency with which they occur, as opposed to differences in the particular events. Owing to SAMPEX's orbit, we only sampled a small swath of local time during each individual storm, however summing over the large number of storms in the period provides a method for covering all of the local times. If the total loss is driven by the number of events, than it would suggest that monitoring the frequency of total events at multiple local locations simultaneously (or perhaps through use of proxies) would provide a way to better estimate and constrain the total loss due to microbursts. This suggests that the problem of total loss due to microbursts can be separated into the twin problems of when and where the

bursts occur, and what the effects of a single burst are. When and where is a question of event frequency; the effects are a question of intensity distributions. These results motivate and serve as the jumping off point for the work in Chapter 5.

### **Conclusions**

The objective of this section is to take advantage of the length and breadth of the SAMPEX observations of microbursts in order to assess the notable characteristics of the events, both in terms of usual values as well as in their variability. Phrased alternatively, it gets at the question of “*How are microbursts similar/how do they vary?*” The observations from SAMPEX encompass an entire solar cycle, as well as over 200 different storm events (plus the quieter times in between). While many of these observations have been attempted before with subsets of the data (e.g. (O'Brien et al., 2003) or (Lorentzen et al., 2001)), this thesis represents a more comprehensive extension of the study to all of the available data. In terms of location, microbursts occur all along the dawnside of the magnetosphere, from midnight until noon, primarily between L shells of 4 and 8. These observed locations are co-located with normal regions of intense chorus activity (outside the plasmapause, at dawnside local times). This type of a study does not permit a search for 1-to-1 correlations between individual chorus elements and individual microburst events, so we are forced to rely on broader links and correlations. Like chorus, microburst activity is heavily tied to AE, as at the quietest times by AE, microburst activity is very low while >75% of all events occurred for AE > 300 nT. As this sorting is not nearly as intense or obvious

when events are binned by Dst instead, it suggests a more local mechanism for event frequency.

Event intensity distributions were also studied heavily. The relative intensity of events (ratio of peak flux to normal levels) is of considerable interest for event identification. This was utilized heavily for instrument design in the FIREBIRD mission (discussed further in Chapter 4). Additionally, searching for the strongest events provides some clues about the event mechanisms, as it is curious that the peak in event intensity (strongest events) occurs closest to dawn, while the peak in event frequency (most common events) occurs closer to noon (~1000 MLT) in local time. This ~3-4 hour discrepancy is interesting and suggests that the factors controlling event size and event frequency may be different. A similar analysis is repeated for the ‘absolute intensity’ (total number of electrons lost). Interestingly enough, when compared across different storms, there does not seem to be significant differences in event intensity, just in the event frequency.

Lastly, microburst event durations were compared across events. The event duration is of principal interest from an instrumental standpoint as it really sets what the instrument resolution must be in order to see microbursts—which can be a significant challenge. As discussed further in chapter 4, the event duration sets both the timescale for event identification (100 ms), as well as the resolution desired to probe event structure (~20 ms, but ideally even higher). Additionally, we note that the event durations are very comparable to the durations of individual chorus elements.

# CHAPTER 3

## MAPPING THE SOURCE REGIONS

### Motivation

It is easiest to measure microbursts at low altitude. In the case of spacecraft measurements, low altitude means that the atmospheric loss cone becomes very large, making it correspondingly easier to detect significant enhancements in the precipitating population, which would be only a small fraction of the total population in the heart of the belts. However, measuring microbursts at a location that is outside the radiation belts themselves means that the observations are typically separated from the location of the generation of the events. Mapping backwards along the event path from the point of microburst identification to the source region provides information about generation mechanism of microbursts and permits constraints on theoretical predictions which should enhance our understanding of the conditions which give rise to significant microburst precipitation. This chapter focuses on addressing the focus question, “*What are the physical mechanisms involved in the generation of microbursts?*”

### Theory of Microburst Generation

The current understanding in the field is that microbursts are caused by a non-linear interaction between whistler-mode chorus waves and the particle populations (Thorne, 2010). However, such a description still leaves considerable

details unresolved and needing further analysis and assessment. As was discussed in Chapter 2, there are significant overlaps between the regions of microburst activity and those of strongest chorus wave presence. Furthermore, as previously noted, the literature has also seen links between observations of higher frequencies of microburst precipitation being associated with times of enhanced chorus activity [ (Lorentzen et al., 2001), (Imhof et al., 1983)]. Thus links between microbursts and chorus appear both in temporal and spatial correlations.

A number of theories related to wave activity have been advanced for microburst generation. All of them rely on some form of wave-particle interaction to scatter electrons into the loss cone and produce the precipitation but the timescales involved represent a significant challenge. *Lorentzen et al.* [2001] advanced a theory of cyclotron resonance between VLF chorus and energetic electrons as responsible for the events. This interaction was defined by the following resonance condition:

$$\omega + k \cos \theta v \cos \alpha = \frac{s\Omega_e}{\gamma}$$

In this relation,  $\omega$  is the wave frequency,  $k$  is the wave number,  $\theta$  is the wave propagation angle,  $v$  is the electron velocity,  $\alpha$  is the electron pitch angle,  $s$  is an integer,  $\Omega_e$  is the unsigned electron gyrofrequency, and  $\gamma$  is the Lorentz factor. This relation combines factors that depend on wave properties (frequency, wave number, propagation angle), with particle properties (energy/velocity, pitch angle), and characteristics that combine electron properties with the local environment (electron gyrofrequency).

These properties can be combined into parameterized maps of the location of the resonance zone. Figure 16 shows estimates of the resonance zones for observations made by SAMPEX (Lorentzen et al., 2001). The orange band represents the range in chorus frequencies observed by POLAR around that time, while the dashed line indicates the particle energy ( $>1$  MeV) observed by SAMPEX. In the top panel, most of the conditions are held constant, while the magnetic latitude is varied in the different traces. In the bottom panel, an equatorial interaction is assumed, and higher order resonances are plotted. A few items of interest stand out from the plot. The first is that for this type of resonance condition, there is a strong source latitude/energy effect. For a given wave mode, higher energy particles resonate at higher source latitudes. Secondly, at a given latitude higher energy particles will resonate with higher wave modes. Moreover, although the resonant energy can be increased by going to higher latitudes or to a higher wave number, there is a lower energy cutoff for a given  $(\theta, N, L)$  which is the value at the magnetic equator. Obviously this is dependent upon wave frequency, but energies of  $\sim 10$  keV appear to be near the cutoff. The search for resonant regions is not limited to a particular interaction process; rather it is a way of trying to understand how an interaction process leads to a spatial distribution of event frequencies.

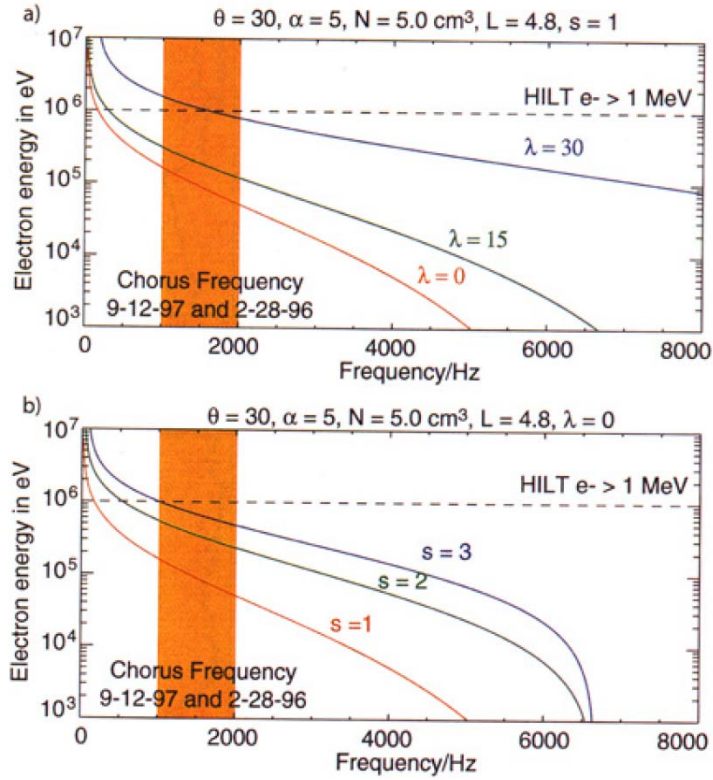


**Figure 16. Prediction of resonance zone for electrons for a variety of conditions.**  
**Top panel holds wave normal angles constant and looks for a first-order resonance at a variety of magnetic latitudes with MeV energy particles seen on SAMPEX. Bottom panel looks for resonance at the equator using higher order resonances (Lorentzen et al., 2001).**

Much effort goes into calculating regions for resonant interactions under a wide range of conditions (Ni and Summers, 2010); this is not intended to be an exhaustive description of the problem. Figure 17 shows another calculation of resonant regions for the interactions of electrons with chorus waves. All of the plots draw contours of magnetic field lines in black, with red indicating the resonant regions (the dotted lines are lines of magnetic latitude,  $\lambda$ ). The top half of the panels are for a wider range in chorus frequencies (corresponding to upper and lower band chorus), while the bottom panels represent a narrower frequency range (only lower band chorus). Two different energy particles are shown, 200

keV and 1 MeV electrons. Finally, the equatorial pitch angle and the second invariant ( $\kappa$ ) are varied. Immediate trends that jump out are strong variations in resonant latitudes with particle energy, while that latitude also changes as a function of L (higher latitudes at greater L). Interestingly, in some areas the resonant regions for the two populations are the same, and in other areas the waves are only resonant with particular energies. If microbursts are seen as an indication that somewhere the resonant conditions were satisfied, that could suggest reasons for variable breakpoints in the energy spectrum. Some places (or times) would see different ranges of valid energies. The search for resonant regions is important because that represents where a first order interaction has a particle seeing a constant field, rather than an oscillating one.

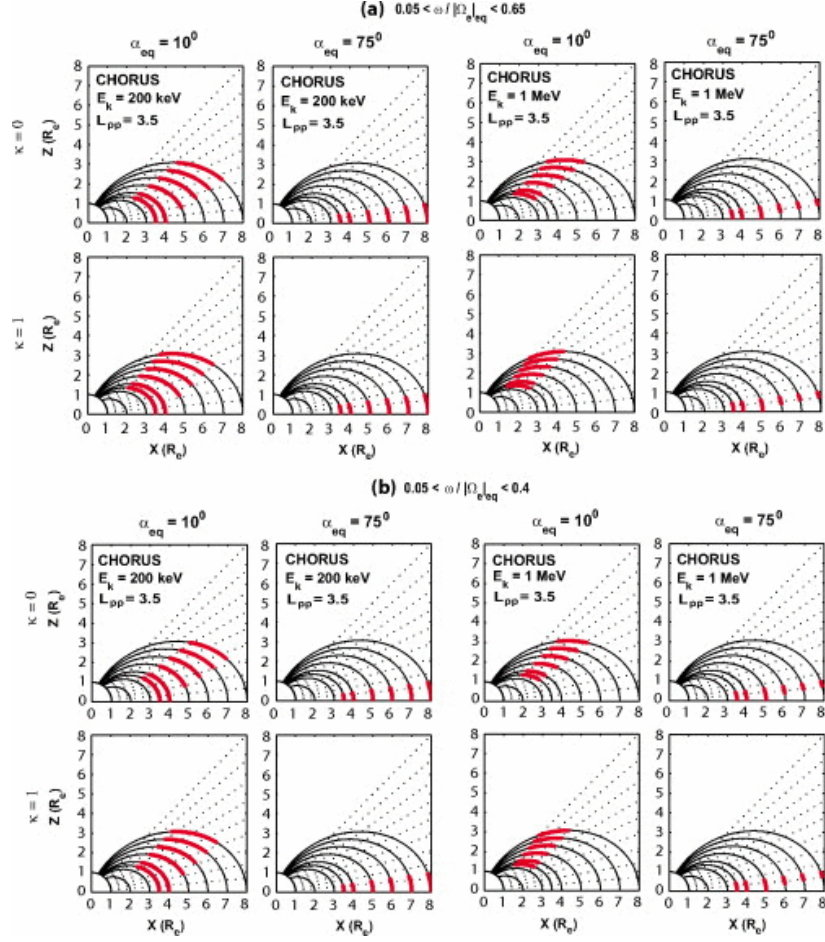


**Figure 17. Resonance zones in  $L$ , magnetic latitude for interactions with chorus at different equatorial pitch angles and energies. The red indicates the resonant regions at different  $L$  values (Ni and Summers, 2010).**

The objective of this study is to try understand the resonant interactions that are responsible for producing microbursts, and specifically microburst precipitation. While there may be differences in the precise location and resonances between MeV, and keV type level energies, there likely are a good number of similarities (as will be further discussed). While the SAMPEX observations dealt mostly with MeV level microbursts, there are other data sets which look at lower energy particles.

Modeling results also play an important role in the discussion of the underlying theory behind microburst generation. As of yet, there has not been a

recorded instance of an observed 1:1 correlation between a measured chorus element and a single microburst. However, this has been measured in complex modeling results. A very large particle simulation (Hikishima, Omura and Summers, 2010) modeled the interaction of large numbers of cold electrons with an energetic electron population with a loss-cone distribution. This simulation, using an idealized magnetic field geometry and an interaction region confined to the magnetic equator, was able to produce first individual chorus elements and then short bursts of particle precipitation on the same timescale as microbursts. These microbursts were of the energy range 10-100 keV; a lower energy range than studied earlier in the SAMPEX data set, but one closer to the focus of this chapter. It is interesting to note that it implies that the generation of microbursts is due to a non-linear wave particle interaction as opposed to quasi-linear theory which was used to produce some of the above estimates of resonance locations (Lorentzen et al., 2001).

### Freja Data

The measurements of electron microbursts used in this study were obtained using the F7 Electron Spectrometer (Boehm et al., 1994) onboard the Freja spacecraft. The Freja spacecraft operated in a 600 by 1750 km orbit inclined at 63 degrees to the equator. This orbit meant that it was able to easily measure the full loss cone of the precipitating particles. The F7 Electron Spectrometer on Freja consisted of a ‘top-hat’ electrostatic analyzer that measured electron distribution from ~20 eV up to 25 keV. The observed microburst features terminated around 5 keV, rendering the working energy

range for this study ~5-20 keV (since the highest energy channel was not always available). Furthermore, each measured energy channel was recorded into 18 distinct pitch angle bins at a time resolution of 32 or 64 ms depending on the instrument operation mode. By assuming a high-altitude electron source and a delay due to the time of flight from the particle source we expected to resolve characteristic velocity dispersion within a single event owing to faster particles reaching the instrument before slower ones.

This work extends the analysis of a single burst based off the time of flight analysis from *Clemons et al.* [1994] to a larger set of microbursts. Figure 18 shows the measurements from Freja in the selected energy channels and pitch angle bins for a series of microbursts. The delay between the most energetic and least energetic particles is evident from the curved shape of the bursts. Using a median filter and a convolution analysis we obtained the delay between the burst peak in each channel and when the burst was first seen in the highest energy channel. Figure 19 shows how that structure is turned into a distance by plotting the delay against the reciprocal of the velocity with the slope providing the distance traveled. This calculation assumes a single particle source which scatters all of the electrons into the loss cone simultaneously. Of the 18 pitch angle bins used by Freja we selected the particles recorded in the six most field-aligned bins as representative of the loss-cone population. We then trace this distance back along a dipole magnetic field to calculate a source location for the event.

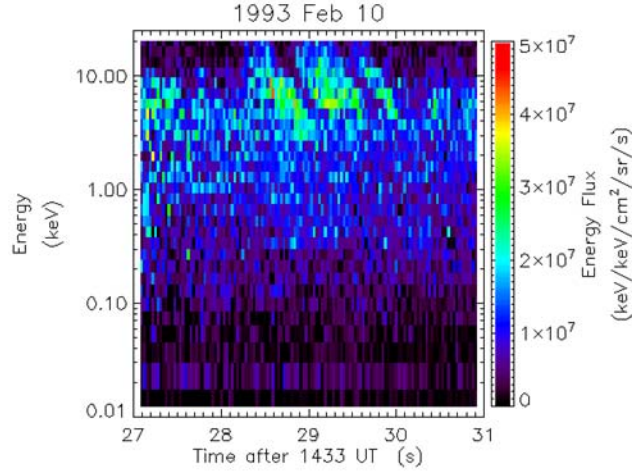


**Figure 18.** Microbursts observed by Freja. Three microbursts are observed starting at the maximum energy of 25keV and terminating around 5keV. The curved shape of the bursts is indicative of the time of flight effects whereby the most energetic particles reach the detector first.

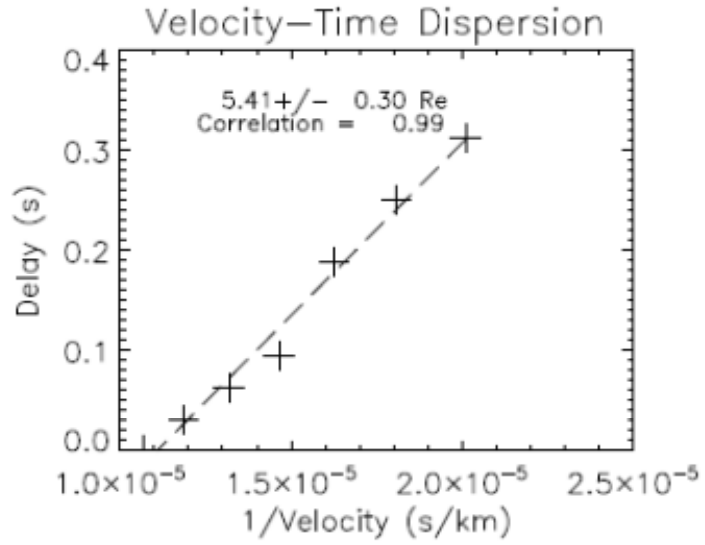


**Figure 19.** Distance determination of a microburst event using the dispersion within a single event and a time of flight analysis to determine the source region. For each channel the delay between the arrival of particles of that energy and that of the highest energy particles is plotted against the reciprocal of its velocity in order to determine the distance traveled.

To draw conclusions about the source regions of the events we extended the microburst analysis from a few events to those from the entire data set for the

Freja F7 electron spectrometer, which covers January 1994 to September 1995. In order to do this, it was necessary to automate the burst identification process. To identify bursts we established two characteristics of microbursts that a prospective event would have to meet in order to be classified as a microburst. The first requirement was that the event had to have the characteristic short time scale of flux enhancement seen in microbursts. This was done by defining a parameter, called the Burst Parameter, which served as a proxy for the short term variability in the electron flux. This parameter was modeled on work on SAMPEX's relativistic electron microbursts (O'Brien et al., 2003), and was defined as:

$$BP = \frac{n_{125} - \text{Baseline}}{\sqrt{1 + \text{Baseline}}}$$

Here  $N_{125}$  is defined as the number of counts in 125 ms, and the baseline is the larger of the 10 second or 1 minute running average of  $N_{125}$ . Obviously this is very similar to the definition used in Chapter 2 (since it comes from the same source), but some of the time constants have changed.  $N_{125}$  is now based on 125 ms due to the timing cadence of the instrument, and the longer baseline was chosen due to peculiarities of the instrument and lower count rates. Like with the SAMPEX data, this algorithm was also spot-checked by eye. We chose the variable form of the baseline to account for periodic drop outs of data which could skew the short term averages. Furthermore, for many of the events the fluxes are weak so a longer baseline reduces the impact of low fluxes looking artificially bursty due to the small numbers involved. Our definition of microbursts required that the Burst Parameter exceed 10 during the event. Consecutive sweeps (at

32ms or 64ms time resolution) with a Burst Parameter greater than 10 were classified as a single event, whereas if the Burst Parameter dropped below 10 in the middle it was then classified as multiple events. This process identified a large number of potential microburst events. The second characteristic that we used for identification was the energy structure of the bursts. We required that the event appear across all the energy channels above its minimum energy simultaneously (except for the aforementioned time of flight delay which was used for analysis). This time of flight delay was a necessary condition to enable an analysis of source location. Other events which could not be analyzed through time of flight were excluded even if they exhibited other signatures which might be consistent with microburst precipitation (timescale).

### **Mapping Microburst Source Region**

From these two conditions a total of 828 events were identified over the course of the mission which could be mapped. The events were ordered by L and MLT, providing two dimensions of constraint on the source regions. Figure 20 shows the distribution of these events in L, MLT, from the spacecraft ephemeris, normalized by the total observing time from Freja. The primary location of these events was on the downside from approximately 0300-0900 MLT, with a tail of events extending towards, and just before midnight and from 4 to 8 in L. These results are not unexpected, as they agree with earlier work on relativistic microbursts (O'Brien et al., 2003) in observing a concentration of events on the downside, with L values of roughly 4 to 6. These results were also shown in Chapter 2. By and large the trend in results is similar to the SAMPEX

data, although there are some differences which may be a function of opportunity and statistics. For instance, SAMPEX was better able to resolve a peak local time for event frequency in the pre-noon sector where there are comparatively fewer observations. A comparison with spatial measurements of chorus strength from THEMIS (Li et al., 2009) showcases a similar distribution in intensity. Moreover, the L shells of measured microburst precipitation match radiation belt sources despite the lower particle energy.

Events per hour of Observing time

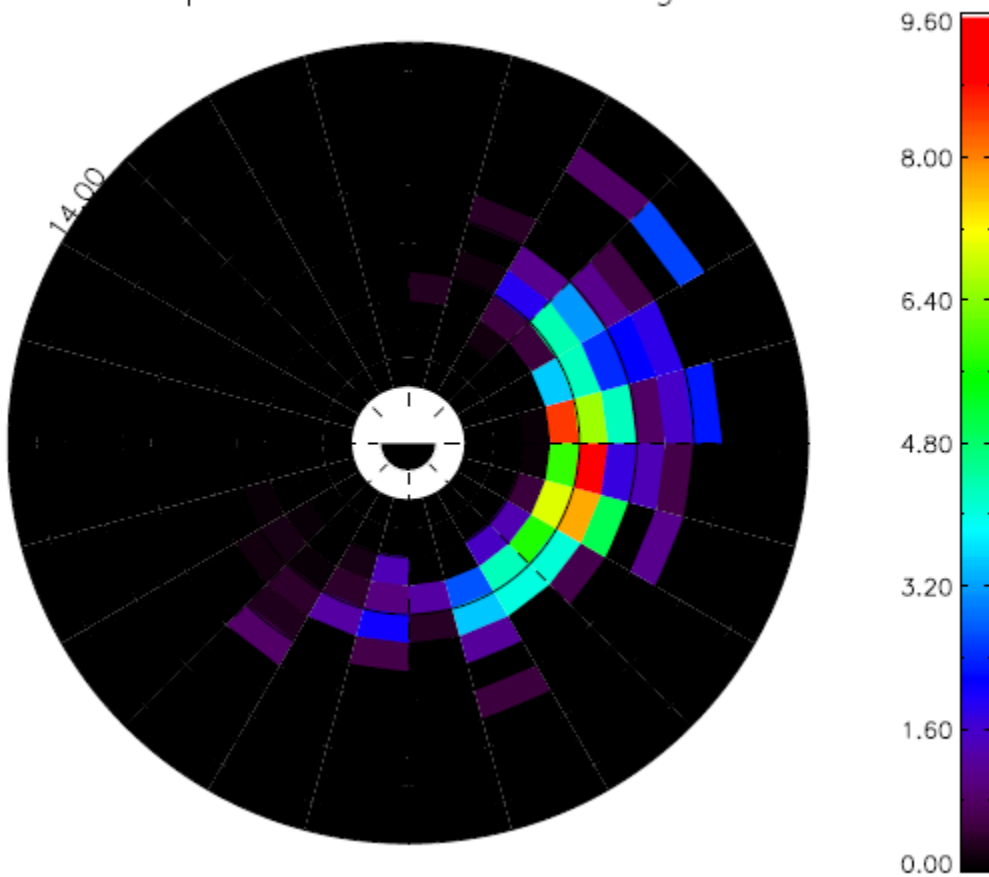


**Figure 20. Distribution of microburst events measured by Freja normalized by observation time within each MLT, L bin, extending out to a maximum L value of 10. This comprises all events which matched the necessary conditions to be identified as a microburst and mapped.**

Our measurement of the distance traveled from the microburst source regions permits us to systematically add in source latitude as a third dimension of constraint on the source regions. For this calculation we took the calculated distance from the source region obtained from the velocity-time dispersion (Figure 19) and then traced backwards along a dipole magnetic field that distance from Freja's location. Figure 21 depicts the average distance from the equator of the traced events in each bin with at least five events. For each event the calculated linear fit of distance from delay produces a calculated uncertainty in the measurement that is generally 10% of the total distance (ranging from 5% to 20% for a single event). Propagating the distance uncertainty into a latitude one depends on a host of factors, depending on the precise location of the satellite, as well as the distances and latitudes in question, but typical values are approximately 10°.

One question that might come up is the choice of a dipole field for the mapping as opposed to a more realistic field model (even something like a T-89 empirical model (Tsyganenko, 1989)). The choice of a dipole model comes primarily from its simplicity; as many modeling results present their work in a dipole field. it simplifies the comparison. Additionally, the areas of greatest discrepancy between a dipole field model and the actual magnetic field are typically at largest L values and closest to midnight during storms (Huang et al., 2008). Many of our events occur in the inner magnetosphere where the discrepancies are not as large. We did attempt a tracing of some of the results in the T-89 field and while the individual results shifted around within the

aforementioned  $10^\circ$  uncertainty, there did not seem to be a systematic change and we chose to stay with the simplest model.

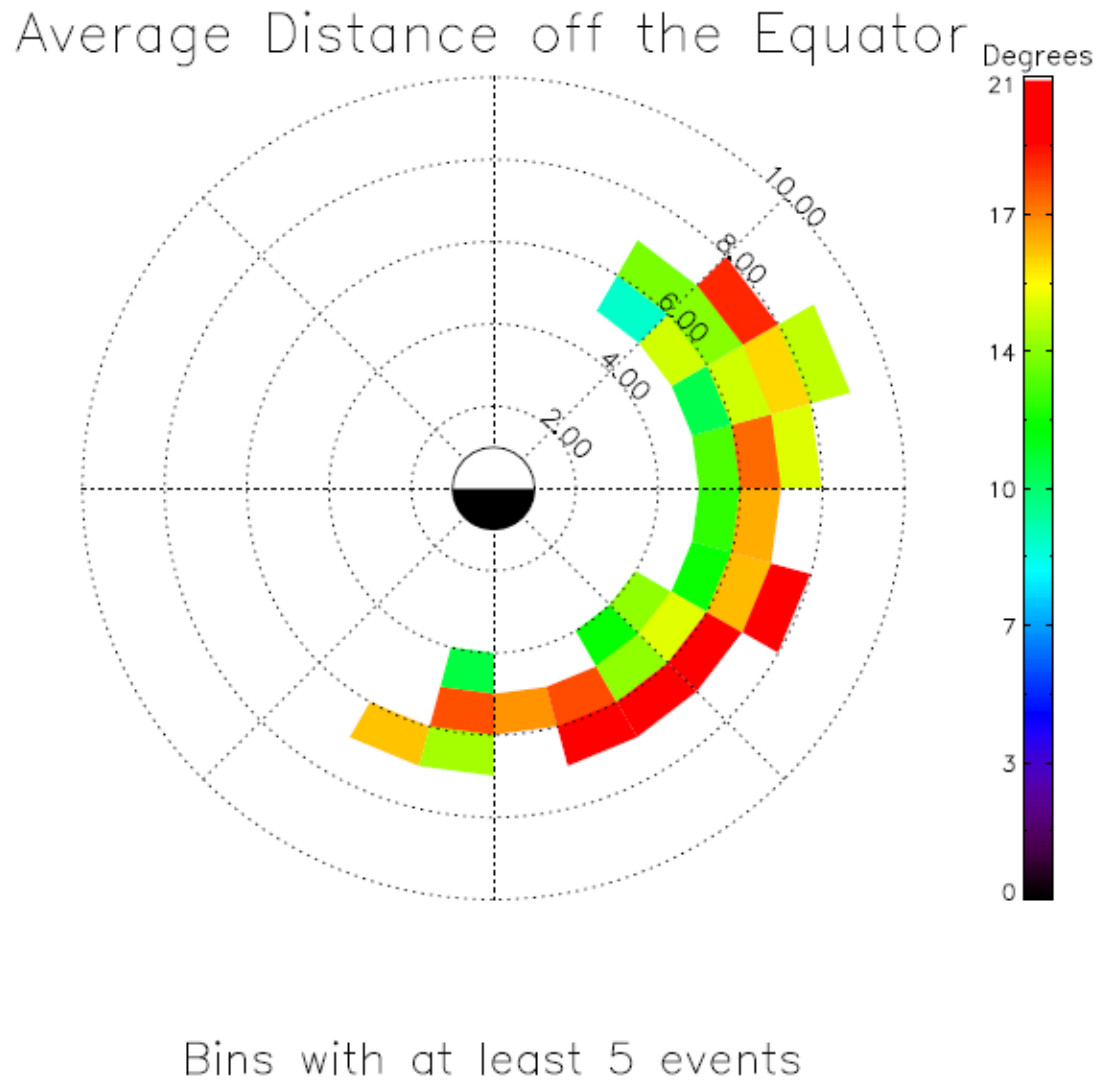


**Figure 21. Average distance off the equator for Freja events measured in degrees latitude, binned by MLT and L. Only bins with at least 5 events are shown.**

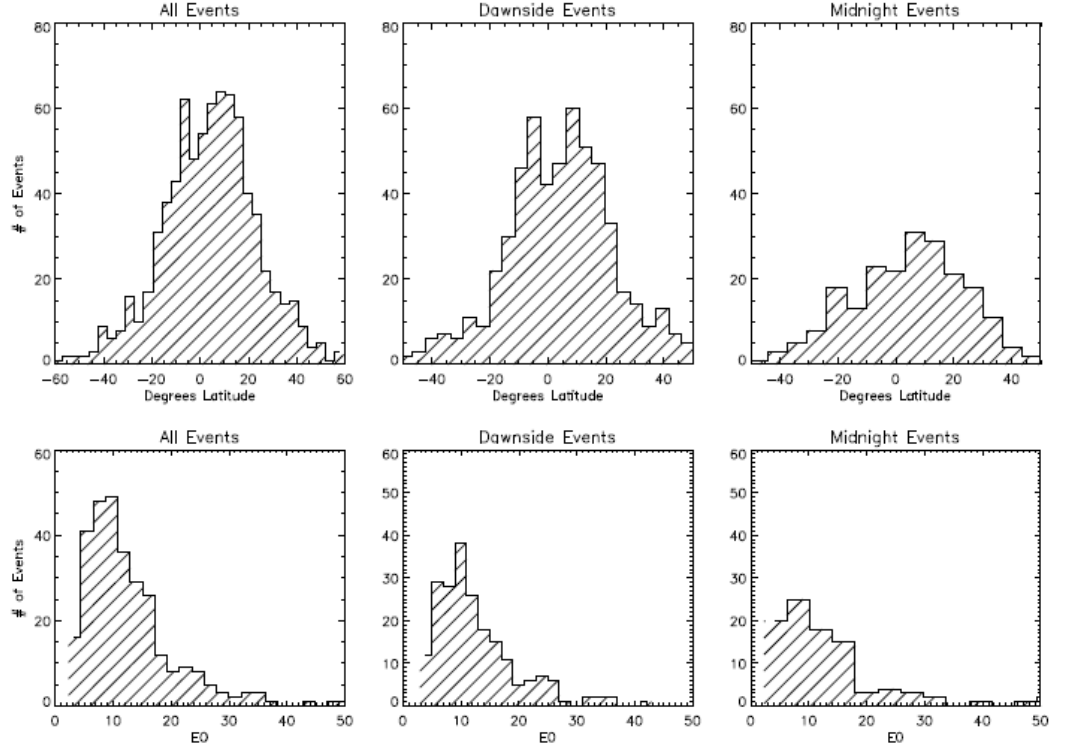


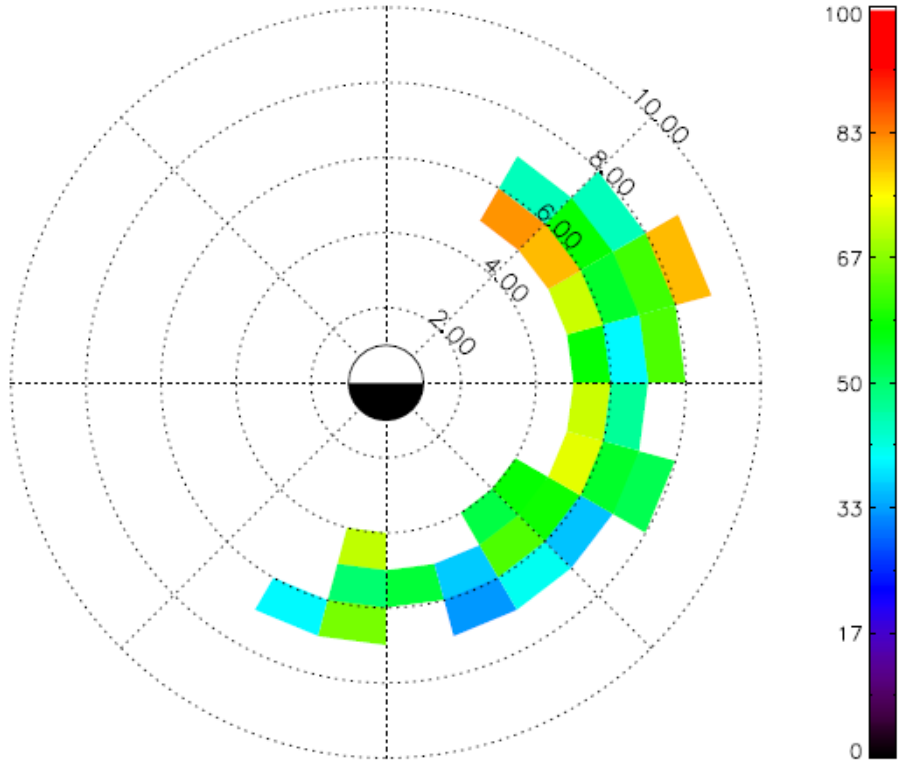
**Figure 22. Histograms of microburst source latitude and characteristic energy. Top panel shows source latitude (positive is Northern hemisphere, which is the same hemisphere as the spacecraft) for all events, only downside and only midnight events. Bottom panel shows the calculated characteristic energy for the spectra of events in the different categories.**

Within a given region there is still variation in the microburst source latitude. Figure 22 shows the distribution of microburst source latitudes for all events and divided into a ‘dawn’ sector (from 0300-0900 MLT) and a ‘midnight’ sector (from 2100-0300 MLT). From this we see that the overall distribution is one that peaks around the equator and falling off to higher latitudes. Although both populations peaks around the equator the downside events fall away very quickly as latitude increases, while the decrease is much more gradual for the midnight events and a much larger fraction comes from far off the equator. Moreover, we expect that as the field lines get stretched (which is more likely near midnight) the difference from the dipole model becomes more significant,

and a field line tracing of a dipole field will result in binning the event closer to the equator than its actual source. Additionally, given the size of the uncertainties on the mapping process, the twin horns seen in the downside distribution around +/- 10° may not be significant. However, the key result is that microburst events are most commonly seen as originating from near the equator.

Given that the typical uncertainty is ~10°, we use this to organize events into the twin categories of equatorial and non-equatorial. Using a definition of an equatorial event as one with a source latitude less than 15° off the equator, events with a source latitude of >15° must have a non-equatorial source. As modeling results, (Hikishima, Omura and Summers, 2010) can create microbursts through an equatorial interaction this separates out events for which a different mechanism or interaction region is needed. Furthermore, it facilitates comparison with equatorial and non-equatorial chorus wave measurements. Accordingly, Figure 23 depicts the fraction of events within 15° of the equator. For downside events, most events can be comfortably described as equatorial with only a small fraction that come from far enough off the equator to require type of source region. For the events that occur near midnight, the fraction of events that fall into an equatorial definition is lower. There are still many events that can be considered as such, but there exists a substantial non-equatorial population as well.

## Fraction Within 15 degrees of the Equator



Bins with at least 5 events

**Figure 23.** Fraction of events that correspond to mapped location within 15 degrees of the equator binned by  $L$  and  $MLT$ . Events that mapped to within 15 degrees of the equator are those which can be considered to have a possibly equatorial source.

A second characteristic of the bursts that was measured was the energy spectrum of the particle population of each event. For each event, the total counts observed was fit to a spectrum of the form  $\text{Flux} = Ae^{-E/E_0}$  where  $A$  is a constant,  $E$  is the channel energy, and  $E_0$  the characteristic energy of the distribution. This represents an exponential distribution with a characteristic e-folding energy  $E_0$ . Figure 24 shows the energy spectrum of a single event. Owing to the low measured fluxes during some of the events, not all events could be fit to this form of a spectrum. Nonetheless, for 303 (37%) of the events we were

able to obtain a measurement for the characteristic energy of the event spectrum, resulting in an average characteristic energy of  $13 \pm 8$  keV. For these events the average characteristic energy was calculated for the various local times and L values where we observed microbursts, the results of which are provided in Figure 25 for bins with at least five events. Furthermore, Figure 22 presents in histogram form the characteristic energy breakdown for midnight and downside populations. The downside and midnight populations see similar energy spectra; however events with a softer (smaller folding energy) spectrum are somewhat more prevalent within the midnight subset. These spectral measurements appear to be typical of microburst precipitation (Reinard et al., 1997), although the larger variability near midnight suggests the possibility of multiple source populations.

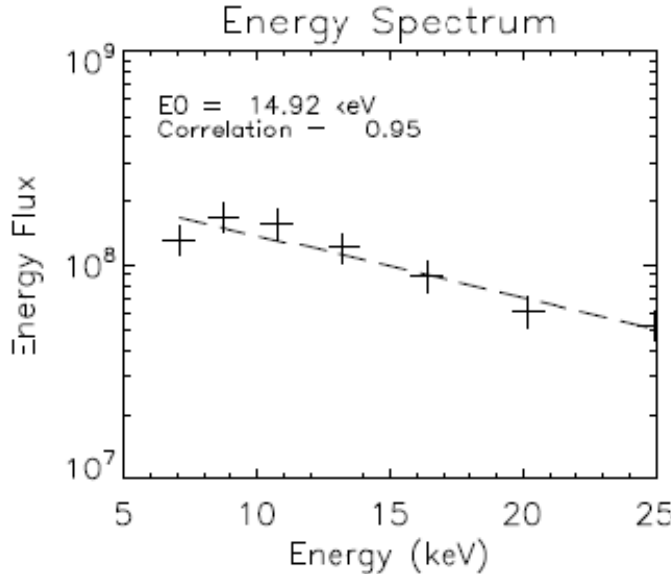
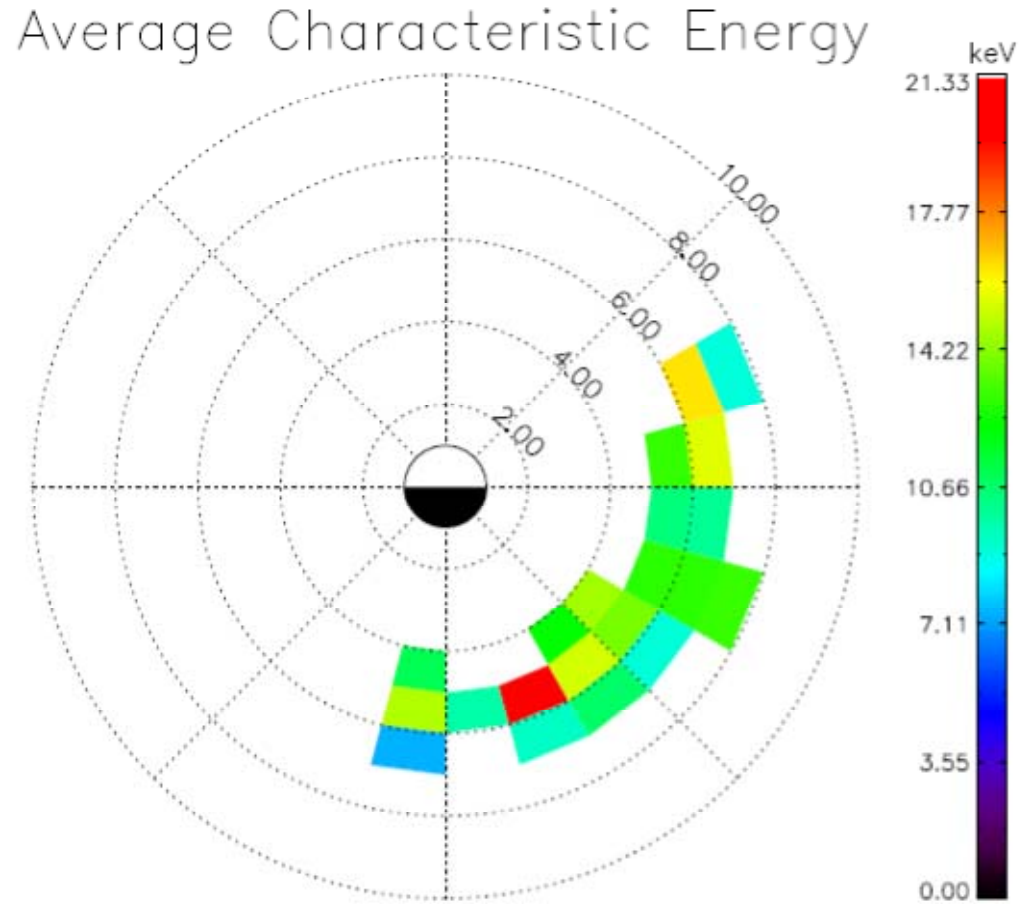


**Figure 24. Energy spectrum of a single microburst event. The energy spectra was fitted to an exponential distribution with a characteristic energy  $E_0$ .**



Bins with at least 5 events

**Figure 25. Average characteristic energy for events in different regions by MLT, L. Only those regions with at least 5 events are shown.**

### Discussion

The events from Freja represent an extension of the microburst energy range to a minimum of 5 keV, a lower energy than previously reported. Comparisons with work from SAMPEX (O'Brien et al., 2003) showcased a similar distribution in local time and L for the events, suggesting that in this realm these

lower energy microbursts mirror their relativistic counterparts. Analysis of the energy spectra of the events provides an additional method to connect these Freja observations with earlier observations of microbursts. The early work on microbursts provided measurements of a characteristic energy for microburst events assuming an e-folding spectrum. The initial measurements of microbursts by *Anderson et al.* [1966] showed characteristic e-folding spectrum of  $\sim$ 20keV, however balloons are limited at the lowest energies. Later work from the rocket flights (Reinard et al., 1997) measured the energy spectrum in the range of 20-120keV, or just above Freja's measurement range. Their measured values for  $E_0$ , the characteristic energy, for the exponential were generally of the order of 6-30keV in their lowest measured energy band, but there was substantial variation even among events within a single evening and within different energy ranges that they measured. Our measurements for the average characteristic energy of the downside events ( $\sim$ 15 keV) agree with earlier work on the microbursts. The bulk of the measurements are similar, although events occurring more towards midnight exhibit more dispersion in their characteristic energy (as shown in Figure 22 and Figure 25). The consequence of the similarities between the events observed by Freja and prior observations enables us to place the events within the larger context of microburst results. Specifically, the events measured by Freja represent a lower bound on the observed microburst energy; the processes responsible for microbursts must work at both the lower energies of Freja and higher (MeV) energies of SAMPEX.

A picture where chorus waves are intimately involved in the generation of microbursts requires overlapping measurements of the particles and the waves. Observations of the waves can come from a number of sources. For instance, measurements at lower L values come from the Cluster spacecraft (Breneman et al., 2009), (Santolik et al., 2003). Using the delays between the measurements at the different spacecraft to isolate the source of the chorus emissions, they concluded that the upper band emissions were confined to the region near the magnetic equator and that the lower band emissions dropped off with occurrence frequency at higher latitudes (Santolik et al., 2003). *Breneman* [2009] measured 52 different chorus events with a ray tracing technique and found that events were situated close to the equator, extending to a maximum latitude of 12°. From the THEMIS mission (Li et al., 2009) they categorized equatorial chorus as chorus from within 10° of the equator, which was primarily seen on the dawnside. On the dayside, some chorus was seen at higher latitudes, but not near midnight. Additionally, the THEMIS mission observed several periods of large-amplitude whistler waves in the outer radiation belts (Cully, Bonnell and Ergun, 2008). Their observations of large-amplitude whistlers showed a high-amplitude peak on the morning side around L shells of 3.5-5.5. These are co-located with much of our microburst observations, although we do not have wave observations at higher L shells, and they do not explain the midnight bursts. Furthermore, *Meredith* [2003] used data from CRRES to show that the required chorus conditions for the scattering and acceleration occurred during active conditions from 2100 to 1300 MLT, with the most favored regions being between L of 4 and 6 from 0300 to

1000 MLT. Moreover, within these regions, the chorus activity was constrained to within 15° of the equator.

The interaction of 10-100 keV electrons with individual chorus elements has been modeled by *Hikishima et al.*, [2010]. Their model was able to demonstrate a one-to-one correspondence between wave packets and particle microburst events. This model had the interaction between the chorus and the particles taking place on the equator, with the particles then propagating away. The energy range for the simulation was for 10-100keV, while our particle measurements were from 5-20keV, but the similarity is apparent. Another point of interest from that paper is that their model produced an energy-dependent dispersion in the generation of the microbursts owing to the different group velocities of the resonant waves. However, the associated delay appears to be less than that measured by Freja, so we will continue to assume that the dispersion is primarily due to time of flight effects. Accordingly, any events which map to an equatorial source region could be explained by this process, while it would not explain events that map to higher latitudes.

The measurements of chorus activity help inform the organization of the source latitude data. Owing to the limitations of the precision of the measurement, those events from within 15° of the equator were characterized as equatorial in nature, while those from further off the equator were considered non-equatorial. A result of this definition is that events mapped to a latitude less 15° constitute the events that can be explained by equatorial chorus. For the population of events that map from further off the equator, we therefore believe

that they must be the result of a process that is not occurring on the equator. On the downside most events can be considered to be equatorial in nature, with a handful of events that do not fit that description. For this majority of the events, a picture where the microburst events are caused by interactions with chorus waves near the equator is a satisfactory explanation. In this picture, the strongest regions of wave activity are correlated with the strongest source regions of microbursts.

However, towards midnight, the trend in source latitude reverses and the number of events which are clearly non-equatorial in nature increases. There still are a large number of equatorial events, but we need an explanation for the non-equatorial population. There are a few possible explanations for why a significant fraction map to higher latitudes. The first is that while a dipole field model can serve as a reasonable proxy on the downside, near midnight—and especially during disturbed conditions—the difference between the dipole model and reality is sufficiently large as to incorrectly locate a larger number of events. For instance, *McPherron and Barfield* [1980] noted that in the tail it was possible for a satellite that is nominally at  $10^{\circ}$  latitude to be effectively on the equator during some conditions. This would suggest that near midnight the definition of what must be an equatorial event may need to be broadened. Widening this definition of equatorial could make the fraction of equatorial events near midnight seem similar to the distribution on the downside, but lacking as large a peak seen occurring directly on the equator. However, since this difference is not seen as much in the wave measurements (Meredith et al., 2003), it suggests that the

difference is more likely a mapping issue, rather than a new generation mechanism.

### **Conclusions**

The purpose of this chapter is to trace the path of microbursts back from the point of observation to their source region, and in so doing, address the question, “*What is the generation mechanism of microbursts?*” Measurements of low energy electrons from Freja provide constraints on microburst location, both the MLT, L (which has also been done at higher energies with SAMPEX) as well as adding a third dimension of constraint: source latitude. Over the course of the two year Freja mission, we observed 828 microburst events over a range of conditions that we used to provide two new characteristics of microbursts and to understand the generation mechanism.

The first is that the microbursts observed by Freja extended down to an energy of ~5 keV, yet still displayed many of the same characteristics (location, energy spectra) of other observations of the phenomena at higher energies. Measurements of the characteristic energy, done for completeness, were found to be consistent with prior work using other data sources. We note that exploring the similarities and differences in microburst characteristics ideally would be done simultaneously on the same spacecraft across a wide range of energies. That to date has not been done but is a goal of the upcoming NSF FIREBIRD CubeSat mission (Spence et al., 2012), discussed in greater detail in the next chapter.

The second result reveals that microbursts observed by Freja typically mapped to an equatorial (typically less than 15° off the equator) source location on the downside, while being distributed in L from roughly 4 to 8. An equatorial source for microbursts correlates with complementary measurements of lower-band chorus known to preferentially occur in this same region, which strongly implicates it as the generation mechanism responsible for microbursts. These two study results (the extension of the microburst energy to lower energies and the inferred equatorial downside source region) constrain microburst theories by requiring an appropriate energy range of interaction, as well as a region for the interaction to take place, both supporting chorus generation.

These results inform our understanding of microburst generation by attacking the search for resonant regions, which in turn gives clues about the involved processes. Understanding the processes responsible for microburst precipitation enables a better understanding of when and where microburst precipitation is likely to occur. If the overall goal is to understand global microburst precipitation as one of the loss mechanisms that contributes to the overall radiation belt dynamics, it is useful to understand limitations on their creation which comes from understanding the generation mechanism.

# **CHAPTER 4**

## **HARDWARE DEVELOPMENT**

### **Motivation**

This chapter is intended to address the following thesis focus question: “*What is required to create the next set of microburst observations to make substantial progress in understanding?*” In that vein, the objective is to take the experience and knowledge gleaned from past observations of microbursts (e.g. SAMPEX, Freja, sounding rockets, balloons, as detailed in earlier chapters) and construct a targeted science mission that addresses new science questions for microbursts with appropriate instrument and mission requirements. More specifically, this chapter focuses on the upcoming NSF FIREBIRD CubeSat mission. As the mission is slated for launch in December 2013, the emphasis is on the instrument design and calibration, as opposed to the post-launch data analysis, which will be separate work from the thesis.

### **FIREBIRD Overview**

FIREBIRD (Focused Investigations of Relativistic Electron Bursts—Intensity, Range, Dynamics) is an NSF funded CubeSat mission that is specifically designed to study microbursts (Spence et al., 2012). Organizationally, the FIREBIRD mission is a collaboration between the University of New Hampshire and Montana State University, with The Aerospace Corporation and

Los Alamos National Laboratory as unfunded collaborators. FIREBIRD consists of a pair of 1.5U (10 x 10 x 15 cm) CubeSats, which will slowly separate and make measurements of microbursts at a variety of spatial scale lengths and separations. At its very heart, FIREBIRD is focused on multipoint measurement of specific phenomena (microbursts) as a way of leveraging the strengths of CubeSats and minimizing weaknesses. Each FIREBIRD CubeSat is identically instrumented. Individually they are designed to provide high resolution single point measurements; together they are used to address scientific questions that require multipoint analysis.

Each FIREBIRD CubeSat is itself divided into two components—the instrument and spacecraft bus itself. The University of New Hampshire is responsible for the instrument, called FIRE (FIREBIRD Instrument for Relativistic Electrons), with assistance and expertise from The Aerospace Corporation and Los Alamos National Laboratory. FIRE's design and operations were specifically planned to take into account knowledge gained on previous missions (and some from past chapters of the thesis) to address FIREBIRD science questions. The spacecraft, called BIRD (Bus In support of Radiation Detection), is built by Montana State University who, in turn, will operate the spacecraft. As CubeSats are by necessity highly resource limited, the mission is specifically targeted to the needs of microburst science. The breakdown of FIREBIRD into its components and the relative simplicity of the interface is highlighted in Figure 26. This picture is from interface testing of the first combined FIRE/BIRD payload at MSU in December 2012. FIRE (the instrument) is visible held in the clamp at the right,

while BIRD is on the benchtop next to an empty spacecraft exterior. FIREBIRD's two solid state silicon detectors are within the aluminum housings on the top board (currently covered to protect against accidental damage). A single interface cable connects FIRE to BIRD. The simple interface between the two is important for a mission that involves large teams of students at multiple institutions working on a project with a minimal budget. That is not to say that such simplicity is the exclusive domain of CubeSats; rather it is a programmatic necessity for such a class of mission.

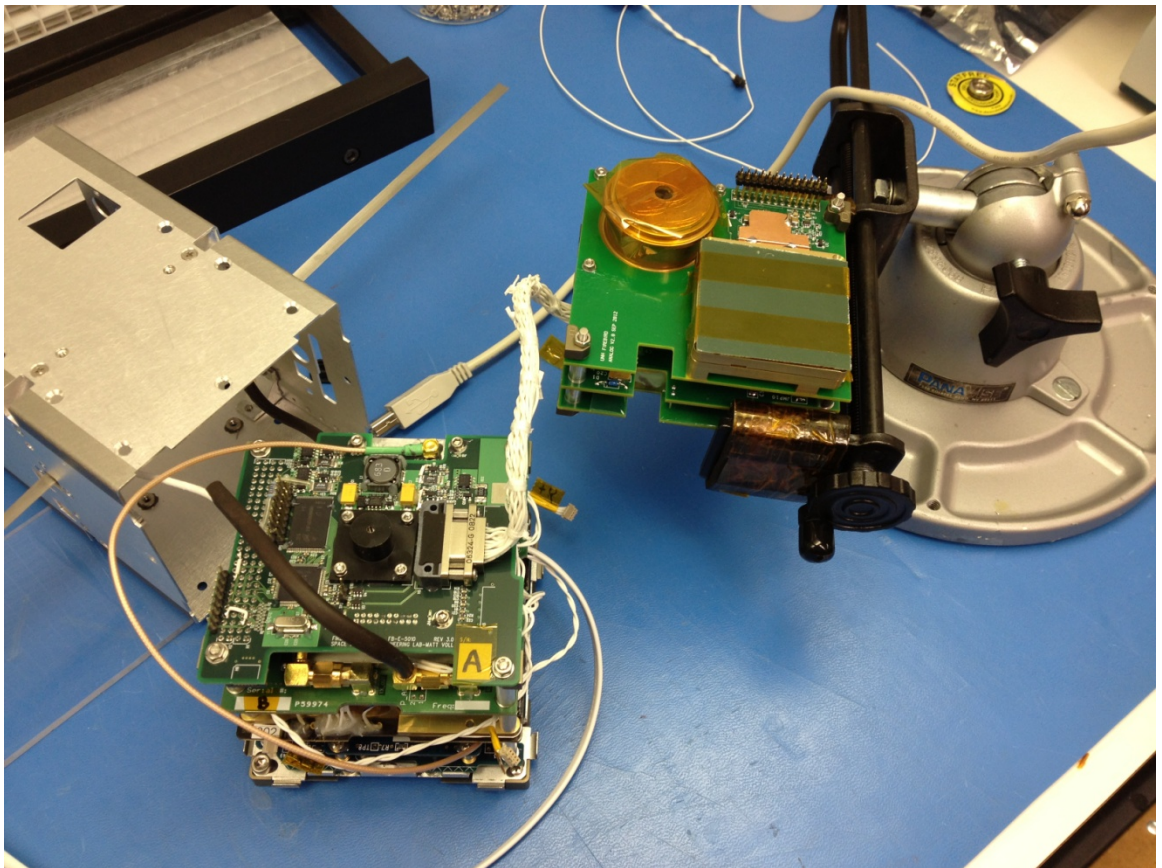


*Figure 26. FIRE/BIRD interface testing at MSU. MSU's BIRD bus is seen in the bottom left, while FIRE is held on the right by the clamp. A single interface cable connects FIRE to BIRD. BIRD occupies the bottom 10x10x10cm of the CubeSat structure, while FIRE uses the remaining 5x10x10cm space. The detectors are within the (covered) doghouses which protrude from the top (analog) electronics board. A model of the spacecraft exterior (with extended antenna) is visible in the top left.*

## **FIREBIRD Science Objectives**

The FIREBIRD mission is built around 3 science objectives. The first (and primary) one is to assess the spatial decorrelation scale length of microbursts. This is accomplished by measuring the occurrence of correlated and uncorrelated microbursts between two spacecraft with those measurements taken at a variety of separations. This science objective establishes the key requirement of having two identical FIREBIRD spacecraft, which are capable of identifying microbursts, as well as requiring a variety of separations between them (no easy feat for CubeSats). The second science objective is to measure the energy range and features of individual microbursts. This objective is accomplished by achieving high-resolution measurements of individual microburst events, and therefore defines the performance requirements of the FIRE instrument on each spacecraft. The third and final goal of the mission is to assess the global scale of microburst loss. This goal is of obvious interest to this thesis (it is discussed much further in Chapter 5) and is not something that FIREBIRD will address by itself, but rather will be done in conjunction with other missions—namely Van Allen Probes (formerly RBSP) and BARREL. Nonetheless, this final mission objective informs design considerations.

## **Spatial Decorrelation Scale Length of Microbursts**

As stated above, the primary goal of the FIREBIRD mission is to assess the spatial decorrelation scale length of microbursts. Doing so addresses some of the characteristic scale lengths of the regions of microburst activity. There are

two notable scale lengths that we are interested in. The first is the scale length that corresponds to the size of an individual burst—how far apart must two satellites be before they are no longer measuring the same microburst event? The second scale length of interest is the scale length involved in the size of the microburst region. This is for when FIREBIRD A and FIREBIRD B are seeing different microbursts simultaneously, and is an indication of the regions over which groups of events are occurring simultaneously.

The necessity of multipoint observation is further tied into the following challenge: with single point measurements it is impossible to tell the difference between temporal and spatial variation. For a satellite in low-earth orbit, typical speeds are  $\sim 7$  km/s, so in the span of a single microburst ( $\sim 100$  ms), the satellite will have traveled 700m. In order to tell the difference between spatial and temporal phenomena, multiple points of measurements are required. Some aspects of the spatial-temporal ambiguity present in microbursts can be handled with balloon measurements since they do not move as fast, but using multiple points of measurement eases analysis of satellite data. There is strong evidence for microbursts being a temporal phenomenon owing to similar durations observed by balloons, sounding rockets, and satellites which have very different velocities. Nonetheless, it is a question which gets at the heart of the mission. Similar issues exist for looking at global patterns in microburst precipitation—the maps built up by SAMPEX are unable to disassociate temporal and spatial variation also. The precise separation speed of FIREBIRD is presently unknown. From a design perspective, the smallest separations between the spacecraft are

of the greatest science impact, so minimizing the separation velocity of the two spacecraft was a mission goal. Extensive testing by MSU determined that the optimal way to minimize this was to use the spacecraft foot springs from the p-pod to control separation. Their testing revealed significant spread in the strength of the springs (which could not be controlled) but best estimates suggest a likely separation velocity of  $\sim$ 1-1.5 cm/s (which works out to approximately  $\sim$ 1 km/day).

As microbursts are understood to be associated with VLF chorus wave activity, further comparisons between the two are of special interest. Figure 27 shows how multiple spacecraft can be used to create a decorrelation scale length for chorus measurements. In the first panel individual chorus elements are shown from a single spacecraft; similar to microbursts the single-point data appears as a significant number of bursty measurements above the normal levels. The calculation of a ‘decorrelation scale length’ comes in panel b, where this measurement is repeated for each of the four Cluster spacecraft and correlated. By measuring the correlation likelihood for events as a function of spatial separation, estimates of the scale size of chorus regions are generated (Santolik, Gurnett and Pickett, 2004). This process can then be repeated for microbursts; panel c shows single point measurements of microbursts from SAMPEX. However, the multipoint decorrelation is something heretofore un-attempted and the focus of FIREBIRD. After the two FIREBIRD CubeSats are ejected from the p-pod after launch, they will slowly (and passively) separate from one another. Over the course of the 120 day prime mission, it is expected that they will reach a separation of  $\sim$ 150 km (the exact amounts depend precisely on the separation

speeds achieved as well as the angle between the separation velocity vector and the orbital velocity vector of the spacecraft). By correlating the microbursts from the two FIREBIRD spacecraft the decorrelation scale length can be calculated just like that of chorus and then compared with those results.

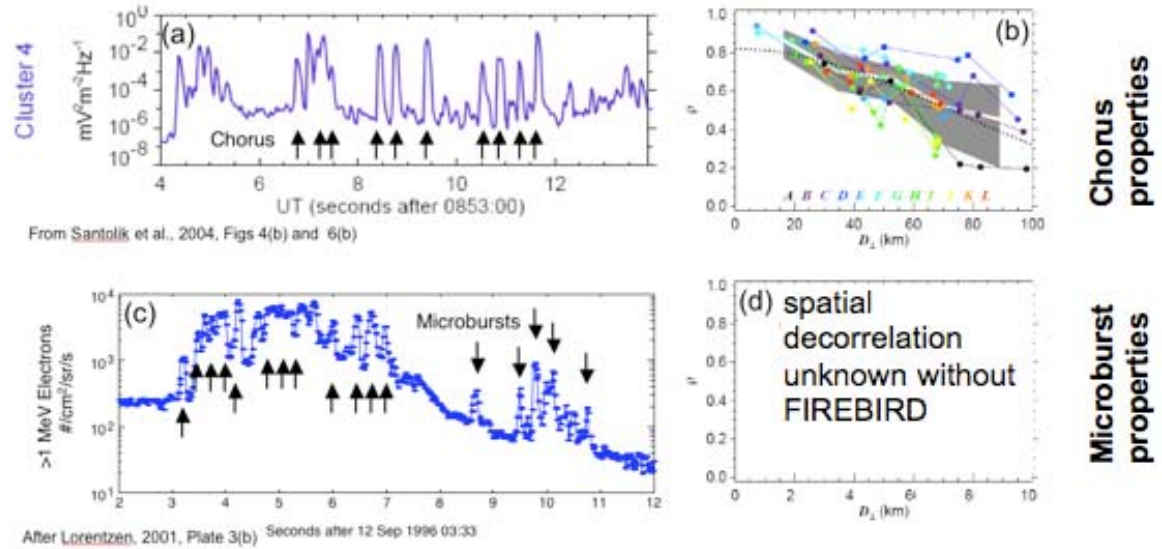


**Figure 27. Process for calculating the spatial decorrelation of chorus and microbursts. Chorus calculations are done using data from Cluster spacecraft, while microburst observations are from SAMPEX. Figure from FIREBIRD proposal (Spence, Private Communication).**

Calculating a spatial decorrelation scale length is a useful mission objective on several fronts. First of all, calculating the scale length lends itself to natural comparisons with the same quantity from chorus measurements. Currently, most of the evidence linking chorus to microbursts is what might best be described as strongly circumstantial. There are considerable links between the processes but they mostly take the form of comparisons that highlight the similarities of the processes, as opposed to direct causal links. Adding in an extra point of comparison will help extend this sort of comparison (or potentially provide constraints on generation mechanisms). Second, the measurements will

provide information about the size scale of an individual burst. This is useful both on a phenomenological level, as well as for better assessing event frequency and instrumental requirements. Although we can estimate how often microbursts are observed from spacecraft data, we do not have a great estimate of how many happen but are not observed due to the spacecraft not being in the right place to see a burst if it is very small. Finally, understanding the size scale of the region over which microbursts occur (as in when both spacecraft see microbursts but not the same microbursts) addresses one of the key issues and uncertainties that has been raised in estimating the total loss due to microbursts (O'Brien, Looper and Blake, 2004).

In order to complete this measurement it is therefore necessary to generate measurements of precisely when microburst events occur on the two spacecraft simultaneously, with accurate knowledge of the spacecraft separation. This requirement informs instrument design and operation, putting a premium on being able to determine if microbursts are occurring. Being able to identify a burst generates the requirements on instrument timing (must count fast enough) as well as geometry factor (sufficient counts for bursts to stand out). Additionally, this drives the requirement of having a GPS receiver on board each unit in order to measure the location and relative separation with sufficient precision and accuracy, a requirement for which the normal TLEs were deemed insufficient. (A TLE, or two line element, is a measurement of spacecraft position and velocity obtained from orbital analysis.) For a comparison with the scale length of chorus regions, it is important to note that spatial scales in low-earth orbit must be

mapped out to equatorial or near equatorial latitudes in the belts, which adds a significant expansion factor to the distances measured between the FIREBIRD spacecraft, which enhances desire for precision in measurements made in low-earth orbit.

### **Energy Range and Features of Individual Events**

The second goal of the mission is to measure the energy range and characteristics of individual microburst events. Unlike the first mission goal, which requires two independent CubeSats, this one is achievable with high-resolution measurements from a single point and consequently sets the performance requirements of the FIRE instrument. The impetus for the science question comes from measurements from two different instruments on SAMPEX. The HILT instrument, which was earlier used for large numbers of statistics on microburst characteristics (see Chapter 2), measured microbursts of electrons with energy  $>1$  MeV in a single channel. An additional instrument (PET) measured electrons in a 150 keV channel (Comess et al., 2013); however, event measurements between the two instruments were not always correlated (Blake et al., 1996). Sometimes microbursts occurred across the entire range simultaneously, but at other times, the two were uncorrelated. The implication is that there may be a break point in the microburst energy spectrum, and that there may be important differences in the generation mechanism of  $\sim 200$  keV level microbursts as compared with  $\sim 1$  MeV level bursts.

These questions of energy spectrum tie in very nicely to questions about the generation mechanism of microbursts. Recall how in the discussion of the

theory of microburst generation in chapter 3, the resonance regions are functions of many variables—in particular energy. Having a breakpoint in the energy spectrum would be evidence that the resonance conditions between the wave and particles were only filled for certain energies which could constrain the regions in which the wave-particle interactions are occurring. Freja observations looked to constrain latitude for a small energy range; SAMPEX constrains MLT, L for a single energy, and FIREBIRD looks to constrain (within MLT, L) as a function of energy.

Accordingly, FIREBIRD is intended to make measurements across that entire energy range in order to map the energy spectra. From a design perspective, this was encapsulated through a philosophy of “fewer events at greater detail.” Owing to telemetry limitations the amount of data that can be sent down is severely limited for FIREBIRD. Therefore, the intent is to generate the highest resolution measurements possible of a few events at the cost of continuous data coverage. For microbursts, high resolution means both high time resolution (fast enough to catch the shape of the event) and high energy resolution (enough channels to determine if and where a breakpoint occurs). In the specific case of FIREBIRD, this meant that the high-resolution data would be produced at an 18.75 ms cadence (customizable) with 6 energy channels between 200 keV and >1 MeV (logarithmically spaced) in two detectors. This mission philosophy is implemented by having the above high-resolution event data combined with a lower time resolution microburst proxy (the MicroBurst

Parameter data) that is used to identify intervals of interest and later download them.

### **Global Loss due to Microbursts**

The third science objective for FIREBIRD is to assess the global loss due to microbursts. As this is a topic which is central to the overall goal of this thesis (see Chapter 5), I will not spend as much time discussing its relevance, but rather focus on how FIREBIRD seeks to address it. From the perspective of FIREBIRD, this is not a goal which is expected to be solved solely with measurements from FIREBIRD; rather it is one which seeks to combine FIREBIRD measurements with other platforms (namely Van Allen Probes and BARREL) in order to create a larger constellation of measurements. The ideal situation uses high resolution measurements of targeted microbursts in low-earth orbit from FIREBIRD in conjunction with detailed measurements of the current state of the radiation belts and the microburst source region from Van Allen Probes, and pulls in measurements of the instantaneous spread in event locations (MLT and L) from BARREL. BARREL, the Balloon Array for Radiation belt Relativistic Electron Losses (Millan et al., 2013) is a balloon array that will conduct a pair of one-month campaigns in January 2013, and January 2014. Balloons have a long-standing association with microburst science, and one of the chief virtues of BARREL is the ability to sample microburst precipitation (through the x-ray bremsstrahlung produced upon atmospheric impact) occurring at a range of local times simultaneously. The ideal is to combine the variety of data sources into a coherent picture of the total microburst loss globally.

## **FIRE Instrument Design and Concept of Operations**

The FIRE instrument is specifically designed to study microbursts within the constraints of the CubeSat budget (space, power, mass, cost). Physically, the instrument occupies a ½ U (5 x 10 x 10 cm) section of each 1.5U FIREBIRD unit. FIRE is wholly contained on 3 circuit boards: the analog board which houses the twin solid state detectors as well as the necessary analog electronics; a digital board, which handles event counting and communication with BIRD; and an HV power board, which supplies power to all of FIRE. As FIREBIRD will be in low-earth orbit, precipitating electrons will travel down the magnetic field lines, so a zenith-pointing spacecraft sees these electrons. With the passive magnetic controls implemented on FIREBIRD, that means that one end of FIREBIRD will be pointing straight up at the precipitating electrons in each hemisphere, and consequently, half the time the FIREBIRD will see the precipitating electrons, and half the time it will be nadir-pointing. This fits with power budget constraints that limit FIRE to a 50% duty cycle, so when the instrument is downward facing, FIRE will be turned off to conserve spacecraft power, as those events are likely to be of lesser interest (although in an ideal world they would also be measured).

## **FIREBIRD Science Operations Plan**

The primary design challenge of FIREBIRD was to determine how to achieve the aforementioned science goals within the constraints imposed by the severe size and power limitations inherent in the CubeSat platform. In addition to instrument size and power, telemetry was another major constraint of the mission (which in turn is fundamentally driven by power limitations). The telemetry

restrictions proved to be the primary driver of the science operations plan and led to the design philosophy of capturing fewer events in higher detail. The conclusion was to produce three different data products that would target the results needed to bring closure to the science questions. The data products were:

- 1) Event Data: High resolution (time and energy) measurements of specific microbursts
- 2) MicroBurst Parameter Data (MBP): A data product designed for identifying microbursts in the larger data set
- 3) Context data: A slower data product designed to provide broad measurements used to contextualize FIREBIRD's environment and facilitate data analysis.

The event data would clearly be the best data product for doing scientific analysis; however owing to telemetry restrictions only a small fraction of it can be downloaded. Accordingly, the intention is that the MBP data will be downloaded every day and used to identify periods of interest with microbursts, and then on a later satellite pass the Event Data from those intervals would be downloaded.

The context data is intended to serve as a way to understand the local conditions and instrument behavior. The three goals of the context data are, first to address broad questions of spacecraft location (as in whether or not the spacecraft is within the belts), secondly to provide a persistent data set that covers the entire mission span, and finally to be available to understand any potential oddities or

changes in instrument performance over the course of the mission (which might be harder to determine from a derived parameter such as the MBP data).

The requirements for the event data have their genesis in the second science objective of the FIREBIRD mission—to determine the energy range and spectra of individual microburst events. Originally, an energy range of 200-700 keV was specified for the instrument, but the availability of thicker detectors meant that the energy range was extended to 200-1000 keV. Within this energy range six energy channels were selected as the compromise that would permit high enough energy resolution to see any potential breakpoints in the spectra, while not proving an onerous burden for data management. Additionally, with logarithmically spaced channels it was expected that a 30%  $\Delta E/E$  energy resolution requirement would lead to the appropriate size bins. The timing of FIREBIRD was governed by the experience with the SAMPEX mission. Figure 28 shows the histogram of microburst duration measured on SAMPEX with an overlay of the various timing cadences used on FIREBIRD. As typical microburst events have durations of ~100 ms, it is necessary to have high-resolution data at a higher cadence in order to probe the structure of individual events. As the highest resolution SAMPEX data was at a 20 ms cadence, FIREBIRD ultimately settled on trying to mimic that for the Event Data. The green identification timescale line represents the implementation of the 100 ms MBP data. Owing to engineering considerations the Event Data time step was implemented as multiples of 6.25 ms. Accordingly, the normal Event Data is at 18.75 ms time resolution (by design very close to the 20 ms SAMPEX used). While originally

6.25 ms was the fast limit of the instrument, this operational mode was discarded due to problems with writing the data to memory fast enough on the BIRD end, and so the practical Event Data limit is 12.5 ms time resolution. That said, the intended normal operations is 18.75 ms time resolution for six energy channels on two detectors per spacecraft.

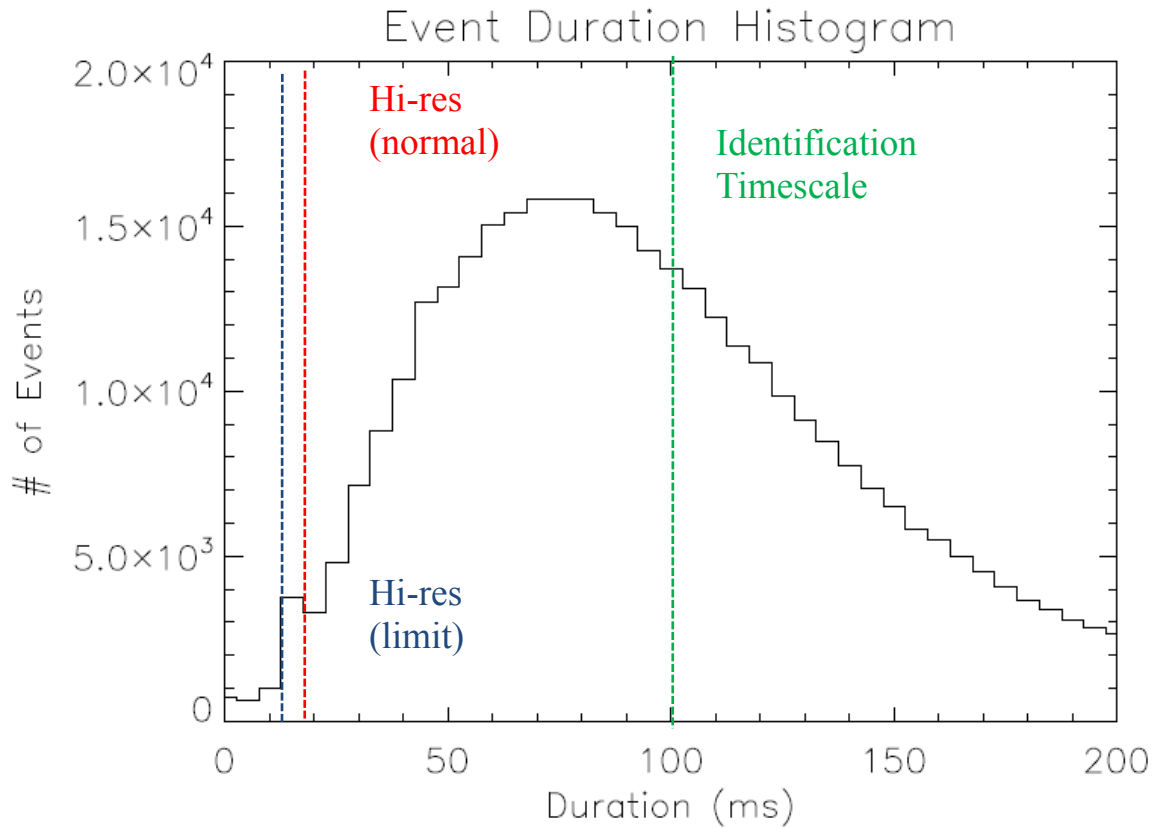


**Figure 28. Comparison of FIRE timing with microburst duration observations from SAMPEX. The green identification timescale is that of the MBP calculation (100 ms), while the normal hi-res data rate, and the practical limit are 18.75 and 12.5 ms respectively.**

In order to optimize the use of the high-resolution Event data, it is necessary to have a method for identifying periods of interest in the data so that not all of it has to be downlinked—an impossibility owing to telemetry constraints. The data product for achieving this is the MicroBurst Parameter (MBP) data. The MBP is a calculated proxy that is derived from O'Brien et al., [2003] and is the

same as was used in the Chapter 2 for the study of microburst characteristics.

The proxy is defined as:

$$MBP = \frac{n_{100} - a_{500}}{\sqrt{1 + a_{500}}}$$

where  $N_{100}$  is the number of counts in 100ms, and  $a_{500}$  is the 500ms rolling average of  $N_{100}$ . Microbursts are considered to occur when  $MBP > 10$ . The form of MBP was chosen so that it would be sensitive to large spikes at a variety of different flux levels. As implemented on FIREBIRD, FIRE actually measures  $N_{100}$  and  $a_{500}$  and passes these values to the BIRD computer which utilizes a lookup table to calculate the result and compresses it into four bits (values <0 to 45 in increments of 3) to save on transmission space.

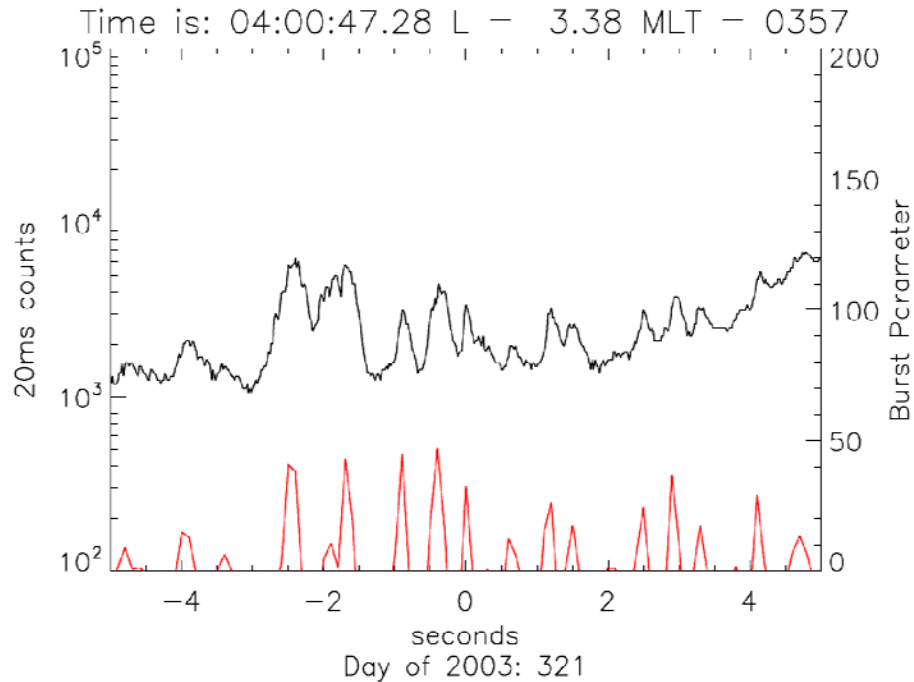


**Figure 29. MicroBurst Parameter Identification.** The top line is the 20 ms count rate from SAMPEX for a period with a number of microburst events, while at the bottom is the calculated MBP for the time interval. Spikes in the MBP correspond with microburst events seen by SAMPEX.

Figure 29 shows an example of how the MicroBurst Parameter identification will work on FIREBIRD. In the plot, the black trace is the 20 ms data from SAMPEX/HILT measuring >1 MeV electrons during a period of bursts. The red line underneath is the calculated MBP (matched to the vertical axis on the right). During microbursts, the MBP also spikes dramatically; while a value greater than 10 can indicate a microburst, during some events it reaches as high as 50. FIREBIRD's science operations plan relies on first producing the MBP data product (the red line) for all time periods and then using that to select the appropriate time intervals for download. While the exact file size is a choice that will be implemented on BIRD based on their constraints, preliminary analysis indicates that the default-sized high resolution data files will be ~3 seconds of data. From a science operations standpoint, it is expected that 10-second snapshots of the event data will be sufficient for most tasks (something borne out through the analysis of SAMPEX data conducted in Chapter 2). As a practical matter, when FIREBIRD is in the default state of 18.75 ms time resolution, each high resolution data file will be ~2.7 seconds long. Consequently, it is likely that four event files will be requested to stitch together a single microburst event.

### **Analog Electronics and Detectors**

Two solid-state detectors are used to make the measurements. Each one is a 1500  $\mu\text{m}$  silicon detector with a diameter of 32 mm. The chief difference between the two detectors resides in the presence of a short collimator around one detector. This has the result of reducing the geometric factor and angular acceptance of that detector. The two geometric factors are 23 and 9  $\text{cm}^2\text{sr}$

respectively. The goal of this is therefore to reduce the number of counts on one detector so that during times of intense fluxes the detector does not saturate. As previously noted, there is significant variability in the total fluxes from the outer radiation belt, and so having a very large dynamic range is necessary in order to capture the highest intensity events while still maintaining sufficient counts for analysis during quiet times. For 1500  $\mu$ m silicon detectors the maximum energy electron that will be completely absorbed is 1050 keV. Accordingly, this sets the upper energy limit of the detector, as more energetic particles will deposit less than their complete energy as they punch through, complicating the analysis. As the detectors are sensitive to light, each one is covered with an aluminum foil designed to both shield out light as well as low energy particles. By shielding out lower energy particles and preventing them from hitting the detector, it reduces the number of events that the analog electronics have to process, which helps avoid saturation issues.

The initial pulse processing is done via the use of a DAPPER (Dual Amplifier Pulse Peak Energy Rundown) chip that was provided by The Aerospace Corporation. Originally designed for the MMS/FEEPS instrument, a cousin of the DAPPER (the MAPPER) was an integral part of the MagEIS instrument on RBSP. The DAPPER is capable of handling both FIRE detectors simultaneously in a low noise, high data rate manner. Obviously, this is extremely beneficial for the program and is a crucial component to mission success. The DAPPER provides a fixed-height, variable width output pulse with a duration that is linearly proportional to the input voltage from the detector (this is different from

a more traditional pulse height analysis where the pulse width is fixed but the pulse height varies with energy). As the DAPPER's nominal maximum count rate is 100 kHz, it sets where the saturation threshold of the instrument is—which governs how thick of a foil shield is needed, and what acceptable geometric factors for the instrument are. Moreover, the relatively low noise of the DAPPER (~25 keV) helps set what the instrument threshold is. From discussions with Mark Widholm, the analog engineer on the project, the intended threshold value is ~5x the noise floor of the instrument. This threshold value is fixed with a particular resistor value on the board (so while it can be changed during building it cannot be adjusted in flight) to a particular analog value. The conversion from the analog threshold value to energy depends on the precise calibration of each unit but is ~125 keV. Having a higher threshold screens out lower energy particles (as well as noise), minimizing dead-time and reducing the likelihood of saturation, at the cost of eliminating the ability to push the energy channels lower if the instrument performance changes over time.

As the second science objective is to measure the energy spectra and characteristics of individual bursts, the detector choice and analog board setup is optimized for this task. For telemetry reasons, the data is limited to six distinct energy channels, but the detector thickness is optimized for the energy range of interest. 1500  $\mu\text{m}$  detectors mean that the maximum energy channel will be  $>1$  MeV electrons, which matches up well with prior measurements from SAMPEX. The minimum energy is set by noise limitations, which is a function of both detector thickness (thicker detectors are inherently noisier) as well as the analog

electronics. However, the detectors and electronics were chosen to be able to easily meet (and in fact exceed, as will be seen in calibration) the intended measurement range. The measurement range of FIRE was chosen so that measurements would bridge from the high-energy measurements of microbursts ( $>1$  MeV seen with SAMPEX/HILT) to some of the lower energy ones (in the 150 keV range).

There were a few major challenges encountered along the path to developing the analog board. The first challenge was that the DAPPER is an extremely ESD (electrostatic discharge) sensitive part. While reasonable precautions could be taken to lessen the chances of breaking them (and significant experience and expertise was available from The Aerospace Corporation), we nonetheless lost three DAPPERS to likely ESD failures over the course of testing. It is thought that many of the failures were due to small charge buildups on the detector housings which then were able to discharge into the DAPPER inputs, but we were unable to prove that rigorously.

The second major challenge encountered with the analog board was the construction and implementation of the aluminum doghouses for the detectors. These doghouses are mechanical structures which house the detectors in a light-tight environment and attach directly to the analog board. Figure 30 shows a detector inside one of the doghouses used on the engineering model. The inside of the doghouse has a few specific protrusions intended to lock the detector into place so that it could not rotate during flight (or vibrations) and keeping it separated from the metal to protect from HV arcing. A thin piece of aluminum foil

is then pinched between the delrin top piece (black) and the aluminum top of the doghouse in order to make it fully light tight. A few small paths were provided for out-gassing of the detectors, but they were cut to ensure that the detector would not be exposed to light. The example shown in Figure 30 is from the engineering model, which had one crucial difference from the flight ones. In the final flight builds, the doghouses were coated in order to prevent oxidation which unfortunately also made the doghouses electrically insulated from the rest of the board. This was problematic because the detector grounds were intended to be completed through the screws that went into the doghouse, but this connection was no longer sufficient. This problem manifested itself in ungrounded detectors, which in addition to being unable to provide useful data could potentially store sufficient charge as to be able to short out the DAPPER if it discharged at once. While this was not conclusively proven to be the case, it is expected that this grounding issue was responsible for one of the DAPPER failures found in March 2013. Figure 31 shows a fully assembled FIRE analog board from the flight builds. The two detectors are contained within the doghouses which are attached to the board. The small amount of electronics on the board is confined to one quarter of the board, with the most sensitive parts (DAPPER) underneath the copper shield. Communication to the digital board is through the connector pins at top left. A cutout in the bottom right was a structural requirement imposed by BIRD. Also of note, there is a green dust cover attached to the edge of the surface detector, as well as tape over the mouth of the collimated detector. This was designed to protect the foils during handling and tests which did not require

the detectors to measure electrons (i.e. gamma or pulser testing), and was removed before electron beam testing and flight.

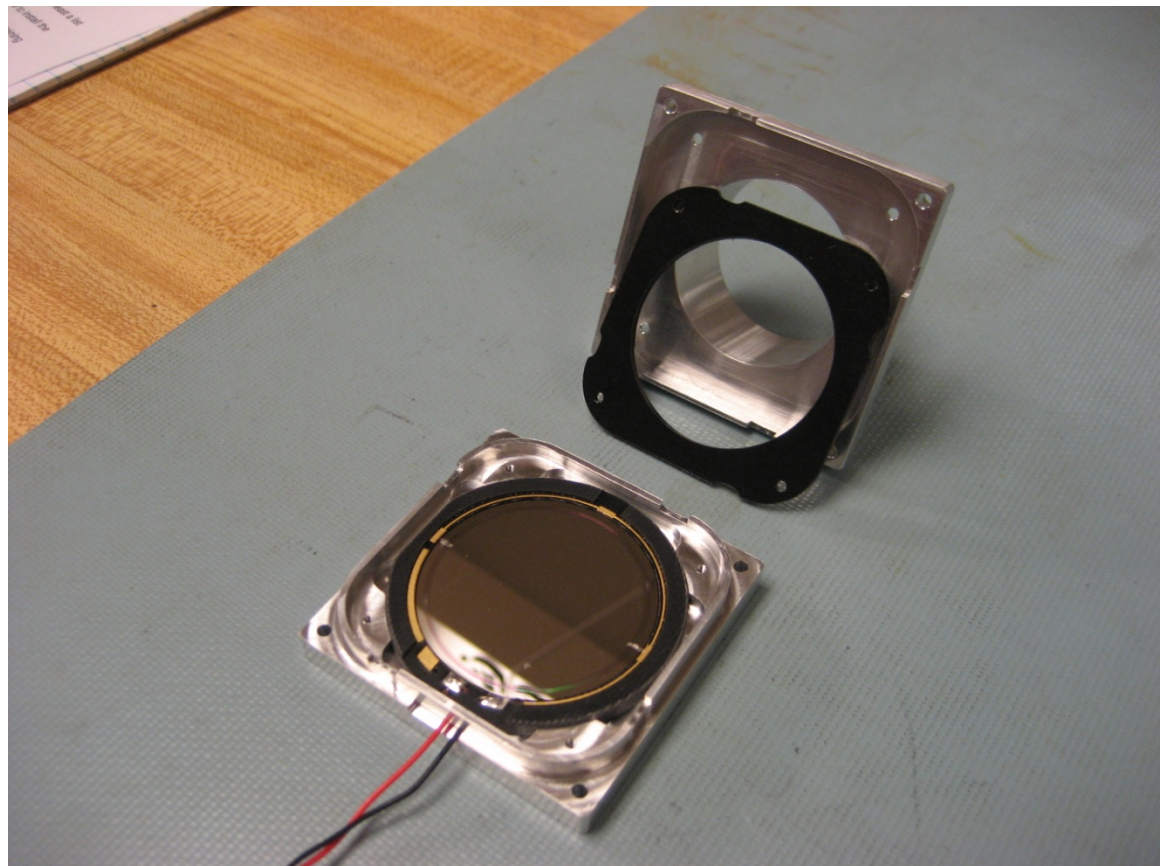


*Figure 30. A single FIRE detector inside a collimated doghouse. The doghouses were coated to prevent oxidation, hence the different color. The short collimator is visible as part of the top piece. The light-tight foil (not shown) goes between the delrin ring and the top half of the doghouse.*



*Figure 31. FIRE Flight analog board. Tape covers the opening to the collimated detector, while a removable dust cover (green) is attached to the surface detector to protect the foil. The sensitive electronics on the analog board (DAPPER) are underneath the copper shield.*

### Digital Board and Instrument Timing

The FIRE digital board controls instrument timing and communication between FIRE & BIRD. The analog board (specifically the DAPPER) outputs a variable-width, constant height pulse that is proportional to the incident particle energy to the digital board. This pulse length is then timed and then mapped into a digital bin, ranging from 0-255. The timing requirements for how fast the pulses are binned are determined by the DAPPER output, as well as expected flux levels in order to minimize dead time, while competing against the fact that a faster clock is more power-intensive—a challenge common to all spacecraft

missions, but of particular import for a CubeSat. Due to telemetry constraints, these 256 digital channels must be down-selected into one of six selected energy channels. This selection was motivated by the second scientific goal of the mission, which was to generate highly resolved energy measurements of a few particular microbursts, while working within limitations. The energy channels were chosen to be on-orbit customizable. This turned out to be a feature for laboratory calibration of the detectors where the channels could be rapidly changed to develop full histogram data at the native digital (256 channel) resolution as compared to the lower resolution products used in flight. This customizability of the energy channels was accomplished by passing the digital board seven values in each command packet which defined the digital boundaries of each channel.

The digital board is also responsible for producing the three data products produced by FIREBIRD. Those three products are the event data, which is produced at the highest data cadence—typically 18.75 ms, but settable to any multiple of 6.25 ms; the MicroBurst Parameter (MBP) data product, which is produced every 100 ms (fixed), and the context data which is produced every six seconds. In order to minimize the size and complexity of the ACTEL chip on the digital board (and therefore power requirements), the digital engineer (Steve Longworth) proposed that FIRE would pass BIRD the two numbers used to generate the MBP, but that the actual calculation would be accomplished with the onboard computer in BIRD. While the event data is recorded for all six energy channels on each detector, the MBP and Context data are only calculated off two

of the twelve total possible channels. As these channels are settable in flight, the digital board is responsible for appropriately maintaining the relevant counters and commanding of the instrument.

The digital board is also responsible for instrument commanding. As specified in the FIRE->BIRD Interface Control Document (ICD), FIRE's state is controlled by a 16 byte command packet. Of particular interest are a few of the customizable parameters. The instrument timing, and data rates are each settable through the command packet—(high resolution data is multiple of 6.25ms up to 100ms), and the telemetry cadence can be adjusted if needed. Of particular interest for calibration and flight activities is the way the six flight bins are computed. Thus, seven different numbers are used to define the six bins which correspond to digital values of the analog pulse width. Consequently, the bins are freely settable in flight.

A fully built FIRE digital board is shown in Figure 32. The top right quadrant is kept clear for the collimated doghouse which sits pressed between the analog and digital boards. The black connector in the bottom left is for the connection to the analog and digital boards. The ACTEL FPGA, which handles FIRE logic is mounted on the underside of the board (not visible). The center hole in the middle of the board was for the infamous screw which pulled the digital board and analog boards together structurally (infamous for its difficulty to work with).

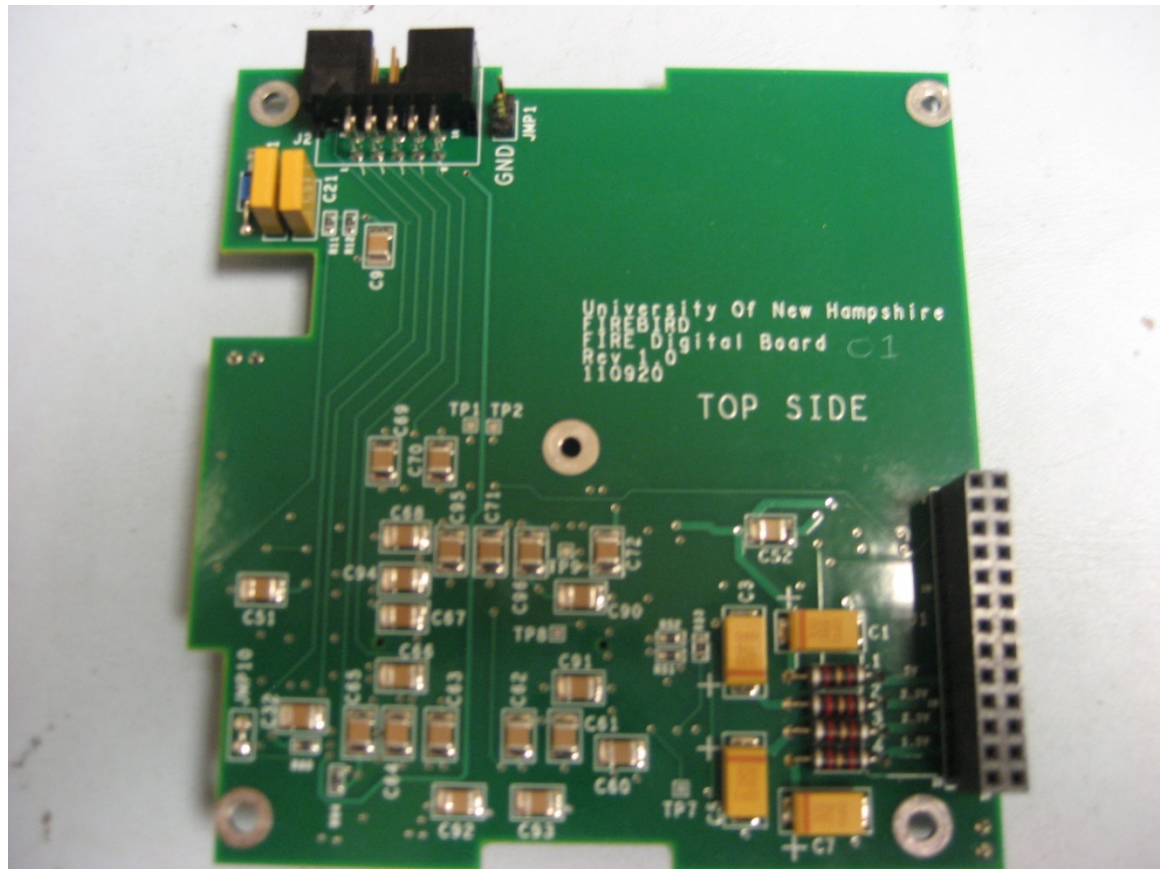


**Figure 32.** Top side view of FIRE digital board. The blank space in the top right corner is for the collimated doghouse which is pressed between the analog and digital boards. The connection to the analog board (above) and digital board (below) is through the black connector at bottom right.

## **Power Board and Unit Assembly**

The final major component of the FIRE instrument was the power board. FIRE's power board was responsible for taking the unregulated 8V line provided by BIRD and turning it into the necessary voltages to both operate the digital and analog electronics, as well as providing the 250 V HV supply for the detectors themselves. In actuality, the nominal 250 V HV power turned out to be 247 V owing to the precise construction of the board and the transformers used. The detectors used by FIREBIRD all had nominal operational voltages between 220 and 280 V, so 250 V was used as the designed standard, so a final value of

247V was perfectly acceptable. Also of note, the power board ended up being the only board which was conformal coated.

The full instrument assembly consisted of integrating the doghouses (with detectors) into the analog board, and then combining the analog, digital and power boards into a single stack. Between each board mechanical spacers were placed in order to ensure proper spacing of the boards for integration into satellite structure (provided by MSU). Additionally, above the analog and below the power board a set of mid-plane standoffs were attached which were used to affix FIRE into the structure itself. The fully built up FIRE is shown in Figure 33.

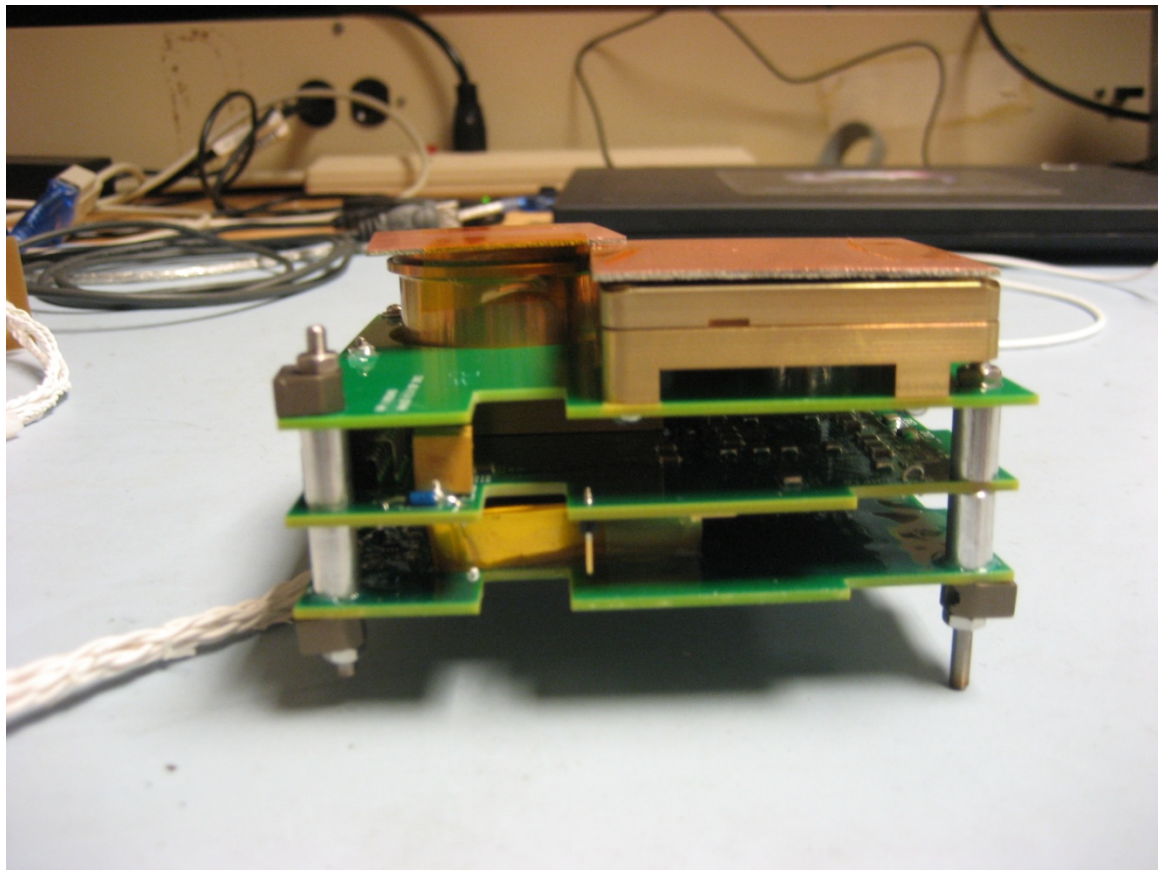


*Figure 33. Fully built FIRE unit. FIRE->BIRD interface cable extends from bottom left. Mechanical dust covers are placed over each detector aperture currently. Mid-plane standoffs for attaching FIRE to the spacecraft structure are visible above (on left) analog board, and below (on both sides) the power board.*

## **Instrument Calibration**

Testing and calibration of the FIRE instruments consisted of several different steps with different measurement objectives. The signal measurement path through FIRE for an incident electron is as follows. An incident electron starting with some unknown energy targets the detector. First, some small amount of energy is lost in passing through the aluminum foil cover on the detector. The exact amount is a function of particle energy (less at higher energies). Then the particle strikes the solid-state detector at which point it deposits energy in the detector. The exact amount deposited is dependent on particle energy, incident angle, and path length in the detector (as it can scatter out), but ideally it deposits all of its energy. The silicon detector then converts this energy deposit into a small charge pulse. This charge pulse is then measured by the analog board, and converted into a fixed-amplitude variable length pulse by the DAPPER. This pulse length is then timed by the digital board and converted into a digital value from 0-255. Finally, this digital value is compared to the six defined energy channels and the appropriate channel is incremented accordingly. Consequently, there are a number of different points along this path to check the calibration. As part of the testing and calibration plan, each FIRE unit underwent radionuclide source testing at UNH. Additionally, the FIRE A unit traveled to The Aerospace Corporation in January 2013 for further testing and characterization with their Beta spectrometer. Both flight units (FIRE A and FIRE B, later redubbed Flight 2 and Flight 1, respectively) traveled to The Aerospace Corporation again in May 2013, for final testing and calibration activities. Finally,

a Geant4 model of FIRE was built by Brian Larsen at Los Alamos National Laboratory to be validated against lab calibration and provide detailed instrument response functions.

### **Radionuclide Source Testing at UNH**

The initial testing and calibration for each unit took place at UNH through the use of radionuclide sources in the lab. This testing was done in air with a variety of beta and gamma ray sources that were locally available. While ideally the testing would be done in vacuum, this was not feasible for FIRE. Each unit was commanded through the use of the GSE (Ground Support Equipment) provided by MSU which replicated the actions of BIRD, providing commanding and data readout. Although FIRE only outputs counts into one of six energy channels in its highest resolution data product, calibration exploited the feature that the energy channel boundaries are adjustable in flight. Consequently, it is possible to sweep out every single digital channel (0-255) by varying recorded energy channels during the test. Any resolution up to a single digital channel (~10 keV) is achievable in this manner at the cost of testing time. If six channels are to be tested at a time, it takes 40x as long to measure the results in single channel bins. Accordingly, depending on the strength of the source and the requirements of the testing being done, the test resolution varied.

Three different sources were used in the lab testing of the instruments. The source was held in place 3" above the detectors so that it could illuminate both detectors simultaneously as well as to minimize the path length in air of the electrons (a concern of non-vacuum testing). Figure 34 shows the testing setup

at UNH. This shows testing with one of the gamma sources, which meant that the detector dust covers could stay on (the beta source was clamped so that the active area was above the exposed target detector). From the left side of the instrument extends the FIRE->BIRD interface cable (which was the sole electrical interface between the two sides of FIREBIRD) to the GSE board, which is run by the laptop.

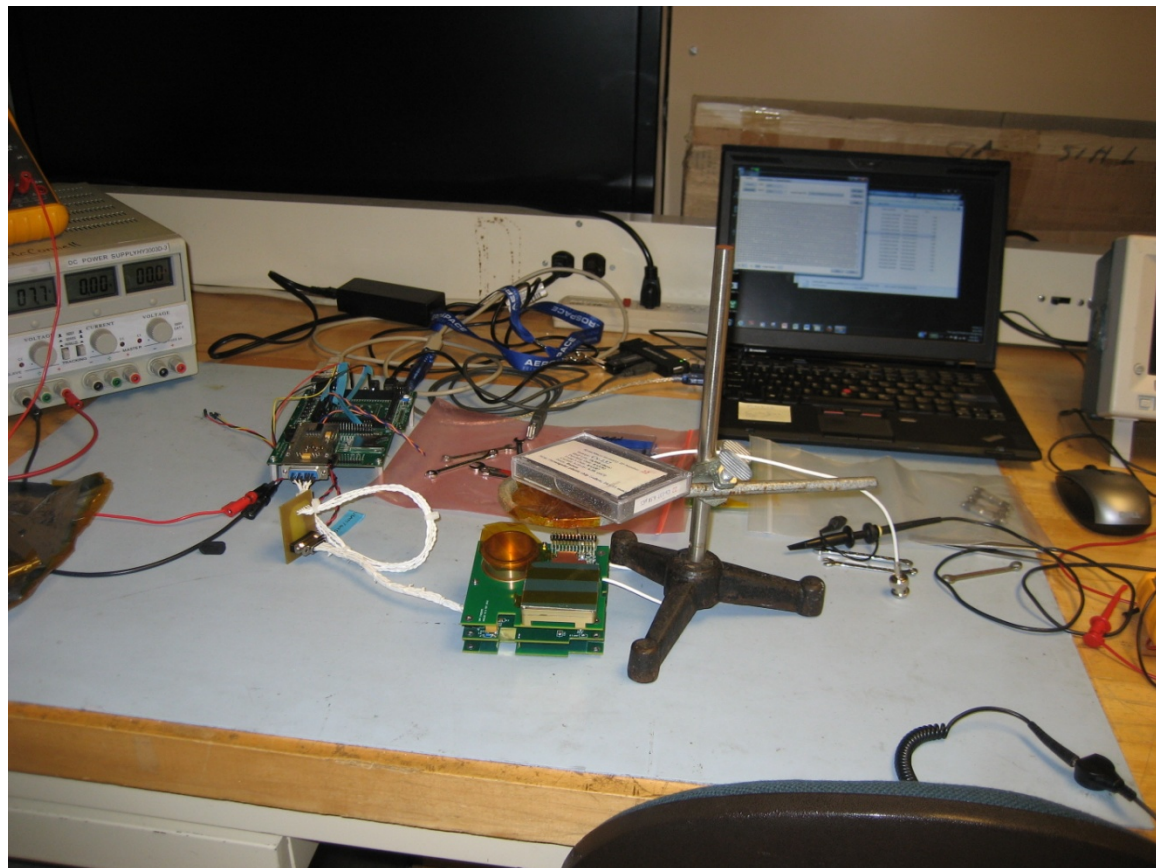


*Figure 34. Testing setup at UNH. The gamma source was held approximately 3" above the detector. The GSE board is visible to the left of the instrument, along with the laptop to command FIRE.*

The sources utilized in testing are summarized in the table below:

Isotope	Activity	Type	Notable Spectral Features
Ba-133	28.94nCi	$\gamma$	Peak at 356keV, Compton Edge near 207keV
Cs-137	95.74nCi	$\beta$	Conversion Electrons at 624keV
Cs-137	5.82 $\mu$ Ci	$\gamma$	Peak at 662keV, Compton Edge near 478keV

**Table 1. Sources used in radionuclide testing at UNH with relevant characteristics.**

Gamma ray sources have the advantage of not losing energy in the foil or in the air on the way to the detector for short distances, but typically have a low efficiency in the silicon detector requiring substantial run time in order to generate sufficient counts. Moreover, the characteristic shape of a gamma ray source has a Compton edge at known energy ( $2E^2/(m_e c^2 + 2E)$ ) where E is the energy of the photon. However, from a calibration perspective, although this is a recognizable feature in the spectrum, it is difficult to ascribe the edge to a specific channel number (unlike a peak which is easier to fit), making it qualitatively useful, but quantitatively less useful. Consequently the gamma sources were an ideal way for verifying that the instrument *worked* (if a pulser test was insufficient) and as a way of generating preliminary gains and offsets (which were refined in calibration).

Calibration results from source testing with the FIRE A unit are shown in Figure 35. The collimated detector is shown in the solid line and the surface detector is shown with the dashed line. The different colors represent the different sources: the green is the Ba-133 gamma source, the red is the Cs-137 gamma source, and the black is the Cs-137 beta source. The dotted vertical lines represent a few ‘interesting’ energies for comparison with calibration.

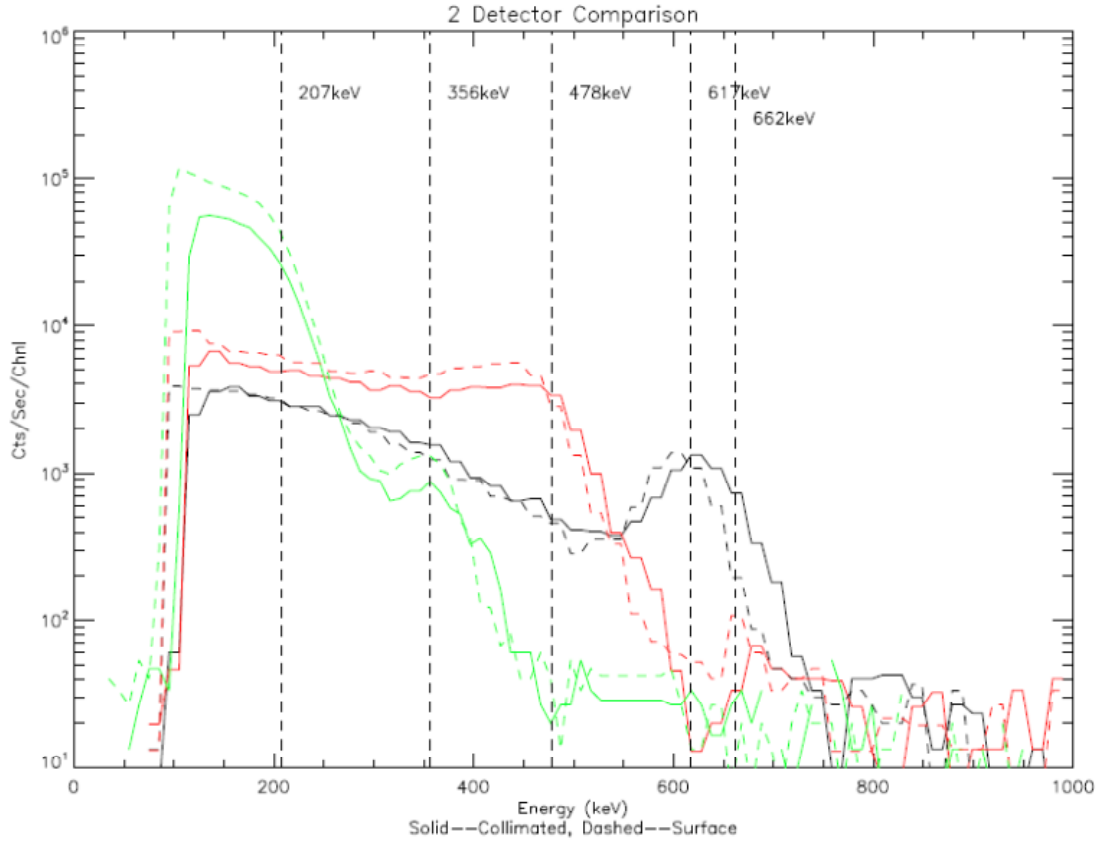


**Figure 35. UNH source testing of FIRE A. Collimated detector is shown in solid lines, surface detector in dashed lines. Different colors represent different sources.**

The three sources used in calibration provide three primary points that were used to generate the calibration. They were the 356 keV line in the Ba-133 source, the 662 keV gamma line from Cs-137, and the 598 keV electron energy peak from the Cs-137 beta source. This last line is worthy of more discussion. Cs-137 gives off a gamma ray at 662 keV, which can give rise to a conversion electron to produce the beta particle via electron capture. The exact energy of the electron depends on electron binding energies, but the most probable binding energy is 37.4 keV. Accordingly, the emitted beta peak is most likely at 624 keV [Blake, private communication]. However, this energy must then be reduced by the electron energy loss in the aluminum foil detector cover. This value is

obtained through use of a Geant4 model, which suggests that the most probable deposited peak energy for the electrons is 598 keV. A linear fit is then performed between the 3 deposited energy peaks to determine the conversion from detector channel to incident energy. This fit is performed for each detector independently as each has its own unique gain and offset.

From experience with similar detectors and electronics in previous missions, it was expected that the response function of the detectors could be characterized by the linear response function given below:

$$E = (ADU \times G) + Z$$

Here, E is the energy deposited in the detector, ADU is the digital number that is received from the electronics system, G is the gain of the electronics, and Z is the zero offset of the system. The precise values of G and Z are unique for each channel of a given DAPPER as well as to each individual DAPPER (and thus each FIRE). Consequently, the goal of the calibration is to determine the precise values of G and Z for each individual channel. As the stopping power of a 1500  $\mu\text{m}$  silicon detector is 1050 keV, it is typically assumed that the deposited energy in the detector will equal the incident energy minus the energy loss in foil, assuming that the incident energy was less than 1 MeV. At higher energies, the electrons will punch through the detector without depositing all of their energy, but those energies are outside the nominal instrument range; additionally we did not have access to electrons of these energies until calibration activities moved to The Aerospace Corporation's Beta Spectrometer. The assumption of instrument linearity was validated by use of an external precision pulser. Due to

commanding constraints, data was recorded using an oscilloscope which could measure both the input pulser peak (in mV) and the DAPPER shaper output pulse width (a duration in ns). This pulse width was then converted to a nominal channel number through the 14.7456 MHz (67.817 ns period) clock on the digital board. Figure 36 depicts the results of the test showing how the instrument response is linear over a large range in energies.

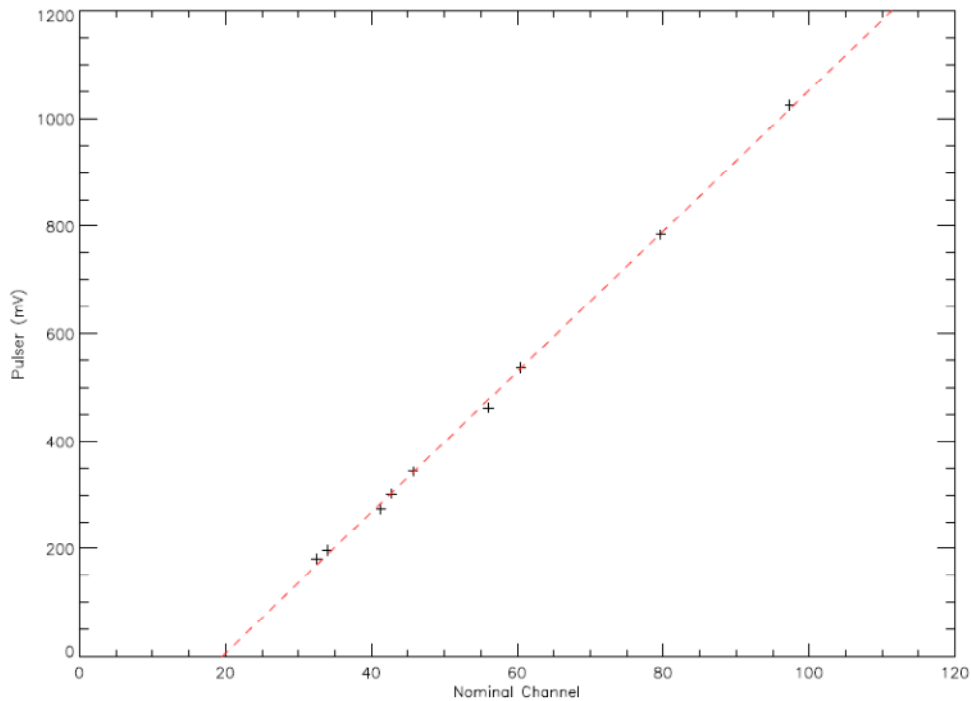


**Figure 36. Testing DAPPER linearity with a lab pulser.** Data was taken using an oscilloscope to measure input voltage from laboratory precision pulser as well as the DAPPER shaper pulse width (in ns). This pulse width was then converted to the nominal channel using the 14.7456 MHz digital board clock.

While each detector has a unique gain and offset that is set by resistors on the analog board as well as the internal DAPPER hardware, the flight software only permits setting a single set of digital channels for the two detectors.

Therefore, differences in calibration show up as an energy difference between the detectors. Accordingly, one of the goals of calibration is to measure the offset between the two detectors. The energy information along the x-axis is Figure 35 represents the average of the calibration between the surface and collimated detectors. The gains and offsets are tracked independently for data analysis, but the preliminary products will have slightly adjusted data channels. This is seen as how the 598keV peak actually splits the two detectors, as the collimated detector has a slightly larger gain than the surface detector.

In addition to determining the gain and offset through the use of the radioactive sources, the other major questions were the noise limits of the instrument as well as the upper and lower energy limits. Unfortunately source limitations made it difficult to test the full instrument range at UNH—so that was moved to testing at The Aerospace Corporation. However, noise performance of the instrument could be assessed through use of the onboard test pulser in the DAPPER. A test procedure was designed whereby the onboard pulser was turned on, and the instrument channels were stepped up at 1-bin width across the pulser range. As a result, the pulser peak would appear as a Gaussian with calculable FWHM, which was used to assess noise performance. The advantage of this test was that it could be performed in any conditions (vacuum or air), and at a variety of temperatures in order to assess temperature sensitivity of the instrument, as well as provide comparisons across units. Figure 37 shows the results of this pulser test for FIRE B (Flight Unit 1). The two pulser peak shows up in two different channels as expected owing to the different calibrations of the

detectors. The FWHM of each detector is ~60 keV, once appropriate calibration factors are folded in.

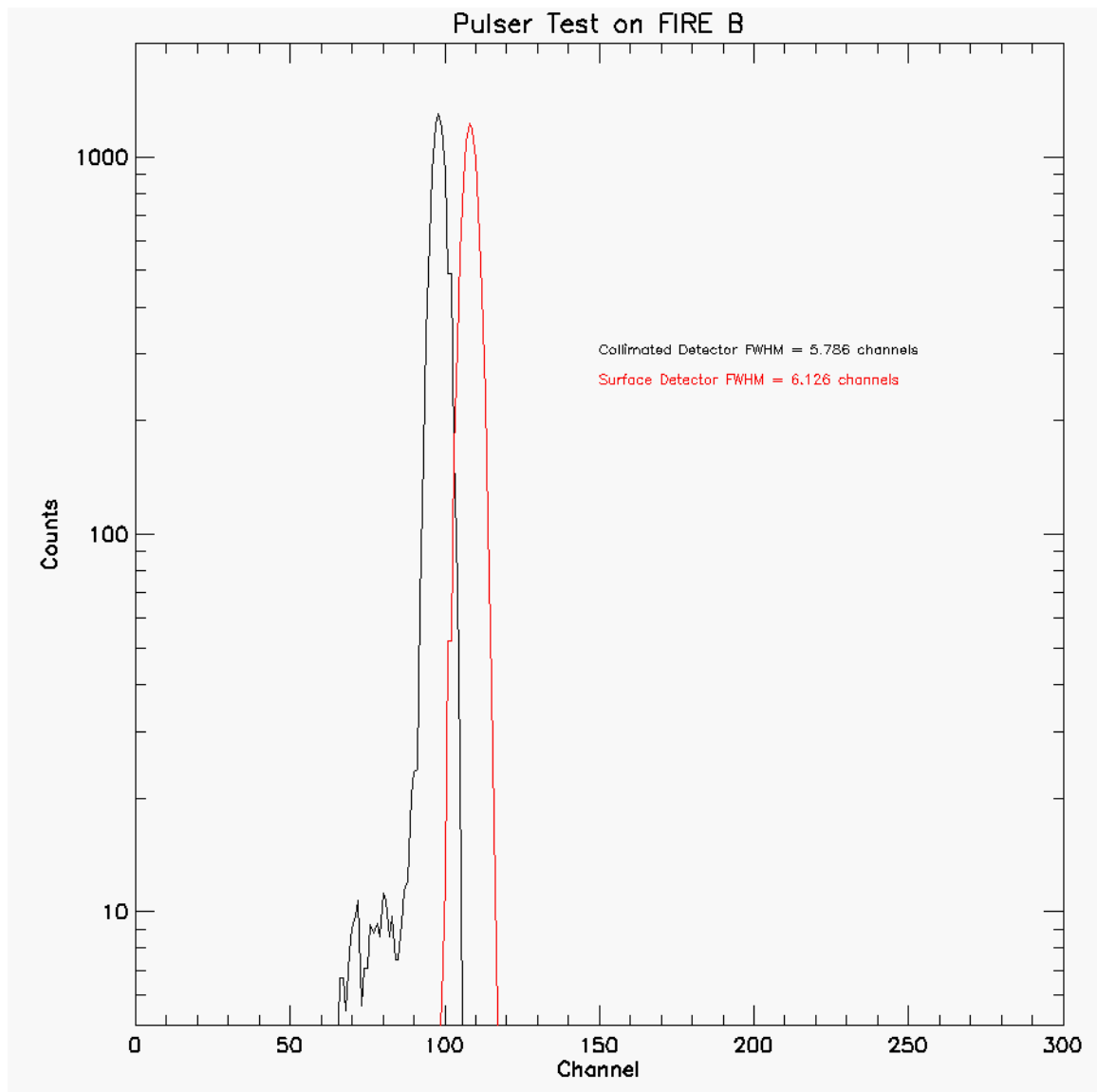


*Figure 37. Pulser test on FIRE B. The small step feature seen near channel 100 is the result of artifact of the GSE software, which did not appear in the flight software.*

#### **Beta Spectrometer Testing at The Aerospace Corporation**

In addition to the source testing that each unit underwent at UNH, in January 2013 the FIREBIRD "A" unit traveled to The Aerospace Corporation for further testing. Following this, in May 2013, both flight units traveled for final flight

calibration. There were several key advantages of this testing. First, the beta spectrometer produces high-energy electrons of selectable energy—an advantage over the source testing at UNH, which produced a broad spectrum with a few peaks. Secondly, as a necessity of using the electron beam, the testing was done in vacuum, which both improves performance (less scattering in air) and permits vacuum testing of components. Thirdly, although perhaps more relevant from an engineering perspective, the test was an opportunity to command the whole unit through BIRD, rather than through the GSE. While in theory this distinction would be of academic nature, in practice it provided another opportunity to test the system and discover unpleasant features sooner rather than later.

The Space Science Application Lab Beta Spectrometer has a long history of being used for calibration of spaceflight instruments at The Aerospace Corporation; incidentally, it was used for calibration of the MagEIS instrument on RBSP. Through use of an electromagnet, the electrons emitted by the radioactive source are subjected to a 90° turn. From a straightforward application of the Lorentz force it is easy to see that for a given magnetic field strength there is only a single energy for which the radius of curvature of an electron will match the radius of curvature of the spectrometer. Accordingly, as long as the source emits electrons at the desired energy it is possible to create a beam of a known energy, which will then be normally incident upon the detector when placed in the beam focus in the vacuum chamber.

For FIREBIRD's nominal energy range of 200-1000 keV, an ideal source to use is Sr-90. In fact, the Sr-90 source is actually a combination of Sr-90 and Y-90, which decay to Zr-90. Between the two of them, they are able to produce a source which emits electrons ranging in energy up to >2 MeV, while still producing significant numbers of electrons at a few hundred keV. If different energy ranges are desired it is possible to substitute other sources—for instance for very low energies (<200 keV) it is more efficient to substitute a Pr-147 source (which has an endpoint of 224 keV), and for very high energies it is possible to use a Ru-106/Rh-106 source which can produce electrons up to 3.5 MeV. Ultimately, for FIREBIRD testing the Sr-90 source was sufficient and so the other sources were not used in the beta spectrometer.

Testing in the beta spectrometer was designed to dovetail with requirements for validation of the Geant4 model of FIRE. Accordingly, testing was focused around two goals: energy resolution and angular response. To measure the energy resolution, FIRE was placed in a histogram (high-resolution lab testing) mode similar to the testing at UNH, but using the beta spectrometer beam at a variety of energies in order to map the energy response. To measure angular response of the instrument, FIRE was placed in its “Flight” configuration of energy channels and then subjected to different energy beams at a variety of angles.

In May 2013 both flight units were taken to Aerospace for the final flight calibration. This was conducted exclusively in the “histogram” mode, where the instrument rapidly scans over a large number of channels at a much higher

resolution to get detailed energy response. For each test, a 60 channel range was chosen which was then sampled over the course of 10 1-minute runs that were then stitched together. This was repeated for each detector on each unit (the spacecraft was rotated between tests because only one detector was in the focus of the beam at a time). The results of the calibration for the collimated detector on Flight Unit 1 are shown in Figure 38.

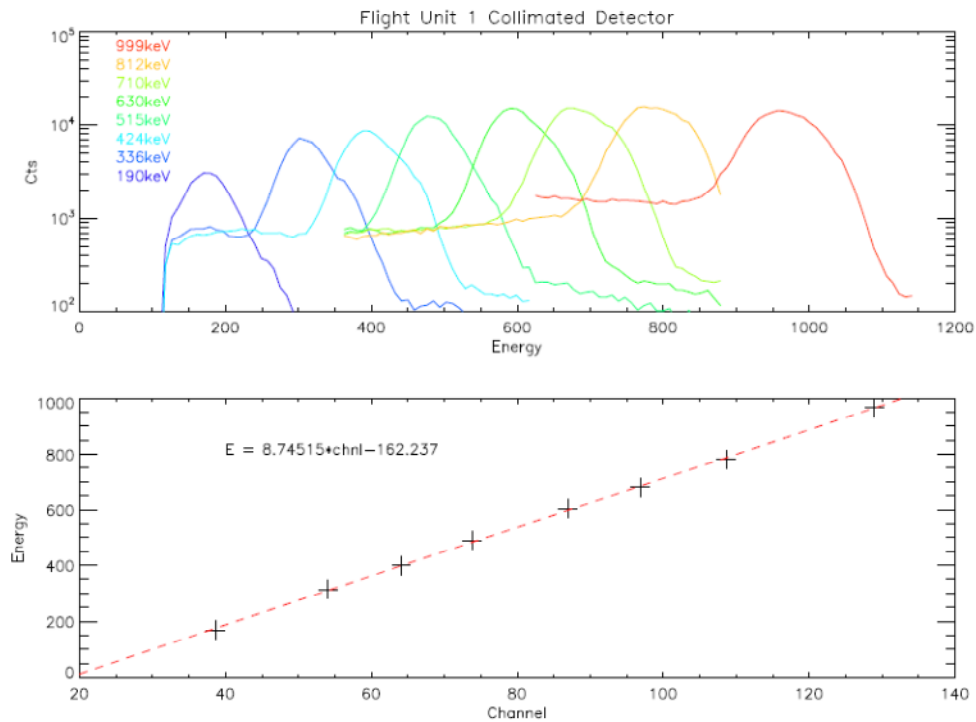


**Figure 38. Histogram results from Flight Unit 1 Collimated Detector. The top panel is traces in the highest energy resolution mode of the beam at different set energies. The bottom panel is a plot of the center channel of each peak showing the linear energy response and calibration coefficients.**

The top panel shows the results of eight different sweeps at energies ranging from 190 keV to 999 keV. Each beam appears as a nominally Gaussian peak in the instrument. The energies listed on the plot represent the incident

beam energy which is determined from the magnet settings. In the bottom panel, these incident beam energies are converted to maximum deposited energies by correcting for the energy loss in foil, using a correction from Geant4 modeling done by Brian Larsen (*Private communication*).

$$E_{Dep} = (E_{Beam} - 17.544 \text{ keV}) \times 0.9847$$

The resulting peak deposited energies were then plotted against a fit for peak channel. This is plotted in the bottom panel which shows (as expected) a linear relationship between deposited energy and detector channel. The slope of this line gives the detector gain, and the offset, is the zero of the unit. All four detectors tested (surface and collimated detectors on each unit) had an almost perfectly linear fit; however there was ~10% variability on in the gains reported between detectors, and up to 20% in the offset. The detector calibration coefficients are reported in Table 2.

<b>Unit</b>	<b>Detector</b>	<b>Gain (keV/chnl)</b>	<b>Offset (keV)</b>	<b>Gain <math>\sigma</math></b>	<b>Offset <math>\sigma</math></b>
Flight 1	Collimated	8.75	-162.24	0.066	5.68
Flight 1	Surface	9.50	-192.07	0.062	4.50
Flight 2	Collimated	9.85	-198.46	0.147	10.44
Flight 2	Surface	8.64	-182.90	0.099	7.69

*Table 2. Calibration coefficients for FIREBIRD Flight units.*

FIREBIRD has a nominal instrument range of 200 keV to 1 MeV. As can be seen in Figure 38, the instrument is actually sensitive to electrons below that value, as the 190 keV peak is clearly visible with little indication of noise. In flight of course, this data will be down-sampled into the six flight bins, and there will be a digital threshold imposed at 200 keV (if desired this value could be dropped as low as the analog threshold of ~150 keV).

The second major type of calibration testing done with the Beta Spectrometer was testing the angular response of FIRE. As the instrument is rotated, particles coming in off-axis will have different path lengths through the silicon. Consequently, the energy deposited will vary depending on the angle. This is particularly important for the highest energy particles, which might be capable of punching through the detector at normal incidence, but at an oblique angle are capable of depositing more energy. Moreover, the collimated detector would have a more limited field of view, and so there should be some angles outside the acceptance range. In an ideal world, the counts would go to zero in that case, however, it was known that it was not an ideal collimator and so some electrons could “bounce” down the collimator to the detector. For these runs, testing was done with the unit in the ‘Flight’ configuration—five logarithmically spaced bins between 200 keV and 1 MeV, with the sixth bin used as an integral  $>1$  MeV channel. The results of the testing for a two-minute run are shown in Figure 39. This also highlights the differences in resolution between the ‘histogram’ (or lab data) and the ‘flight’ data produced. Also visible in that figure is the  $dE/dX$  peak around 500 keV that comes from the  $>1$  MeV electrons punching through the detector. Additionally, a ‘background’ run was done with the source blocked off to measure that count rate. While it is not zero, it is a small fraction of the normal count rates, and only really appears in the lowest energy channel (but explains why we would not want to drive the threshold too low).

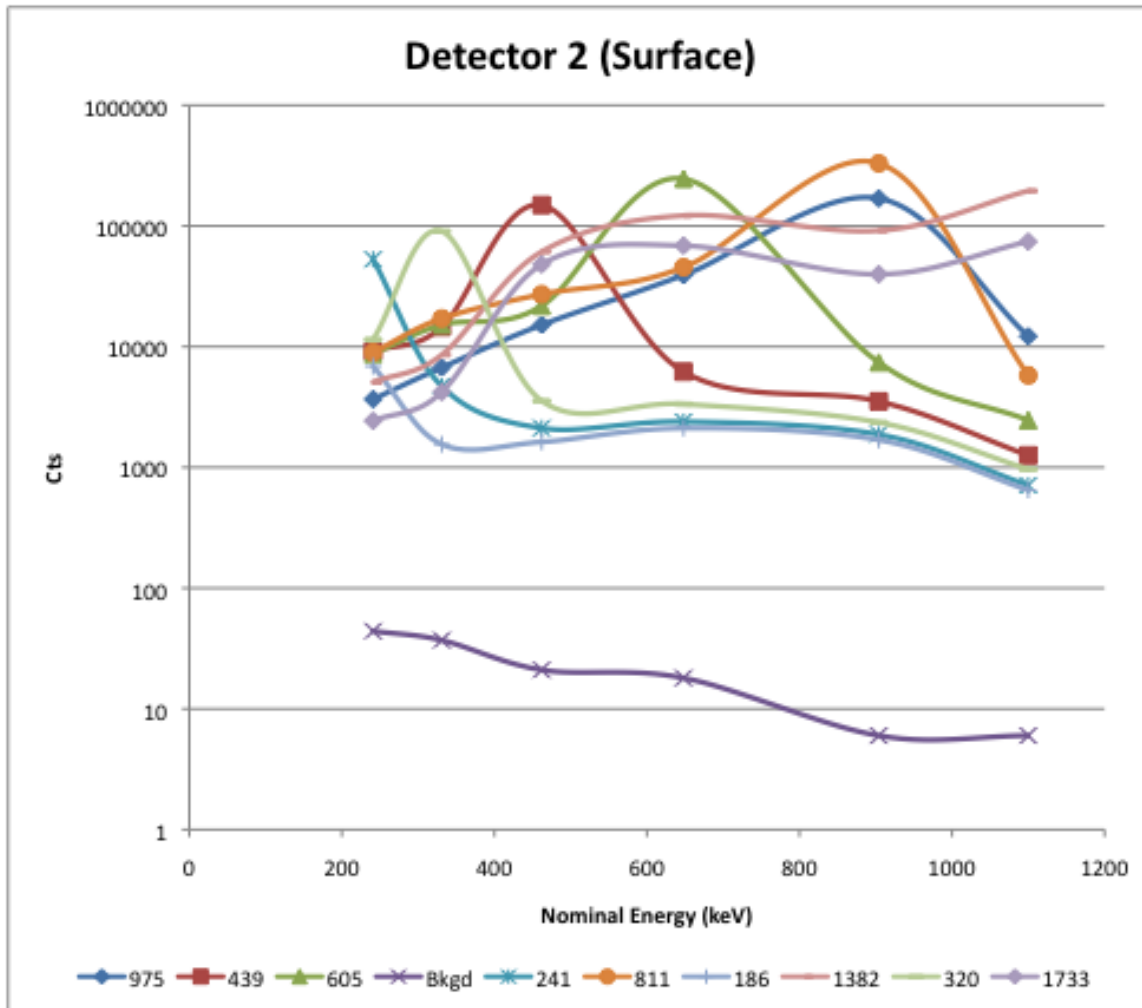


**Figure 39. Normal Incidence on surface detector.** Here the instrument is in flight configuration with very wide energy bins. As expected the energy peaks fall in the correct bins within the nominal (200-1000 keV) energy range. At higher energies, the peak moves to the lower energies predicted due to the electrons punching through the detector. Background counts are a small fraction of the total.

### Geant4 Model validation

The final stage in calibration was to create a Geant4 model that would be used to define the instrument response function. From the instrument response function it is possible to generate geometric factors, as well as angular and energy response for all the values and configurations that it was not possible to test for in the lab. Brian Larsen at Los Alamos National Laboratory did the actual coding of the Geant4 model; consequently I will not delve into a detailed

description of the model and its precise construction, but will instead provide a brief overview of it and its uses for FIREBIRD.

The Geant4 model works by building a model of the spacecraft and the materials used, and then shoots a large number of particles of set energy at it, measuring the energy deposited in different locations. By combining a wide range of energies, and incidence angles it is possible to compute the full instrument response function. A Geant4 plot of the instrument response for the surface (uncollimated) detector is shown in Figure 40. Six different energy channels were defined for the run: 200-279 keV, 279-388 keV, 388-541 keV, 541-754 keV, 754-1050 keV, and >1050 keV.

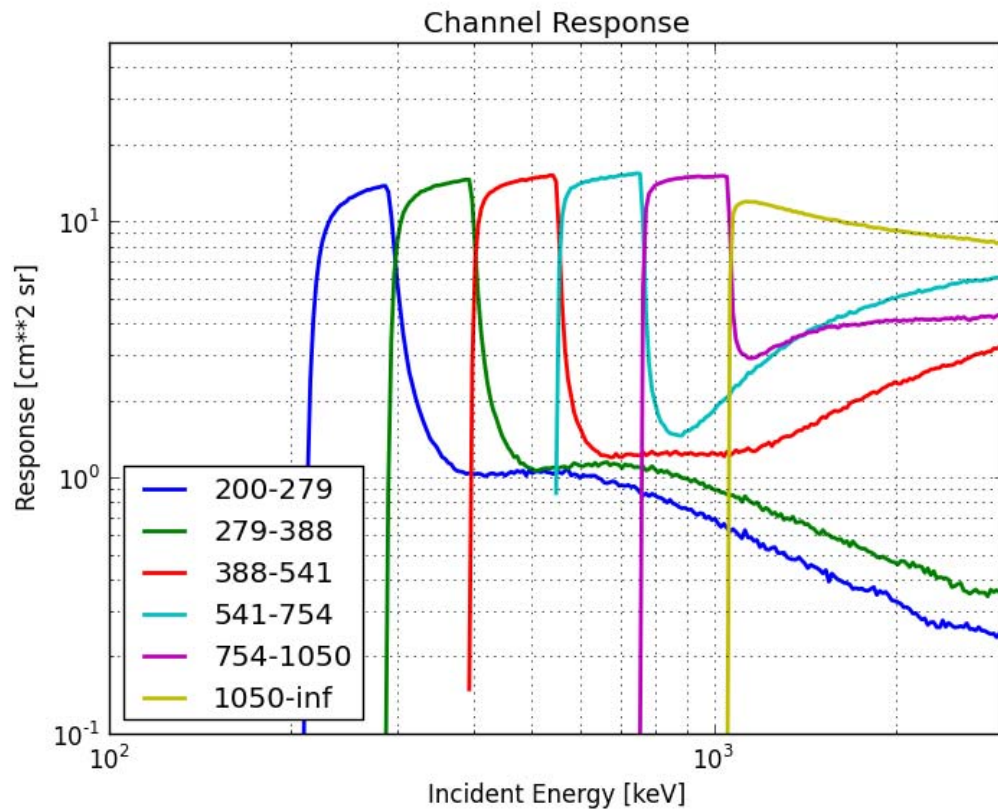


**Figure 40. Geant4 Model of instrument response in each of the 6 nominal flight channels for the uncollimated (surface) detector. Figure courtesy of Brian Larsen.**

These channel numbers resulted from initial testing of the ‘A’ unit and the resulting estimates of what the flight channel boundaries would be. Each color represents a deposited energy falling into a given range. The left-most (blue) curve represents all particles that deposit between 200 and 279 keV in the detector. The plot shows that the minimum incident energy to appear in that channel is just over 200 keV (the difference is due to energy loss in the foil over the detector), and that the response shoots upward very quickly before flattening across the channel range, before falling off relatively quickly as the incident energy approaches the next channel boundary. In an ideal world, the channel response would be perfectly flat across the channel and then fall to zero once

outside the boundaries. It is also useful to note that the highest energy channel (the >1MeV integral one) has the most complicated energy profile. Nonetheless, it reinforces the belief that we are accurately mapping energy channels to the electron deposited energies.

### **Conclusions**

FIREBIRD is a CubeSat mission specifically targeted to microburst science. From a science perspective, the mission is built around a number of open questions about microburst characteristics and generation mechanisms that require multipoint measurements of microbursts. FIREBIRD's mission science objectives and the specific measurement requirements to meet them are based on research described in earlier chapters of the thesis. FIREBIRD's science objectives require coordinated high-resolution measurements capable of both identifying and resolving the characteristics of individual events. The design, construction, and testing of the instrument serve to answer the question: "*What is required to create the next set of microburst observations to make substantial progress in understanding?*"

One of the themes from Chapters 2 and 3 was the use of single point measurements to reveal interesting characteristics (location, size, etc.) of microbursts that in turn lead to more questions (energy range, connections with chorus). These unresolved questions require some sort of multipoint measurement, either in physical space (two spacecraft identifying bursts simultaneously) or energy space (a wide energy range to search for breakpoints in the energy spectra and thus identify resonance regions). The FIREBIRD

mission is designed to respond to these sorts of questions and take advantage of the knowledge gleaned from these studies. Here the single point observations provide the inputs into the questions and design of the multipoint mission that is intended to provide closure.

# CHAPTER 5

## ASSESSING GLOBAL LOSS

### Motivation

The objective of this chapter is to broadly estimate the scale and variability of the totality of microburst precipitation over the course of an entire storm.

Understanding the total loss due to microbursts gets at the heart of the question of what is the geo-effectiveness of microbursts as a radiation belt loss mechanism. This question of geo-effectiveness comes from the conclusion that the radiation belt dynamics are governed by the interplay between the various source and loss terms (Reeves et al., 2003). This conclusion motivates the desire to quantify source and loss terms independently. Prior estimates from SAMPEX (O'Brien,Looper and Blake, 2004) concluded from studying a handful of storms that the total loss due to microbursts could be sufficient to empty the outer radiation belt of MeV electrons in a single day, plus or minus an order of magnitude. That order of magnitude uncertainty (which comes from a number of assumptions that had to be made) is crucial for understanding the geo-effectiveness. Losses within a single day or less are sufficient to be a leading driver of dynamics, whereas if the loss rate is down near the lower end (requiring upwards of a week to see the necessary losses) then microbursts alone are clearly unable to explain the measured losses. This thesis chapter focused on answering the question: “*What is the global scale of microburst precipitation?*”

### **Coordinating Multipoint and Single Point measurements**

One of the biggest challenges in estimating the total loss due to microbursts is that the events occur over a very large portion of the magnetosphere simultaneously. Accordingly, to solve the problem properly requires instantaneous measurements of microburst frequency and size at all locations across the magnetosphere—an unfortunate impossibility due to cost and other logistical constraints. The prospective method for addressing this issue is to combine single point high-resolution measurements of microbursts (and thus their characteristics) with more broadly distributed measurements of event occurrences. This involves taking the general question of microburst losses and dividing it into 2 sub-questions. The first is, “*When and where are we seeing microbursts?*” and the second is, “*What happens every time we see a microburst?*” To answer the first question requires simultaneous measurements of microburst occurrences or a suitable proxy measurement. Fortunately, the requirements for measuring whether or not a microburst occurred are substantially less than the requirements for measuring the detailed characteristics of an individual event. To answer the second question the requirements are higher—we want high time resolution as well as a clear measurement of the precipitating population (good count rates). However, it is quite feasible to think about doing this from single point measurements—if they are of sufficiently high fidelity.

These questions suggest a multifaceted approach to the problem. Missions designed to place a large number of payloads in a variety of locations (such as

BARREL, FIREBIRD in the periods well after launch with the event identification data, etc.) can be used to address the questions of microburst occurrence rate, location and timing, while detailed measurements of individual events (using the high resolution event data from FIREBIRD, for instance) can be gathered in a variety of locations to address the characteristics of the individual events.

### **Estimates from SAMPEX**

In an ideal situation, multipoint measurements of event frequencies and locations are combined with detailed measurements of individual bursts to build an estimate of the total loss due to microbursts. Such observations are not available at this time for this thesis. However, the depth and breadth of the SAMPEX observations suggest a method to build initial estimates. Although during any given storm SAMPEX's orbit precludes it from measuring microbursts from more than a sliver of local times, the long time range of observations permits a form of epoch analysis. By separating out all storm times (defined as events with minimum DST < -50 nT), a data set of 231 storms was compiled, as discussed in Chapter 2. Each storm was broken into main phase and recovery phase components, and then each phase was compiled into a map for comparison to the data set of all events. The results of this comparison are presented in Figure 41.

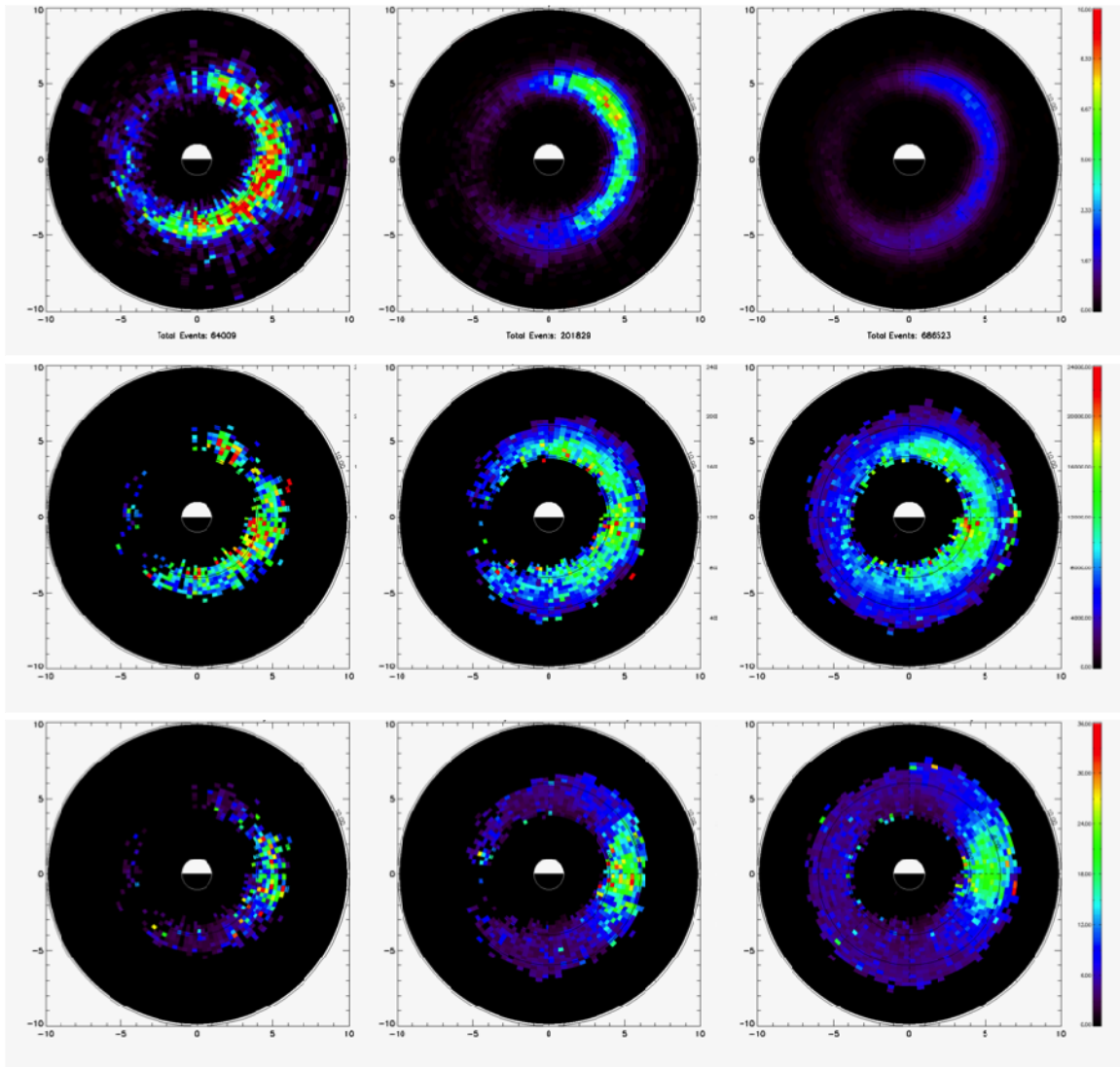


**Figure 41. Comparison of microburst characteristics across storm phase.** From left to right are main phase, recovery phase, and all events (total). From top to bottom, the plots are ordered as event frequency, event absolute intensity (total loss), event relative frequency.

Here, the figures are all on the same color scale and a few notable results stand out. The first is that the event frequency varies strongly across event phase in both overall level and distribution. The main phase sees the most frequent events, as well as a shift closer to midnight in location, while the recovery sees elevated (but not as much as during the main phase) frequencies but with a similar distribution to that of the entire data set. By contrast, the event intensity,

whether viewed as the total loss, or as the relative intensity, is remarkably constant across storm phase. Accordingly, the conclusion is that the total loss due to microbursts is primarily driven by variations in event frequency across storms, as opposed to variations in the size of the events. Therefore, this suggests a plan for building estimates using only the SAMPEX data. The basic scheme is as follows:

- 1) Using the long-term measurements from SAMPEX build up a historical map of microburst characteristics (event frequency, intensity) during each phase of the storm, and call these the baseline maps.
- 2) For a given storm, determine the particular swath of local times that SAMPEX would have sampled during the storm.
- 3) Compare the measured event frequency in the MLT, L bins that SAMPEX sampled during the storm, with the appropriate baseline frequency. Using a weighted average, produce an appropriate scaling factor for the event frequency in the sampled bins as compared to the baseline.
- 4) This scaling factor is then applied across the board to the entire baseline event frequency map to produce a scaled event frequency map for the entire storm phase.
- 5) This event frequency map (event/minute) is then convolved with the average event intensity (electrons/event) and geometric consideration (physical size of each MLT, L bin) to produce an electron loss rate in electrons/hour.

- 6) This loss rate is then multiplied by the duration of that particular storm phase for the storm in question to produce a total integrated loss for the entire storm phase.

Once that is done, the total loss can be compared with estimates of the total pre-storm population of the belts for context. This process is iteratively shown in Figure 42. The map at the top left represents the baseline event frequency from all main phase measurements in the database. At top right is a map showing the location (in MLT, L) of all SAMPEX observations during the storm, with the relative amount of time spent in each bin. At the bottom left, then, is a corresponding mask showing the expected results if that storm perfectly matched the baseline average (if every storm was exactly the same). Here we see that the primary sampling was along the dawn-dusk meridian. Finally, in the bottom right is the actual event frequency as measured by SAMPEX during this particular storm. The scaling factor is then calculated by comparing the bottom right plot to the bottom left plot.

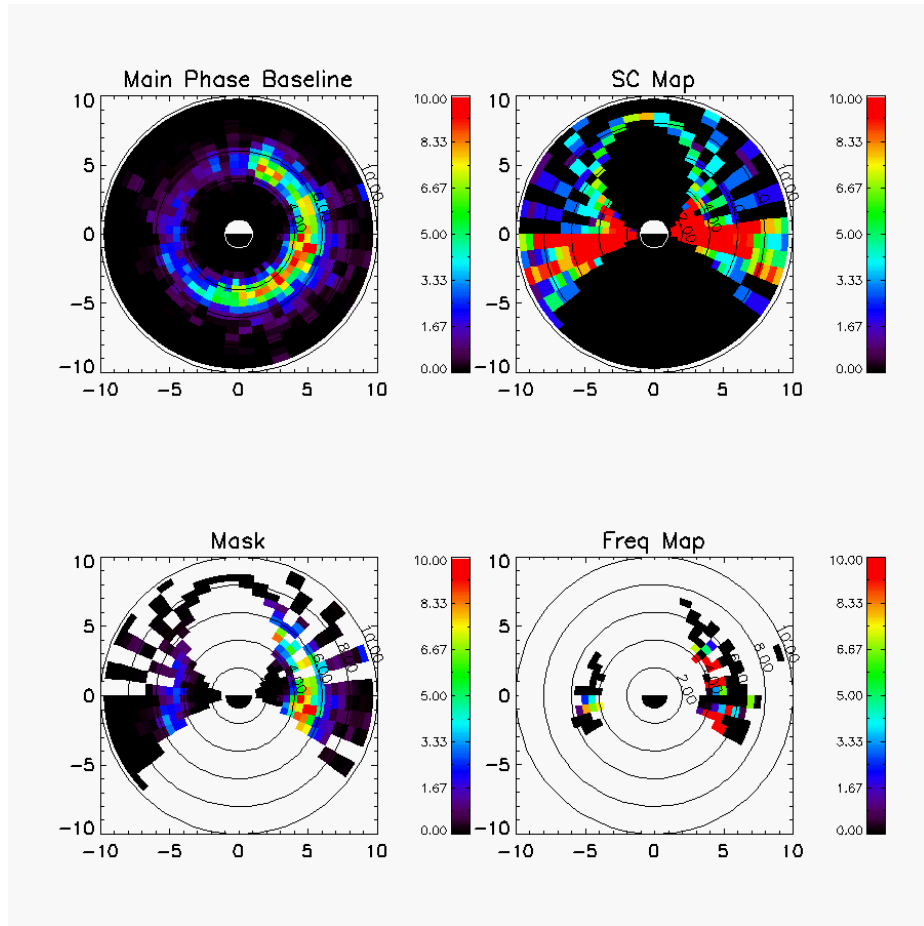


**Figure 42. Producing a storm event frequency map.** Top left is the baseline main phase event frequency map (events/min). Top right is a map of where SAMPEX's observations come from. Bottom left is applying that map of observations to the baseline. Bottom right is then the actual event frequencies as measured by SAMPEX for that storm. The storm in question is the October 1998 storm that was part of the GEM challenge. All plots are in MLT, L.

One of the features of this approach is that it ignores the area of an individual microburst event from the calculation of the overall loss rate. This is a feature of the measurement definitions and the way the various quantities are defined. Microburst event frequency is measured or defined as number of observed events per minute. On a relative scale this makes it easy to observe variations, but on an absolute scale this number does not take into account the size of a microburst. If a microburst is very small then there is a greater probability that an event that occurs within a given MLT, L bin while SAMPEX is

in that bin will be outside the field of view of the instrument. In an ideal case a microburst is large enough that if there is a burst anywhere within a single bin then it is observed by SAMPEX. Thus the relative microburst occurrence frequency will be lower than the absolute microburst occurrence frequency by a factor that depends on the ratio of the microburst area to the area of the particular MLT, L bin in question. However, when we turn around and calculate the total number of electrons lost within a given burst we in turn are only measuring the total number of electrons that reached SAMPEX (once the geometric factor is accounted for). The calculation assumes that simultaneously, the flux observed by SAMPEX is the same across the entire MLT, L bin for the duration of the event. If a microburst is much smaller than the size of a bin, then this will overestimate the total number of electrons lost in a single event (although a relative comparison among events is still valid). However, the ratio by which we are underestimating the event occurrence rate (due to the “missed” events) is the same as the ratio by which we are overestimating the loss during a single event due to the area where an event is not occurring. Consequently, as long as the bins are small enough that there is not significant variation in event properties across the bin, then the loss rate due to microbursts will be both unaffected by bin size and by the size of a particular microburst event. This is shown in equation form below:

$$\frac{\text{Events}}{\text{Min}}(\text{MLT}, \text{L}) \times \frac{\# \text{flux}}{\text{event}}(\text{MLT}, \text{L}) \times (\text{Bin Area})(\text{MLT}, \text{L}) = \frac{\# e^-}{\text{min}}$$

Once a total loss for each storm phase is reached, the results can be compared across events. Figure 43 shows a histogram of these results for both the main

phase and the recovery phase. As can be seen from this histogram, typical main phase total losses fell between  $10^{22}$  and  $10^{24}$  electrons. During the recovery phase these total losses were a bit higher but still in the same general range. The uncertainty of a given measurement is a bit harder to quantify, but based on the estimates from similar types of work in (O'Brien, Looper and Blake, 2004) or (Lorentzen et al., 2001) an order of magnitude is not a bad starting point for an estimate based off of single-point measurements.

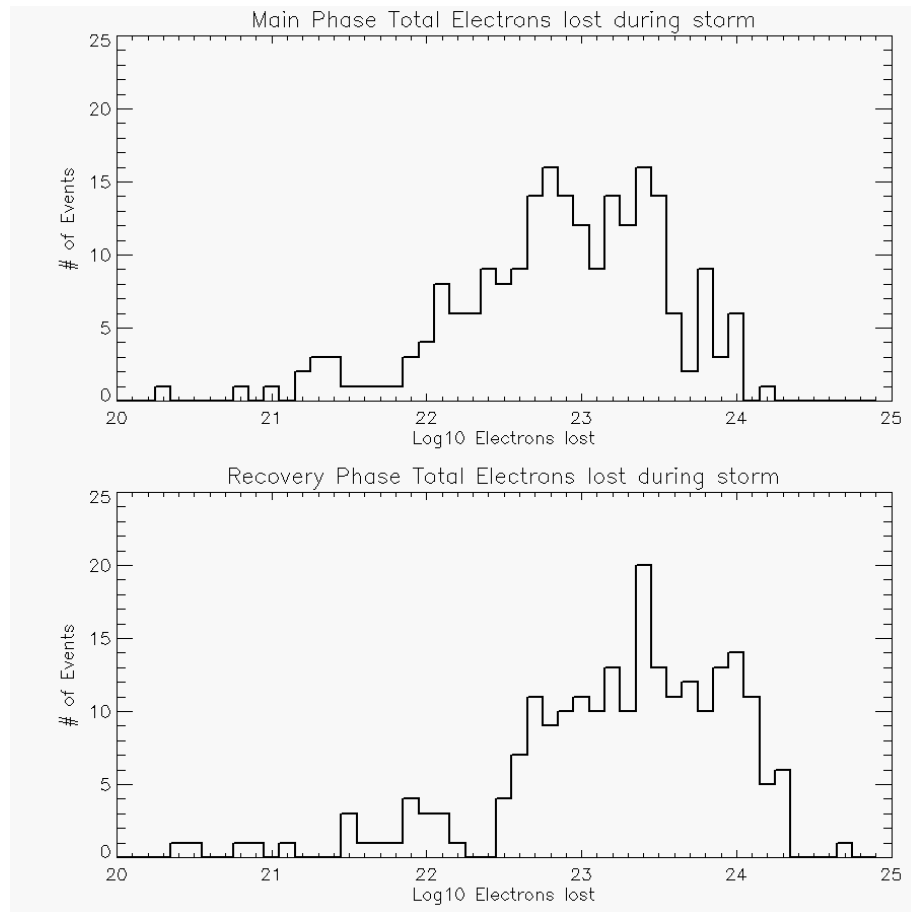


**Figure 43. Total loss across events.** Typical losses during the main phase of storms fell between  $10^{22}$  and  $10^{24}$  electrons. Additionally, there was a lower-loss tail, of a handful events below  $10^{22}$  total electrons for which microbursts were likely not very significant. During the recovery phase the total losses were generally higher, but this was due to the longer duration of recovery phases relative to the main phase—the loss rate was higher during the main phase.

The total loss due to microbursts across an entire storm is by itself a very large number, but one without significance until it is compared to other useful quantities. Estimates of the total population of the Earth's outer radiation belt are a bit tricky, but nonetheless a few efforts have been made. Estimates from POLAR data put the typical outer zone population of  $>1$  MeV electrons at  $\sim 10^{25}$  (Baker, Kanekal and Blake, 2004), but note that there is a multiple order of magnitude variability over the variety of conditions seen within the solar cycle. Other estimates (Selesnick and Kanekal, 2009) produce similar numbers but perhaps slightly higher (but make the estimate at a number of different energies) and highlight the significant variability on a number of timescales.

Ideally, it would be possible to calculate the pre-storm population of the outer radiation belt for that particular storm, rather than use a baseline value. In the future, the best estimates would come from Van Allen Probes, which can measure the energy and pitch angle distribution of the equatorial population and convert that into phase space density (PSD). PSD has the advantage of ignoring adiabatic effects; integrating PSD over all three adiabatic invariants as well as the volume of the radiation belts would give a calculation of the total electron population. For the events in question for this study Van Allen Probes was not operational, but it is possible to estimate the trapped population using a method detailed in O'Brien *et al.*, [2004]. SAMPEX is capable of measuring a fraction of the trapped population corresponding to a small range of equatorial pitch angles that allow the electrons to reach SAMPEX's orbit. If we assume a  $\sin^n$  pitch angle distribution, then it is possible to extrapolate the entire equatorial population from

that particular n value. These pitch angle distributions can be inferred from measurements on other spacecraft (such as Polar, which measured electrons in a polar orbit and thus saw many different equatorial pitch angles) or using other measurements of the pitch angle distribution from the literature. This gives the correct density as a function of L, and then a proper integration over the entire volume of the radiation belts gives total electron content. For the October 1998 storm modeled in Figure 42, literature produces a calculation of  $1.1 \times 10^{25}$  electrons pre-storm and a post-recovery value of  $2.6 \times 10^{25}$  (O'Brien,Looper and Blake, 2004). Our estimates for the total loss in question during that storm were  $3.3 \times 10^{23}$  electrons in the main phase and  $2.1 \times 10^{24}$  during the recovery phase, or approximately 3% in the main phase and 10% in the recovery. Even these values have significant uncertainties associated with them, but they are a starting point for general analysis. Moreover, they suggest that  $10^{25}$  is a reasonable starting point for estimates of the 1 MeV outer zone population.

So if we use  $10^{25}$  as a reasonable estimate of the pre-storm outer zone population, but with the caveat that there is significant variability in that number it provides a lens through which to view the histogram data on microburst loss during storms. A loss of  $10^{23}$  electrons during the main phase (the middle of the broad peak seen in the histogram distribution) would therefore likely represent only 1% of the total population. Now, given the large uncertainties at play it is unlikely but not inconceivable that this would be a significant loss. However, that means that results further down in the tail (those near  $10^{21}$ , or  $10^{22}$  electrons) would definitely represent events where microbursts play an inconsequential role

in the overall dynamics. Returning to the events located with the broad peak from  $10^{22}$  to  $10^{24}$  electrons, here it would require the technique to underestimate microburst loss at the same time as the estimate of outer zone population is on the lower side than reality for it to represent a significant loss. Combined, these suggest that microbursts are likely only an occasional driver of total losses, although there may certainly be particular events where microbursts dominate. Unfortunately, it is difficult to make this conclusion too forcefully given the necessities of the uncertainties involved in a single point measurement.

It should be noted that the total losses are a bit higher during the recovery phase, as compared with the main phase. This is due to the longer duration of the main phase—overall we see higher loss rates during the main phase (tied to a greater microburst occurrence rate), but the recovery (and microburst activity during the recovery phase) persists for much longer periods of time than the often-short main phase. One possibility that is not discussed in detail within this thesis is the idea that the microburst precipitation is intimately tied to some of the wave acceleration (O'Brien, Looper and Blake, 2004) that is going on during the recovery process (the difference between acceleration and loss being tied to particular resonant conditions and a particles location in phase space). It is possible to see how the scattering of electrons leading to precipitation also plays a role in wave generation (Hikishima et al., 2009), where the precise phase space distribution of the relevant particles plays a key role in the total outcome. Astute readers might wonder how this compares with results from O'Brien *et al.*, [2004] which suggested that the total loss was higher during the main phase;

however there are a few relevant items of note. First, O'Brien *et al.*, [2004] only calculated the results for a small handful of storms (the GEM storms), and noticed some variability in the relative strength of main phase and recovery within that small set. A direct comparison of our method on the same storm produced similar results. Secondly, the storms selected in that paper were ones where SAMPEX was in a primarily dawn-dusk orbit. This is significant because they compared microburst precipitation measured in that orbit during the main phase and the recovery. However, as shown in Chapter 2 the regions of principle microburst activity shift from main phase to recovery. Statistically speaking, the dawn sector (where SAMPEX was observing) sees the highest fraction of main phase events, and is outside the region of most common recovery phase events. Consequently, a direct comparison of the counts at that MLT would naturally bias towards overrating the main phase—a result which is unknowable without detailed statistical maps of the storm phase averages.

### **Expanding to Multipoint**

Estimates of total loss based on a set of single-point observations are a useful starting point for the study but suffer from larger uncertainties due to the assumptions that must be made in regions that are under-sampled. With SAMPEX, the single point challenge was addressed by using long-term historical maps of microburst precipitation to try to add some of the benefits that would come with multipoint: a substitute but not a full solution. The obvious avenue for expansion to multipoint would be in the measurements of event frequency.

Event frequency is hopefully an easier characteristic to measure broadly than the detailed characteristics. To measure event frequency requires the ability to identify microbursts when they occur, which is something that can be done with a large geometric factor solid state detector in a low-earth orbit (such as on SAMPEX/HILT or FIREBIRD) as well as from balloon measurements of the bremsstrahlung produced when the precipitating electrons strike the earth's atmosphere. While there will be some confounding effects of different measurement techniques, it is not necessary to measure the precipitating electrons directly to determine the event frequency. As long as there is a spot-checking that the relevant event characteristics (as measured in chapter 2) still hold, measurements of the location and frequency of microburst events at a variety of points should permit a more narrowly bound estimate of the total loss due to microbursts. Additionally, measurements from spacecraft in an equatorial orbit, such as Van Allen Probes, (which permit the sampling of all equatorial pitch angles) at multiple points can be used to generate better estimates of the pre-storm radiation belt content for each individual storm, rather than relying on broad, historical, averages. Rather than being forced to compare the distributions of microburst loss against total population (on average), it can be done on a storm by storm basis to hopefully add meaningful physical constraints.

### **Conclusions**

The aim of this chapter is to address the following guiding question: “*What is the global scale of microburst loss?*” Scientifically, the motivation for this question is rooted in a desire to understand the physical significance of

microbursts as a radiation belt loss process. In order to properly answer this question, it is necessary to know both the total loss due to microbursts, as well as an appropriate number for context (either the scale of competing loss mechanisms or a reasonable estimate of the pre-storm population). Fully answering this question requires multipoint observations of both microbursts and the state of the radiation belts simultaneously. However, by leaning on work from SAMPEX, it is shown how the single larger problem separates into two smaller components—namely, “when and where do microbursts occur”, and “what happens during a typical microburst.” Since most of the differences in microburst characteristics over the course of the storm come in changes in the event frequency, the problem can be reduced to a simpler set of measurements. Finally, I present an approach for generating an estimate of total microburst loss from a set of single spacecraft measurements (SAMPEX) that can be extended to multipoint when that data becomes available. From a single set of measurements it is possible to estimate the total loss due to microbursts, albeit with both substantial uncertainties, as well as a substantial spread in measurements.

Despite the large quantitative uncertainties intrinsic to the single point measurements, it is nevertheless possible to draw some preliminary conclusions from the data, even if the real value lies in developing a framework for multipoint analysis. The large range in total losses due to precipitation suggests a considerable variety in the efficacy of microbursts as a radiation belt loss mechanism. The fact that the mean loss due to microbursts is much smaller

(~100x) than typical estimates of the pre-storm population of the outer zone, suggests that there certainly are cases where microbursts are not a significant factor in governing the dynamics. It is important to be very careful in stating the conclusions; while the data supports the idea that there clearly are storms where microburst precipitation is a minor factor, this should not be extended too far. There may indeed be storms where microburst precipitation is a very important (or even dominant) factor—such a result cannot be ruled out from the data as presently constituted, although it appears somewhat unlikely.

# **CHAPTER 6**

## **CONCLUSIONS AND FUTURE WORK**

### **Summary**

The goal of this thesis is to properly characterize and describe the global distribution of microbursts with an eye towards quantifying the total loss due to microburst precipitation and then properly placing it within the context of radiation belt and magnetospheric dynamics. The basic challenge underlying the thesis is how to infer broad global properties from single point measurements. The overall concept is to use single point measurements to identify key characteristics and provide preliminary conclusions, so that they can be critically evaluated in the future with coordinated multipoint measurements.

The four focus questions highlighted in the introduction serve as a map for understanding microburst precipitation. Each chapter focuses on one of these in turn through a particular data set (e.g. SAMPEX, Freja, FIREBIRD). Future work therefore involves taking this assembled framework of single-point observations and testing and expanding through the use of coordinated multipoint measurements. That is not to demean the utility of single point measurements; or suggest an inability to complete the work. Rather, the thesis focuses on the process of transforming the individual measurements into a coherent global picture. Continued focus and refinement of the process as embodied within the focus questions is how the overall outcome goals are realized.

### **Focus Questions**

The first focus question, “How do microbursts vary/how are they similar,” is directed at the large database of SAMPEX observations of individual microbursts. These observations came from a wide variety of conditions and focus on critical characteristics of individual events: when and where do they occur, how large are they, and how long is an event. Microbursts are seen primarily on the downside of the magnetosphere at radiation belt L shells. While microburst precipitation covers a very large swath in local time, typically events are most frequently seen in the post-dawn/pre-noon region, whereas the strongest events are most commonly seen close to dawn. Event intensity is highly variable between individual events, but tends to follow power-law like distributions over the two order of magnitude variability. Event durations, are typically of the order of 100ms.

These characteristics of microbursts are all based on single point measurements and are centered around the basic question of what a microburst is, and the applied question of what is required in order to observe one. These requirements inform mission design (as discussed in the chapter on FIREBIRD), and are a key component in understanding how to extend from single-point to multipoint observations. Beyond the simple question of what the key characteristics of microbursts are is the question of how they vary. This is addressed by considering an epoch analysis of several hundred storms over the lifetime of the SAMPEX mission.

Across storms there is both notable variability and consistency in microburst characteristics. The most significant variability is in the event frequency and location. During quiescent times, microburst precipitation can almost disappear, whereas during storms event can occur at a much higher frequency. Moreover, the location of the microburst events shifts over the course of storms. During the main phase of storms, not only is the overall microburst frequency higher, but it occurs preferentially closer to midnight, while by the recovery phase, the overall rate is still elevated (although not as much as during the main phase), but the location of events shifts more to the dayside. These changes, combined with the relative consistency of the event size distribution across storm phases suggest that event frequency is the most important characteristic to systematically monitor.

The second focus question was, “What are the physical mechanisms involved in the generation of microbursts?” Time of flight analysis permits a single point measurement to be used to determine a source region for an individual microburst event. Taken together, the results from Freja generated a 3-dimensional region from which microburst events issue. This region encompasses an equatorial swath of the downside of the magnetosphere. This area is strongly aligned with regions of the most intense chorus activity, as measured from CRRES and THEMIS. While the measurements of chorus are not from the exact same time as the measurements of microbursts (and thus a 1:1 correspondence has not been observed), it furthers the link between the processes.

There are several reasons for wanting to understand the causal mechanism for microbursts. The first, and most fundamental, is that it is a basic scientific question. That of and by itself has value, but beyond that, understanding the generation mechanism has implications for understanding when and where microbursts occur. From an application standpoint it opens a fundamental question of the order in which the measurements lead to inferences. For much of the thesis, the question has been based around whether chorus lead to microbursts. Understanding microburst science is the goal, and so the objective for studying chorus in its relation is to build better estimates for total loss due to microbursts.

However, it is possible to turn this question around—a potential arena for future work. If we extend the conclusions of the thesis beyond correlations between microbursts and chorus, to assume that chorus causes microbursts, it raises the question of whether or not an observed microburst can be used to infer chorus activity. Beyond that, if it were possible to infer chorus activity (not a given), would it also be possible to ascribe any meaningful characteristics to it. Chorus has been ascribed to both acceleration and precipitation process (Bortnik and Thorne, 2007) and so it is not inconceivable that microbursts could serve as a tracer for other chorus activity (O'Brien, Looper and Blake, 2004). While the idea that chorus could have simultaneous precipitation and acceleration effects at different energies has been introduced before (Horne, Glauert and Thorne, 2003), it remains to be seen if any sort of useful quantitative or qualitative predictions can be made from spacecraft measurements. As a topic for the

thesis, this is mostly about understanding the mechanisms responsible for microburst precipitation (and where they occur); as a topic for future work, this thesis serves as a jumping off point for future explorations.

One of the central ideas to all of the questions in this thesis is how to address fundamentally multipoint challenges (involving global quantities) with single point measurements. The obvious next step is then to extend these measurements to the multipoint domain. Some of this is accomplished by novel techniques for combining data sets, while other parts require making hypotheses from single point data that must be tested once multipoint data becomes available. The extension of single point measurements into the multipoint domain represents the principle thrust of the future work from this thesis.

However, just because the extension to multipoint measurement is a large component of future work does not mean it does not play a key role in the work contained within the thesis. The third focus question, “What are the tools required to create the next set of microburst observations” deals with precisely this challenge. In this case, FIREBIRD is both the specific and the general answer to this question. On the general level, FIREBIRD represents a coordinated multipoint measurement of microburst characteristics. This is the type of measurement that is required to take the next step forward. In the global picture, the single point measurements provide the first results as well as generating testable predictions, but it is for multipoint to test these assumptions.

At a specific level, FIREBIRD is designed in response to both open questions in microburst science, as well as in specific response to previous

measurements. The results from the SAMPEX mission played a critical role in determining the specifications and requirements of the instrument as well as the concept of operations for FIREBIRD. Details such as the size (relative intensity) and duration of microbursts turn around and define the requirements for FIREBIRD. The desire to test broader results inferred from single point measurements (namely the association between microbursts and chorus) sets the mission concept: calculating the scale length of microburst precipitation for comparison with that of chorus.

The overarching idea is that hardware requirements are driven by a fundamental desire for multipoint measurements. A CubeSat platform is an ideal vehicle for multipoint owing to its lower cost; however that introduces a number of engineering challenges to minimize the requirements for such a small bus. Consequently, the details of the chapter on FIREBIRD are about the need to distill the requirements from the earlier results into a practical and feasible instrument design. By taking advantage of the experience with Freja & SAMPEX, the single point measurements enable a more narrowly focused instrument design. This design than permits the testing of hypotheses and theories obtained using single point measurements in a multipoint laboratory.

One of the chief technical constraints for FIREBIRD is the limited telemetry budget, which is in turn driven by the limited power available to the spacecraft. Accordingly, the data products that FIREBIRD produces have to be scaled down. This increases the pressure to be able to narrowly define the problem and thus the measurement required. Rather than being able to send

down all produced data, it is necessary to already know what many of the measurements will look like in order to be able to select the new ones that are required to address the specific scientific question. Here, the characterization of microbursts plays an essential role in being able to define the next requirements of the next set of observations in a manner that makes it feasible to obtain them.

The final focus question, “what is the global scale of microburst loss?” pulls together all the various components of the thesis. In many ways it serves to emphasize the thesis’ focus on process. Combining the different measurements with long-term averages provides an avenue for estimating the total loss due to microbursts. Owing to the various uncertainties involved, it is difficult to formulate a precise conclusion, but it is clear that there are times when microburst loss is a negligible factor. However, the techniques and assumptions made using single point data are easily transferrable to the multipoint domain, once the measurements are available.

This is not to say that there are not conclusions from the thesis. Rather it is to emphasize that analyzing the global picture is part of an iterative process. With each new set of observations the capability to tie together the disparate measurements into a cohesive tableau is refined. As the measurements increase, it is natural for the uncertainties to diminish until they reach an instructive point. Conclusions reached before that point help establish areas of further interest and provide instructive guideposts along the journey.

### **Van Allen Probes and BARREL**

There are a number of particular areas in which Van Allen Probes and BARREL will address microburst precipitation and the goals contained within this thesis. These areas are all defined by the fact that Van Allen Probes and BARREL provide measurements at different points as well as different measurement types. The basic requirement is that there needs to be an opportune moment of when two measurement platforms are in conjugate locations.

One of the key features of Van Allen Probes is the ability to calculate Phase Space Density (PSD) from the particle measurements. Calculating PSD requires measurements of pitch angle resolved particle measurements as well as accurate measurements of the local magnetic field (for the first adiabatic invariant) and a reasonable model of the magnetic field that the particle encounters on its bounce path (for the second adiabatic invariant) and its drift path (for the third adiabatic invariant). Measurements of the PSD during the course of a storm permit a search for local maxima (an indication of local acceleration) as well as other features (Reeves et al., 2013). By combining measurements of PSD with local measurements of wave activity as well as measurements of precipitating population from BARREL, it is possible to assess directly the impact of precipitation on the trapped population. The primary tool for this (and other studies) is conjunctions—times when both Van Allen Probes spacecraft (or one Van Allen Probes spacecraft and a BARREL balloon, for example) end up on the same magnetic field line or contour. Conjunctions

therefore permit attempts to separate and assess correlation and causation separately.

Another key question for the combined platforms is the longitudinal (MLT) spread of various phenomena. As shown in Chapter 2 with SAMPEX or Chapter 3 with Freja, maps of microburst precipitation from historical measurements covered a wide swath of local times. What is missing is assessing the instantaneous width of these features—do they occur at all local times simultaneously or do they start in one location and then move around the magnetosphere, perhaps following an electron drift orbit? When we talk about spatio-temporal ambiguity for microbursts we often think about the small scale structures; as a low-earth orbiting spacecraft flies through a feature at 7km/s we think about whether or not a wiggle in time is a wiggle in space, or a time-varying phenomena. However, the same is true on larger scales—not that of an individual event, but rather that of the region of microburst precipitation. This is an area where coordinated measurements from Van Allen Probes and BARREL can try to resolve what is a local versus what is a global phenomenon.

A final major area for Van Allen Probes is measuring accurate and precise values for the total number of electrons (at proscribed energy levels) in the radiation belts. This is a quantity, which is essential for comparative studies, yet as was mentioned in Chapter 5, at present long-term statistical averages must be substituted. Both the accuracy and the precision of this value are important, specifically as functions of geomagnetic activity (or other parameters). Van Allen Probes can do this by taking advantage of its orbit to sample most equatorial

pitch angles and thus estimate the distribution of particle fluxes. Since the underlying question is about understanding how sources and losses stack up, providing an accurate baseline for comparison is a necessary and important service.

### **Parting Words**

The overarching goal to which this thesis contributes is to understand radiation belt dynamics. As this is a very large and complex undertaking is beyond the bounds of this single thesis. Nevertheless, the operative objective is to reduce the problem into one that *can* be attacked. To understand radiation belt dynamics we can think in terms of sources and losses. Framing the problem in this manner (sources and losses) leads to the need to quantify the impact of the individual processes for comparison. The focus questions presented and addressed in the thesis are a way of breaking the problem down further into soluble elements. In turn they combine as puzzle pieces to be a single piece of the larger whole. Past observations, such as from SAMPEX and Freja, inform and direct the design and requirements of future missions, such as FIREBIRD. FIREBIRD itself does not work in a vacuum. Although its primary science goals are designed to be achieved by itself, the largest one (quantifying total loss) is intended to be accomplished in conjunction with other missions and falls under future work, with the goal of completing one single piece of the larger puzzle.

## WORKS CITED

Anderson, K.A., Chase, L.M., Hudson, H.S., Lampton, M., Milton, D.W. and Parks, G.K. (1966) 'Balloon and rocket observations of auroral-zone microburst', *J. Geophys. Res.*, vol. 71, no. 19, pp. 4589-4617.

Baker, D.N., Kanekal, S.G. and Blake, J.B. (2004) 'Characterizing the Earth's outer Van Allen zone using a radiation belt content index', *Space Weather*, vol. 2, no. S02003.

Baker, D.N., Kanekal, S.G., Hoxie, V.C., Henderson, M.G., Li, X., Spence, H.E., Elkington, S.R., Friedel, R.H.W., Goldstein, J., Hudson, M.K., Reeves, G.D., Thorne, R.M., Kletzing, C.A. and Claudepierre, S.G. (2013) 'A Long-Lived Relativistic Electron Storage Ring Embedded in Earth's Outer Van Allen Belt', *Science*, vol. 340, no. 6129, pp. 186-190.

Baker, D.N., Kanekal, S.G., Li, X., Monk, S.P., Goldstein, J. and Burch, J.L. (2004) 'An extreme distortion of the Van Allen Belt arising from the 'Hallowe'en' solar storm in 2003', *Nature*, vol. 432, pp. 878-881.

Blake, J.B., Kolasinski, W.A., Fillius, R.W. and Mullen, E.G. (1992) 'Injection of Electrons and Protons with Energies of Tens of MeV into  $L < 3$  on 24 March 1991', *Geophys. Res. Lett.*, vol. 19, no. 8, pp. 821-824.

Blake, J.B., Looper, M.D., Baker, D.N., Nakamura, R., Klecker, B. and Hovestadt, D. (1996) 'New High Temporal and Spatial Resolution Measurements by SAMPEX of the Precipitation of Relativistic Electrons', *Adv. Space Res.*, vol. 18, no. 8, pp. 171-186.

Boehm, M., Paschmann, G., Clemons, J., Hofner, H., Frenzel, R., Ertl, M., Haerendel, G., Hill, P., Lauche, H., Eliasson, L. and Lundin, R. (1994) 'The TESP Electron Spectrometer and Correlator (F7) on Freja', *Space Science Reviews*, vol. 10, pp. 509-540.

Bortnik, J. and Thorne, R.M. (2007) 'The dual role of ELF/VLF chorus waves in the acceleration and precipitation of radiation belt electrons', *Journal of Atmospheric and Solar-Terrestrial Physics*, vol. 69, pp. 378-386.

Breneman, A.W., Kletzing, C.A., Pickett, J., Chum, J. and Santolik, O. (2009) 'Statistics of multispacecraft observations of chorus dispersion and source location', *Journal of Geophysical Research*, vol. 114, no. A06202.

Clemmons, J.H., Boehm, M.H., Paschmann, G.E. and Haerendel, G. (1994) 'Signatures of energy-time dispersed electron fluxes measured by Freja', *Geophys. Res. Lett.*, vol. 21, no. 17, pp. 1899-1902.

Comess, M.D., Smith, D.M., Selesnick, R.S., Millan, R.M. and Sample, J.G. (2013) 'Duskside relativistic electron precipitation as measured by SAMPEX: A statistical survey', *Journal of Geophys. Res.*, vol. 118, pp. 5050-5058.

Cully, C.M., Bonnell, J.W. and Ergun, R.E. (2008) 'THEMIS observations of long-lived regions of large-amplitude whistler waves in the inner magnetosphere', *Geophys. Res. Lett.*, vol. 35, no. L17S16.

Datta, S., Skoug, R.M., McCarthy, M.P. and Parks, G.K. (1996) 'Analysis and modeling of microburst precipitation', *Geophys. Res. Lett.*, vol. 23, no. 14, pp. 1729-1732.

Datta, S., Skoug, R.M., McCarthy, M.P. and Parks, G.K. (1997) 'Modeling of microburst electron precipitation using pitch angle diffusion theory', *Journal of Geophysical Research*, vol. 102, no. A8, pp. 17325-17333.

Davis, T.N. and Sugiura, M. (1966) 'Auroral Electrojet Activity Index AE and Its Universal Time Variations', *J. Geophys. Res.*, vol. 71, no. 3, pp. 785-801.

Friedel, R.H.W., Reeves, G.D. and Obara, T. (2002) 'Relativistic electron dynamics in the inner magnetosphere--a review', *Journal of Atmospheric and Solar-Terrestrial Physics*, vol. 64, pp. 265-282.

Hikishima, M., Omura, Y. and Summers, D. (2010) 'Microburst precipitation of energetic electrons associated with chorus wave generation', *Geophys. Res. Lett.*, vol. 37, no. L07103.

Hikishima, M., Yagitani, S., Omura, Y. and Nagano, I. (2009) 'Coherent nonlinear scattering of energetic electrons in the process of whistler mode chorus generation', *Journal of Geophys. Res.*, vol. 114, p. A10205.

Horne, R.B., Glauert, S.A. and Thorne, R.M. (2003) 'Resonant diffusion of radiation belt electrons by whistler-mode chorus', *Geophysical Research Letters*, vol. 30, no. 9, p. 1493.

Huang, C.-L., Spence, H.E., Singer, H.J. and Tsyananako, N.A. (2008) 'A quantitative assessment of empirical magnetic field models at geosynchronous orbit during magnetic storms', *J. Geophys. Res.*, vol. 113, p. A04208.

Imhof, W.L., Reagan, J.B., Voss, H.D., Gaines, E.E., Datlowe, D.W. and Mobilia, J. (1983) 'The modulated precipitation of radiation belt electrons by controlled signals from VLF transmitters', *Geophys. Res. Lett.*, vol. 10, no. 8, pp. 615-618.

Imhof, W.L., Voss, H.D., Mobilia, J., Datlowe, D.W., Gaines, E.E., McGlennan, J.P. and Inan, U.S. (1992) 'Relativistic', *Electron Microbursts*, vol. 97, no. A9, pp. 13829-13837.

Imhof, W.L., Voss, H.D., Mobilia, J., Walt, M., Inan, U.S. and Carpenter, D.L. (1989) 'Characteristics of Short-Duration Electron Precipitation Bursts and Their Relationship With VLF Wave Activity', *Journal of Geophysical Research*, vol. 94, no. A8, pp. 10079-10093.

Klecker, B., Hovestadt, D., Scholer, M., Arbinger, H., Ertl, M., Kastle, H., Kunnen, E., Laeverenz, P., Seidenschwang, E., Blake, J.B., Katz, N. and Mabry, D. (1993) 'HILT: A Heavy Ion Large Area Proportional Counter Telescope for Solar and Anomalous Cosmic Rays', *IEEE Transactions on Geoscience and Remote Sensing*, vol. 31, no. 3, pp. 542-548.

Lanzerotti, L. (2001) 'Space weather effects on technologies', in Song, Singer and Siscoe (ed.) *Space Weather*, American Geophysical Union.

Li., X., Temerin, M., Baker, D.N. and Reeves, G.D. (2011) 'Behavior of MeV electrons at geosynchronous orbit during last two solar cycles', *J. Geophys. Res.*, vol. 116, p. A11207.

Li, W., Thorne, R.M., Angelopoulos, V., Bortnik, J., Cully, C.M., Ni, B., LeContel, O., Roux, A., Auster, U. and Magnes, W. (2009) 'Global distribution of whistler-mode chorus waves observed on the THEMIS spacecraft', *Geophys. Res. Lett.*, vol. 36, no. L09104.

Lorentzen, K.R., Blake, J.B., Inan, U.S. and Bortnik, J. (2001) 'Observations of relativistic electron microbursts in association with VLF chorus', *Journal of Geophysical Research*, vol. 106, no. A4, pp. 6017-6027.

Lorentzen, K.R., Looper, M.D. and Blake, J.B. (2001) 'Relativistic electron microbursts during the GEM storms', *Geophys. Res. Lett.*, vol. 28, no. 13, pp. 2573-2576.

Mauk, B.H., Fox, N.J., Kanekal, S.G., Kessel, R.L., Sibeck, D.G. and Ukhorskiy, A. (2012) 'Science Objectives and Rationale for the Radiation Belt Storm Probes Mission', *Space Science Reviews*.

McPherron, R.L. and Barfield, J.N. (1980) 'A seasonal change in the effect of field-aligned currents at synchronous orbit', *Journal of Geophysical Research*, vol. 85, pp. 6743-6746.

Meredith, N.P., Horne, R.B., Thorne, R.M. and Anderson, R.R. (2003) 'Favored regions for chorus-driven electron acceleration to relativistic energies in the Earth's outer radiation belt', *Geophys. Res. Lett.*, vol. 30, no. 16, p. 1871.

Millan, R.M. and Baker, D.N. (2012) 'Acceleration of Particles to High Energies in Earth's Radiation Belts', *Space Sci. Rev.*, vol. 173, pp. 103-131.

Millan, R.M., McCarthy, M.P., Sample, J.G., Smith, D.M., Thompson, L.D., McGaw, D.G., Woodger, L.A., Hewitt, J.G., Comess, M.D., Yando, K.B., Liang, A.X., Anderson, B.A., Knezeck, N.R., Rexroad, W.Z., Scheiman, J.M., Bowers, G.S., Halford, A.J., Collier, A.B., Cliverd, M.A., Lin, R.P. et al. (2013) 'The Balloon Array for RBSP Relativistic Electron Losses (BARREL)', *Space Science Reviews*.

Millan, R.M. and Thorne, R.M. (2007) 'Review of radiation belt relativistic electron loss', *Journal of Atmospheric and Solar-Terrestrial Physics*, vol. 69, no. 2007, pp. 362-377.

Nakamura, R., Baker, D.N., Blake, J.B., Kanekal, S., Klecker, B. and Hovestadt, D. (1995) 'Relativistic electron precipitation enhancements near the outer edge of the radiation belt', *Geophys. Res. Lett.*, vol. 22, no. 9, pp. 1129-1132.

Nakamura, R., Isowa, M., Kamide, Y., Baker, D.N., Blake, J.B. andLooper, M. (2000) 'SAMPEX observations of precipitation bursts in the outer radiation belt', *Journal of Geophysical Research*, vol. 105, no. A7, pp. 15875-15885.

Ni, B. and Summers, D. (2010) 'Resonance zones for electron interaction with plasma waves in the Earth's dipole magnetosphere. I. Evaluation for field-aligned chorus, hiss, and electromagnetic ion cyclotron waves', *Physics of Plasmas*, vol. 17, p. 042902.

O'Brien, T.P., Looper, M.D. and Blake, J.B. (2004) 'Quantification of relativistic electron microburst loss during the GEM storms', *Geophys. Res. Lett.*, vol. 31, no. L04802.

O'Brien, T.P., Lorentzen, K.R., Mann, I.R., Meredith, N.P., Blake, J.B., Fennell, J.F., Looper, M.D., Milling, D.K. and Anderson, R.R. (2003) 'Energization of relativistic electrons in the presence of ULF power and MeV microbursts: Evidence for dual ULF and VLF acceleration', *Journal of Geophysical Research*, vol. 108, no. A8, p. 1329.

Reeves, G.D., McAdams, K.L., Friedel, R.H.W. and O'Brien, T.P. (2003) 'Acceleration and Loss of relativistic electrons during geomagnetic storms', *Geophys. Res. Lett.*, vol. 30, p. 1529.

Reeves, G.D., Spence, H.E., Henderson, M.G., Morley, S.K., Friedel, R.H.W., Funsten, H.O., Baker, D.N., Kanekal, S.G., Blake, J.B., Fennell, J.F., Claudepierre, S.G., Thorne, R.M., Turner, D.L., Kletzing, C.A., Kurth, W.S., Larsen, B.A. and Niehof, J.T. (2013) 'Electron Acceleration in the Heart of the Van Allen Radiation Belts', *Science*, vol. 341, no. 6149, August, pp. 991-994.

Reinard, A.A., Skoug, R.M., Datta, S. and Parks, G.K. (1997) 'Energy spectral characteristics of auroral electron microburst precipitation', *Geophys. Res. Lett.*, vol. 24, no. 5, pp. 611-614.

Roederer, J.G. (1970) *Dynamics of Geomagnetically Trapped Radiation*, New York: Springer.

Rosenberg, T.J., Foster, J.C., Matthews, D.L., Sheldon, W.R. and Benbrook, J.R. (1977) 'Microburst Electron Precipitation at L ~4', *Journal of Geophysical Research*, vol. 82, no. 1, pp. 177-180.

Santolik, O., Gurnett, D.A. and Pickett, J.S. (2004) 'Multipoint investigation of the source region of storm-time chorus', *Annales Geophysicae*, vol. 22, pp. 2555-2563.

Santolik, O., Gurnett, D.A., Pickett, J.S., Parrot, M. and Cornilleau-Wehrlin, N. (2003) 'Spatio-temporal structure of storm-time chorus', *Journal of Geophysical Research*, vol. 108, no. A7, p. 1278.

Schultz, M. and Lanzerotti, L. (1974) *Particle Diffusion in the Radiation Belts*, New York: Springer-Verlag.

Selesnick, R.S. and Kanekal, S.G. (2009) 'Variability of the total radiation belt electron content', *J. Geophys. Res.*, vol. 114, p. A02203.

Skoug, R.M., Datta, S., McCarthy, M.P. and Parks, G.K. (1996) 'A cyclotron resonance model of VLF chorus emissions detected during electron microburst precipitation', *Journal of Geophysical Research*, vol. 101, no. A10, pp. 21481-21491.

Spence, H.E., Blake, J.B., Crew, A.B., Driscoll, S., Klumpar, D.M., Larsen, B.A., Legere, J., Longworth, S., Mosleh, E., O'Brien, T.P., Smith, S., Springer, L. and Widholm, M. (2012) 'Focusing on Size and Energy Dependence of Electron Microbursts From the Van Allen Radiation Belts', *Space Weather*, vol. 10, no. S1104.

Sugiura, M. (1964) 'Hourly values of equatorial Dst for IGY', *Annals of the International Geophysical Year*, vol. 35, pp. 945-948.

Summers, D., Ni, B. and Meredith, N.P. (2007) 'Timescales for radiation belt electron acceleration and loss due to resonant wave-particle interactions: 1. Theory', *J. Geophys. Res.*, vol. 112, p. A04206.

Thorne, R. (2010) 'Radiation Belt Dynamics: The importance of wave-particle interactions', *Geophys. Res. Lett.*, vol. 37, p. L22107.

Thorne, R.M., O'Brien, T.P., Shprits, Y.Y., Summers, D. and Horne, R.B. (2005) 'Timescale for MeV electron microburst loss during geomagnetic storms', *Journal of Geophysical Research*, vol. 110.

Tsurutani, B.T. and Smith, E.J. (1974) 'Postmidnight Chorus: A Substrom Phenomenon', *Journal of Geophysical Research*, vol. 79, no. 1, pp. 118-127.

Tsyganenko, N.A. (1989) 'A magnetospheric magnetic field model with a warped tail current sheet', *Planetary Space Sci.*, vol. 37, pp. 5-20.

Turner, D.L., Shprits, Y., Hartinger, M. and Angelopoulos, V. (2012) 'Explaining sudden losses of outer radiation belt electrons during geomagnetic storms', *Nature Physics*, vol. 8, no. 3.